



MINISTÉRIO DA CIÊNCIA, TECNOLOGIA, INOVAÇÕES E COMUNICAÇÕES  
**INSTITUTO NACIONAL DE PESQUISAS ESPACIAIS**

sid.inpe.br/mtc-m21b/2017/02.04.17.17-TDI

**AEROTHERMODYNAMICS ANALYSIS OF A  
REENTRY VEHICLE WITH SURFACE  
DISCONTINUITY - LIKE A GAP**

Luis Thiago Lucci Corrêa Paolicchi

Doctorate Thesis of the Graduate  
Course in Engineering and Space  
Technology, guided by Dr. Wilson  
Fernando Nogueira dos Santos,  
approved in February 02, 2017.

URL of the original document:

<<http://urlib.net/8JMKD3MGP3W34P/3NAKDRE>>

INPE  
São José dos Campos  
2017

**PUBLISHED BY:**

Instituto Nacional de Pesquisas Espaciais - INPE

Gabinete do Diretor (GB)

Serviço de Informação e Documentação (SID)

Caixa Postal 515 - CEP 12.245-970

São José dos Campos - SP - Brasil

Tel.:(012) 3208-6923/6921

Fax: (012) 3208-6919

E-mail: pubtc@inpe.br

**COMMISSION OF BOARD OF PUBLISHING AND PRESERVATION  
OF INPE INTELLECTUAL PRODUCTION (DE/DIR-544):****Chairperson:**

Maria do Carmo de Andrade Nono - Conselho de Pós-Graduação (CPG)

**Members:**

Dr. Plínio Carlos Alvalá - Centro de Ciência do Sistema Terrestre (CST)

Dr. André de Castro Milone - Coordenação de Ciências Espaciais e Atmosféricas (CEA)

Dra. Carina de Barros Melo - Coordenação de Laboratórios Associados (CTE)

Dr. Evandro Marconi Rocco - Coordenação de Engenharia e Tecnologia Espacial (ETE)

Dr. Hermann Johann Heinrich Kux - Coordenação de Observação da Terra (OBT)

Dr. Marley Cavalcante de Lima Moscati - Centro de Previsão de Tempo e Estudos Climáticos (CPT)

Silvia Castro Marcelino - Serviço de Informação e Documentação (SID) **DIGITAL**

**LIBRARY:**

Dr. Gerald Jean Francis Banon

Clayton Martins Pereira - Serviço de Informação e Documentação (SID)

**DOCUMENT REVIEW:**

Simone Angélica Del Duca Barbedo - Serviço de Informação e Documentação (SID)

Yolanda Ribeiro da Silva Souza - Serviço de Informação e Documentação (SID)

**ELECTRONIC EDITING:**

Marcelo de Castro Pazos - Serviço de Informação e Documentação (SID)

André Luis Dias Fernandes - Serviço de Informação e Documentação (SID)



MINISTÉRIO DA CIÊNCIA, TECNOLOGIA, INOVAÇÕES E COMUNICAÇÕES  
**INSTITUTO NACIONAL DE PESQUISAS ESPACIAIS**

sid.inpe.br/mtc-m21b/2017/02.04.17.17-TDI

**AEROTHERMODYNAMICS ANALYSIS OF A  
REENTRY VEHICLE WITH SURFACE  
DISCONTINUITY - LIKE A GAP**

Luis Thiago Lucci Corrêa Paolicchi

Doctorate Thesis of the Graduate  
Course in Engineering and Space  
Technology, guided by Dr. Wilson  
Fernando Nogueira dos Santos,  
approved in February 02, 2017.

URL of the original document:

<<http://urlib.net/8JMKD3MGP3W34P/3NAKDRE>>

INPE  
São José dos Campos  
2017

Cataloging in Publication Data

---

Paolicchi, Luis Thiago Lucci Corrêa.

P196a      Aerothermodynamics analysis of a reentry vehicle with surface discontinuity - Like a Gap / Luis Thiago Lucci Corrêa Paolicchi. – São José dos Campos : INPE, 2017.  
xx + 140 p. ; (sid.inpe.br/mtc-m21b/2017/02.04.17.17-TDI)

Thesis (Doctorate in Engineering and Space Technology) – Instituto Nacional de Pesquisas Espaciais, São José dos Campos, 2017.

Guiding : Dr. Wilson Fernando Nogueira dos Santos.

1. Direct simulation Monte carlo. 2. Hypersonic vehicle. 3. Gas dynamics. 4. Discontinuity on vehicle surface. 5. Reentry vehicle. I.Title.

CDU 629.7.015:519.87

---



Esta obra foi licenciada sob uma Licença [Creative Commons Atribuição-NãoComercial 3.0 Não Adaptada](https://creativecommons.org/licenses/by-nc/3.0/).

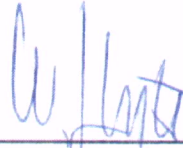
This work is licensed under a [Creative Commons Attribution-NonCommercial 3.0 Unported License](https://creativecommons.org/licenses/by-nc/3.0/).

Aluno (a): **Luis Thiago Luccl Corrêa Paolicchi**  
"AEROTHERMODYNAMICS ANALYSIS OF A REENTRY VEHICLE WITH SURFACE DISCONTINUITY-LIKE A GAP"

Aprovado (a) pela Banca Examinadora  
em cumprimento ao requisito exigido para  
obtenção do Título de **Doutor(a)** em

**Engenharia e Tecnologia**  
**Espaciais/Combustão e Propulsão**

Dr. Wilson Fernando Nogueira dos Santos



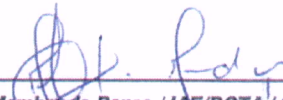
\_\_\_\_\_  
*Presidente / Orientador(a) / INPE / Cachoeira Paulista - SP*

Dr. Jeronimo dos Santos Travelho



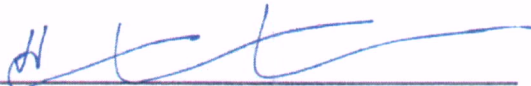
\_\_\_\_\_  
*Membro da Banca / INPE / São José dos Campos - SP*

Dr. Márcio Teixeira de Mendonça



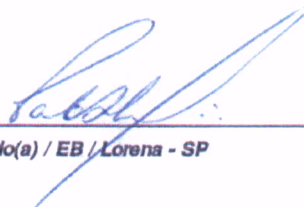
\_\_\_\_\_  
*Membro da Banca / IAE/DCTA / SJCampos - SP*

Dr. Helcio Francisco Villa Nova



\_\_\_\_\_  
*Convidado(a) / UNIFEI / Itajubá - MG*

Dr. Paulo Henrique Mineiro Leite



\_\_\_\_\_  
*Convidado(a) / EB / Lorena - SP*

*Este trabalho foi aprovado por:*

*maioria simples*

*unanimidade*

**São José dos Campos, 02 de Fevereiro de 2017**



## **ACKNOWLEDGEMENTS**

I would like to thank my family for believing that the pursuit of knowledge is eternal.

In addition, a thank you to CNPq, for financial support No. 557605 / 2010-5.



## ABSTRACT

A computational analysis has been performed in order to investigate the impact of the presence of gaps and variations on the vehicle nose radius in the flowfield structure, as well as on the aerodynamic properties of hypersonic vehicles in atmospheric reentry at different altitudes. The calculations were performed with a computational model that takes into account the effects of thermodynamic non-equilibrium. A detailed description of the impact on the flow structure - velocity, density, pressure and temperature - as well as on aerodynamic properties - number flux, heat transfer, pressure and skin friction - is presented for various sections of the vehicle due to variations in the gap ratio ( $L/H$ ) and nose ratio ( $R$ ), for altitudes ( $A$ ) of 100, 90 and 80 km. For the conditions investigated, the analyzes showed that the gap presence caused a small influence on the flowfield structure and that a single vortex inside the gap for all gap ratio ( $L/H$ ) investigated was formed, thus demonstrating that the flow topology inside the gap for transition flow regime differs from the flow topology present for the continuum flow regime. In addition, as the vehicle becomes more aerodynamic, i.e., with the decrease in vehicle nose radius ( $R$ ), disturbances in the flow structure around the vehicle are smaller and larger are the heat and pressure loads inside the gap.

Palavras-chave: Direct Simulation Monte Carlo. Hypersonic vehicle. Gas dynamics. Discontinuity on vehicle surface. Reentry vehicle.



# ANÁLISE AEROTERMODINÂMICA DE UM VEÍCULO NA REENTRADA COM DESCONTINUIDADES NA SUPERFÍCIE - DO TIPO FILETE.

## RESUMO

Uma análise computacional foi realizada com o objetivo de examinar o impacto da presença de filetes e da variação do raio de curvatura do bordo de ataque na estrutura do escoamento, bem como nas propriedades aerodinâmicas na superfície de veículos hipersônicos na reentrada atmosférica para diferentes altitudes. Os cálculos foram realizados com um modelo computacional que leva em conta os efeitos do não-equilíbrio termodinâmico. Uma descrição detalhada do impacto sobre a estrutura do escoamento - velocidade, massa específica, pressão e temperatura - bem como sobre as propriedades aerodinâmicas - fluxo molecular, transferência de calor, pressão e atrito - é apresentada para diversas seções do veículo devido às variações nas razões largura-profundidade ( $L/H$ ) do filete e razões do bordo de ataque ( $R$ ) para as altitudes ( $A$ ) de 100, 90 e 80 km. Para as condições investigadas, as análises mostraram que a presença do filete causou uma pequena influência na estrutura do escoamento e que um único vórtice no interior do filete para todas as razões de ( $L/H$ ) investigadas foi formado, demonstrando então que a topologia do escoamento no interior do filete para regime de transição difere da topologia do escoamento presente para o regime do contínuo. Além disso, a medida que o veículo se torna mais aerodinâmico, isto é, com a diminuição do raio de curvatura do bordo de ataque ( $R$ ), as perturbações na estrutura do escoamento ao redor do veículo são menores e maiores são as cargas de calor e pressão dentro do filete.

Palavras-chave: Simulação Direta de Monte Carlo. Veículo hipersônico. Cinética dos gases. Imperfeições na superfícies de veículos. Veículo na reentrada.



## LIST OF FIGURES

	<u>Page</u>
1.1 (a) SARA Sketch, (b) SARA Geometry . . . . .	2
1.2 Thermal Protection System of Space Shuttle. . . . .	3
1.3 (a) TPS on orbit fly, (b) TPS post fly . . . . .	4
1.4 Flow regimes as a function of the Knudsen number. . . . .	7
1.5 Drawing illustrating the flowfield structure inside a gap in the continuum flow regime. . . . .	10
2.1 Validity of the conventional mathematical models as function of local Knudsen number. Adapted from Bird (BIRD, 1986). . . . .	16
2.2 Flow Chart of DSMC method. . . . .	20
2.3 Phenomenological models timeline. Adapted from Bird (BIRD, 2013). . .	23
2.4 Binary collision in the centre of mass frame reference. Adapted from Bird (BIRD, 1994). . . . .	31
2.5 Drawing illustration of the Maxwell and CLL reflection model. Adapted from Leite (LEITE, 2009). . . . .	37
3.1 Drawing illustrating a (a) schematic view of the capsule, and (b) the important parameters. . . . .	40
3.2 Velocity-altitude map for the SARA capsule. . . . .	42
3.3 Drawing illustrating a schematic view of the computational domain. . . .	44
4.1 Drawing illustrating the flat-ended circular cylinder. . . . .	51
4.2 Computational domain for the flat-ended cylinder model. . . . .	53
4.3 Effect of variation in the cell size in the $\xi$ -direction coordinate on pressure (top), skin friction (middle) and heat transfer (bottom) coefficients. . . .	55
4.4 Effect of variation in the cell size in the $\eta$ -direction coordinate on pressure (top), skin friction (middle) and heat transfer (bottom) coefficients. . . .	56
4.5 Effect of variation in the number of molecules on pressure (top), skin friction (middle) and heat transfer (bottom) coefficients. . . . .	57
4.6 Drawing illustrating the standard grid. . . . .	58
4.7 Normal velocity profile along the stagnation line. . . . .	59
4.8 Density ratio profile along the stagnation line. . . . .	59
4.9 Dimensionless translational temperature ratio profile along the stagnation line. . . . .	60

4.10	Dimensionless rotational temperature ratio profile along the stagnation line. . . . .	60
5.1	Tangential velocity ratio ( $u/U_\infty$ ) for three sections $s/R$ along the capsule surface and altitudes of 100 and 80 <i>km</i> , parameterized by the gap $L/H$ ratio and nose radius $R$ . . . . .	64
5.2	Tangential velocity ratio ( $u/U_\infty$ ) for three vertical sections inside the gap for altitude of 100 <i>km</i> (left) and 80 <i>km</i> (right), nose radius $R$ , and gap $L/H$ of 1, 1/2 and 1/4. . . . .	66
5.3	Normal velocity ratio ( $v/U_\infty$ ) for three transversal sections inside the gap for altitude of 100 <i>km</i> (left) and 80 <i>km</i> (right), nose radius $R$ , and gap $L/H$ of 1, 1/2 and 1/4. . . . .	67
5.4	Streamlines traces inside the gap for altitude of 100 <i>km</i> (left) and 80 <i>km</i> (right), nose radius $R$ , and gap $L/H$ of 1, 1/2, and 1/4. . . . .	68
5.5	Streamlines traces inside the gap for altitude of 100 <i>km</i> (left) and 80 <i>km</i> (right), nose radius $R/2$ , and gap $L/H$ of 1, 1/2, and 1/4. . . . .	69
5.6	Streamlines traces inside the gap for altitude of 100 <i>km</i> (left) and 80 <i>km</i> (right), nose radius $R/4$ , and gap $L/H$ of 1, 1/2, and 1/4. . . . .	70
5.7	Density ratio ( $\rho/\rho_\infty$ ) for three sections $s/R$ along the capsule surface and altitudes of 100 and 80 <i>km</i> , parameterized by the gap $L/H$ ratio and nose radius $R$ . . . . .	73
5.8	Density ratio ( $\rho/\rho_\infty$ ) for three vertical sections inside the gap for altitude of 100 <i>km</i> (left) and 80 <i>km</i> (right), nose radius $R$ , and gap $L/H$ of 1, 1/2 and 1/4. . . . .	74
5.9	Contour maps for density ratio along with streamline traces inside the gap for altitudes of 100 <i>km</i> (left) and 80 <i>km</i> (right), nose radius $R$ , and gap $L/H$ of 1, 1/2, and 1/4. . . . .	75
5.10	Pressure ratio ( $p/p_\infty$ ) for three sections $s/R$ along the capsule surface and altitudes of 100 and 80 <i>km</i> , parameterized by the gap $L/H$ ratio and nose radius $R$ . . . . .	77
5.11	Pressure ratio ( $p/p_\infty$ ) for three vertical sections inside the gap for altitudes of 100 <i>km</i> (left) and 80 <i>km</i> (right), nose radius $R$ , and gap $L/H$ of 1, 1/2 and 1/4. . . . .	79
5.12	Contour maps for pressure ratio ( $p/p_\infty$ ) along with streamline traces inside the gap for altitude of 100 <i>km</i> (left) and 80 <i>km</i> (right), nose radius $R$ , and gap $L/H$ of 1, 1/2, and 1/4. . . . .	80
5.13	Temperature ratio ( $T/T_\infty$ ) for three sections $s/R$ along the capsule surface and altitudes of 100 and 80 <i>km</i> , parameterized by the gap $L/H$ ratio and nose radius $R$ . . . . .	83

5.14	Translational temperature ratio ( $T_T/T_\infty$ ) for three sections $s/R$ along the capsule surface and altitudes of 100 and 80 <i>km</i> , parameterized by the gap $L/H$ ratio and nose radius $R$ . . . . .	84
5.15	Temperature ratio ( $T/T_\infty$ ) for three sections $\xi_L$ inside the gap for altitude 100 km (left) and 80 km (right) for radius ratio $R = 1.00$ and gap ratio $G = 1.00$ . . . . .	86
5.16	Translational temperature ratio ( $T_T/T_\infty$ ) for three sections $\xi_L$ inside the gap for altitude of 100 km (left) and 80 km (right) for radius ratio $R = 1.00$ and gap ratio $G = 1.00$ . . . . .	87
5.17	Translational temperature ratio ( $T_T/T_\infty$ ) inside the gaps parameterized by the gap $L/H$ ratio of 1, 1/2 and 1/4 and altitude of 100 km (left) and 80 km (right). . . . .	88
5.18	Dimensionless number flux ( $N_f$ ) distribution along surfaces $S1$ and $S5$ as a function of the dimensionless arc length $s/R$ parameterized by the altitude, nose radius, and the gap $L/H$ ratio. . . . .	92
5.19	Dimensionless number flux ( $N_f$ ) along surface $S2$ as a function of the dimensionless height $\eta/H$ , parameterized by the altitude, nose radius and the gap $L/H$ ratio. . . . .	94
5.20	Dimensionless number flux ( $N_f$ ) along surface $S3$ as a function of the dimensionless length $\xi_L$ , parameterized by the altitude, nose radius and the gap $L/H$ ratio. . . . .	95
5.21	Dimensionless number flux ( $N_f$ ) along surface $S4$ as a function of the dimensionless height $\eta/H$ , parameterized by the altitude, nose radius and the gap $L/H$ ratio. . . . .	96
5.22	Heat transfer coefficient ( $C_h$ ) distribution along surfaces $S1$ and $S5$ as a function of the dimensionless arc length $s/R$ parameterized by the altitude, nose radius, and the gap $L/H$ ratio. . . . .	100
5.23	Heat transfer coefficient ( $C_h$ ) distribution along surface $S2$ as a function of the dimensionless height $\eta/H$ parameterized by the altitude, nose radius, and the gap $L/H$ ratio. . . . .	102
5.24	Heat transfer coefficient ( $C_h$ ) distribution along surface $S3$ as a function of the dimensionless length $\xi_L$ parameterized by the altitude, nose radius, and the gap $L/H$ ratio. . . . .	103
5.25	Heat transfer coefficient ( $C_h$ ) distribution along surface $S4$ as a function of the dimensionless height $\eta/H$ parameterized by the altitude, nose radius, and the gap $L/H$ ratio. . . . .	104

5.26	Pressure coefficient ( $C_p$ ) distribution along surfaces $S1$ and $S5$ as a function of the dimensionless arc length $s/R$ parameterized by the altitude, nose radius, and the gap $L/H$ ratio. . . . .	106
5.27	Pressure coefficient ( $C_p$ ) distribution along surface $S2$ as a function of the dimensionless height $\eta/H$ parameterized by the altitude, nose radius, and the gap $L/H$ ratio. . . . .	110
5.28	Pressure coefficient ( $C_p$ ) distribution along surface $S3$ as a function of the dimensionless length $\xi_L$ parameterized by the altitude, nose radius, and the gap $L/H$ ratio. . . . .	111
5.29	Pressure coefficient ( $C_p$ ) distribution along surface $S4$ as a function of the dimensionless height $\eta/H$ parameterized by the altitude, nose radius, and the gap $L/H$ ratio. . . . .	112
5.30	Skin friction coefficient ( $C_f$ ) distribution along surfaces $S1$ and $S5$ as a function of the dimensionless arc length $s/R$ parameterized by the altitude, nose radius, and the gap $L/H$ ratio. . . . .	114
5.31	Skin friction coefficient ( $C_f$ ) distribution along surface $S2$ as a function of the dimensionless height $\eta/H$ parameterized by the altitude, nose radius, and the gap $L/H$ ratio. . . . .	117
5.32	Skin friction coefficient ( $C_f$ ) distribution along surface $S3$ as a function of the dimensionless length $\xi_L$ parameterized by the altitude, nose radius, and the gap $L/H$ ratio. . . . .	118
5.33	Skin friction coefficient ( $C_f$ ) distribution along surface $S4$ as a function of the dimensionless height $\eta/H$ parameterized by the altitude, nose radius, and the gap $L/H$ ratio. . . . .	119
5.34	Comparison of wall pressure ratio ( $p_w/p_o$ ) distribution along the body surface in a (a) linear scale and in a (b) logarithm scale. . . . .	124

## LIST OF TABLES

	<u>Page</u>
3.1 Geometric cases investigated. . . . .	41
3.2 Freestream flow conditions for 100 km. . . . .	41
3.3 Freestream flow conditions for 90 km. . . . .	42
3.4 Freestream flow conditions for 80 km. . . . .	42
3.5 Characteristics of simulated air for DSMC calculations . . . . .	44
4.1 Freestream flow conditions. . . . .	51
4.2 Gas properties. . . . .	51
4.3 Number of cells in the ( $\xi$ -direction) and [ $\eta$ -direction] for the flat-ended cylinder model. . . . .	54
5.1 Total Drag Coefficient ( $C_d$ ) for all vehicles cases investigated. . . . .	121
5.2 Flow and geometric conditions for the spherically blunted cone models. .	122



# Nomenclature

$b$	Impact parameter
$C_f$	Skin friction coefficient, $\tau_w/(\frac{1}{2}\rho_\infty U_\infty^2)$
$C_h$	Heat transfer coefficient, $q_w/(\frac{1}{2}\rho_\infty U_\infty^3)$
$C_p$	Pressure coefficient, $(p_w - p_\infty)/(\frac{1}{2}\rho_\infty U_\infty^2)$
$\mathbf{c}$	Molecular velocity vector, $m/s$
$\mathbf{c}'$	Thermal molecular velocity, $m/s$
$d$	Molecular diameter, $m$
$D$	Diffusion coefficient, $m^2/s$
$e$	Specific molecular energy, $J/kg$
$E$	Molecular energy, $J$
$f$	Distribution function
$f_0$	Equilibrium distribution function
$F$	Force, $N$
$F_N$	Real molecules represented by a single DSMC particle
$H$	Gap depth, $m$
$k$	Boltzmann constant, $1.3806488 \times 10^{-23} \text{ Js}$
$Kn$	Knudsen number, $\lambda/L$
$L$	Characteristic, Gap length, $m$
$M$	Mach Number, $u/c$
$m$	Molecular mass, $kg$
$n$	Number density, $m^{-3}$
$N$	Number of particles
$N_f$	Dimensionless number flux
$p$	Pressure; Normal momentum flux, $N/m^2$
$P$	A probability
$Pr$	Prandtl number, $\mu c_p/K$
$q$	Net heat flux, $W/m^2$
$r$	Intermolecular separation, $m$
$R$	Ordinary gas constant, $J/Kmol$
$R_F$	Random number between 0 and 1
$Sc$	Schmidt number, $\mu/(\rho D_{11})$
$t$	Time, $s$
$T$	Temperature, $K$
$u$	Tangential velocity, $m/s$
$V$	Cell volume, $m^3$

$v$	Normal velocity, $m/s$
$Z$	Relaxation collision number

## Greek Symbols

$\alpha$	Accommodation coefficient
$\chi$	Deflection angle, degree
$\Delta$	Increment
$\epsilon$	Molecular energy
$\eta$	Power law
$\Gamma$	Mass flux; Gamma function
$\lambda$	Mean free path, $m$
$\mu$	Kinematic viscosity, $kg/m.s$
$\nu$	Collision frequency
$\omega$	Viscosity-temperature index; Angular velocity
$\phi$	Potential energy of interaction; Polar angle; Azimuth angle
$\Phi$	Perturbation term
$\Psi$	Azimuthal angle; Average of the degree of freedom
$\rho$	Gas density, $kg/m^3$
$\sigma$	Collision cross-section, $m$
$\sigma_u$	Viscosity cross-section
$\sigma_M$	Diffusion cross-section
$\sigma_T$	Total collision cross-section
$\tau$	Relaxation time, $s$ ; Tangential momentum
$\theta$	Angle; Elevation angle, degree
$\Theta$	Characteristic temperature, $K$
$\zeta$	Number of degrees of freedom

## Subscripts and superscripts

$i$	Refers to incident; internal
$o$	Refers to overall
$r$	Refers to rotational; reduced; relative; reattachment
$rf$	Refers to reflected
$ref$	Refers to reference values
$t$	Refers to translational
$v$	Refers to upstream

$v$	Refers to vibrational
$d$	Refers to dissociation; downstream
$w$	Refers to wall conditions
$\infty$	Refers to the freestream
$c$	Refers to cell; collision
$n$	Refers to normal
$m$	Refers to centre of mass
$n$	Refers to pairs
$x, y, z$	Refers to x-, y-, and z- cartesian axes
1, 2	Refers to species



# CONTENTS

	<u>Page</u>
<b>1 INTRODUCTION</b> . . . . .	<b>1</b>
1.1 Motivation . . . . .	1
1.2 Reentry Flow Regimes . . . . .	5
1.3 Previous Work . . . . .	7
1.4 Problem Definition and Scope of Current Work . . . . .	11
<b>2 COMPUTATIONAL METHOD</b> . . . . .	<b>15</b>
2.1 Methods for Modeling Transition Flows . . . . .	15
2.2 Direct Simulation Monte Carlo (DSMC) Method . . . . .	18
2.2.1 DSMC Methodology . . . . .	19
2.2.2 Molecular Models . . . . .	22
2.2.3 Collision Models . . . . .	25
2.2.4 Binary Elastic Collisions . . . . .	28
2.2.5 Internal Degrees-of-Freedom . . . . .	32
2.2.6 Translational-Rotational Energy Exchange . . . . .	33
2.2.7 Translational-Vibrational Energy Exchange . . . . .	34
2.2.8 Boundary Conditions . . . . .	35
<b>3 COMPUTATIONAL PROCEDURE</b> . . . . .	<b>39</b>
3.1 Geometry Definition . . . . .	39
3.2 Freestream Flow conditions . . . . .	41
3.3 Numerical Simulation Conditions . . . . .	43
<b>4 CODE VERIFICATION AND VALIDATION</b> . . . . .	<b>47</b>
4.1 Computational Requirements . . . . .	47
4.2 Computational Mesh Generation . . . . .	49
4.3 Computational Mesh Adaptation . . . . .	49
4.4 DSMC Test Case . . . . .	50
4.5 Effect of Mesh Resolution . . . . .	53
4.6 Effect of Number of Molecules Variations . . . . .	54
4.7 Numerical Comparisons . . . . .	58
<b>5 COMPUTATIONAL RESULTS AND DISCUSSION</b> . . . . .	<b>61</b>

5.1	Flowfield Properties . . . . .	61
5.1.1	Velocity Field . . . . .	61
5.1.2	Density Field . . . . .	71
5.1.3	Pressure Field . . . . .	76
5.1.4	Temperature Field . . . . .	81
5.2	Aerodynamic Surface Properties . . . . .	89
5.2.1	Number Flux . . . . .	89
5.2.2	Heat Transfer Coefficient . . . . .	97
5.2.3	Pressure Coefficient . . . . .	105
5.2.4	Skin Friction Coefficient . . . . .	113
5.2.5	Drag Coefficient . . . . .	120
5.2.6	Computational and Experimental Comparison . . . . .	122
<b>6</b>	<b>CONCLUSIONS . . . . .</b>	<b>125</b>
6.1	Concluding Remarks . . . . .	125
6.2	Future Work . . . . .	126
	REFERENCES . . . . .	<b>129</b>

# 1 INTRODUCTION

## 1.1 Motivation

The space activity has contributed over the years significantly to the development of modern nations. With respect to Brazil, space activities are developed based on National Program of Space Activities, PNAE (in portuguese, Programa Nacional de Atividades Espaciais) which aims at enabling the country develop and use space technologies in solving national problems and for the benefit of Brazilian society.

In order to overcome the technological challenges faced in implementing large projects, the PNAE has established itself through the practice of research and development activities, along with the academic sector, as a strong introducer of innovation. The priorities established by PNAE for the period from 2012 to 2021 include, among others, the development of probe rockets and launch vehicles, rockets launch center, completion of the multimission platform design, recoverable orbital platforms, and microgravity program.

To carry out scientific and technological experiments in microgravity, different means (CORRÊA JR.; MORAES JR., 1999) may be used in function of costs and time available for conducting the experiments. Among the alternatives (ACOSTA; MORAES JR., 1999), there are the recoverable orbital platforms (satellite), one of the items considered by the PNAE. It is an orbital system consisting of a platform in a capsule form, which after satellization, remains in orbit by the time needed to conduct the experiments, and then redirect to the Earth, where it is recovered on ground.

A platform of this type, called SARA (in portuguese, SATéelite Recuperável Atmosférico), Fig.1.1, is under development at IAE / DCTA, as one of the programs provided in the PNAE. It consists of a small satellite, operating in low Earth orbit (300 km), capable of carrying scientific or technological experiments of microgravity, small, with orbital permanence up to 10 days. Then, the satellite is brought back to Earth ground, recovered and reused afterwards.

It is usually accepted without questions that the main difficulties in the design of hypersonic vehicles are associated to the effects of high temperature gases which influence the forces present in the flow (pressure and skin friction), energy flux (convective heat and radiative ) and mass flow (ablation) acting on the vehicle. In order to support such loads, different material compositions are used in the manufacture of these vehicles, depending on their location and functionality. A result, discontinu-

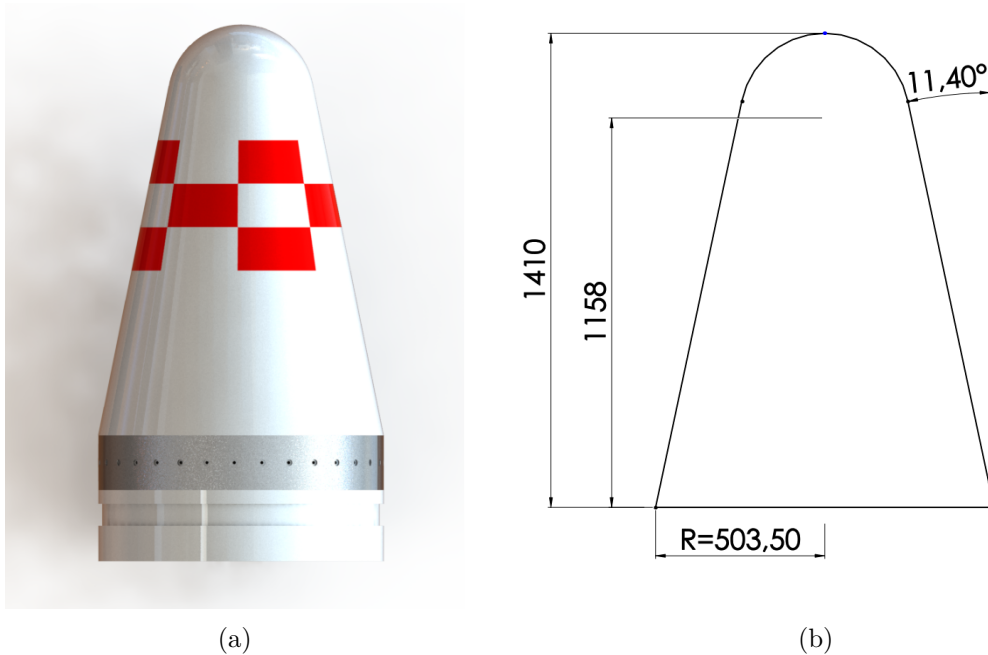


Figure 1.1 - (a) SARA Sketch, (b) SARA Geometry

ities in the surface of the vehicles are often present mainly because of the different expansion rates or ablation of these materials.

Such surface discontinuities are presented as protuberances, steps, cavities and gaps (BERTRAM; WIGGS, 1963; HAHN, 1969; NESTLER et al., 1969; NESTLER, 1982; MORGENSTERN JR.; CHOKANI, 1994) and are usually not considered in the calculations of thermal loads. However, some of them are present in Thermal Protection Systems (TPS) of hypersonic vehicles. Nevertheless, these discontinuities may constitute a potential source in increased heat flux to the surface or even in a premature transition from laminar to turbulent flow. An example of gaps in the TPS on the Space Shuttle Vehicle is illustrated in Fig. 1.2.

The determination of distribution of the thermal loads on the surface of the vehicles is part of the process to design the TPS (BERTIN; CUMMINGS, 2006). The majority of tiles in the TPS consists of high purity silica fibers foam with 6 x 6 inches square (JENKIS, 2007), with variable depth that depends on the tile location on the Orbiter. In principle, the flow is very complex in the gaps between tiles, since hot gases may flow into the gaps and cause an increase in the heating rate to the tile sidewall and the underlying aluminum structure (SCOTT; MARAIA, 1979).

Much has been learned from accidents with the Space Shuttle Orbiter in last decades



(a) Space Shuttle



(b) TPS



(c) Tiles

Figure 1.2 - Thermal Protection System of Space Shuttle.

about the importance of surface discontinuities. For instance, the Space Shuttle Orbiter Columbia, during its reentry on February 1, 2003. According to the final report of the Columbia Accident Investigation Board (CAIB), a piece of insulating foam produced a breach in the TPS of the leading edge of the left wing. It is believed that this small breach in the TPS provided a path for the hot gases, which reached the interior of the left wing during the severe aerothermodynamic environment in the reentry trajectory of the Columbia during its mission STS-107 (BERTIN; CUMMINGS, 2006).

Similar to the accident of the Space Shuttle Orbiter Columbia, a piece of foam in-

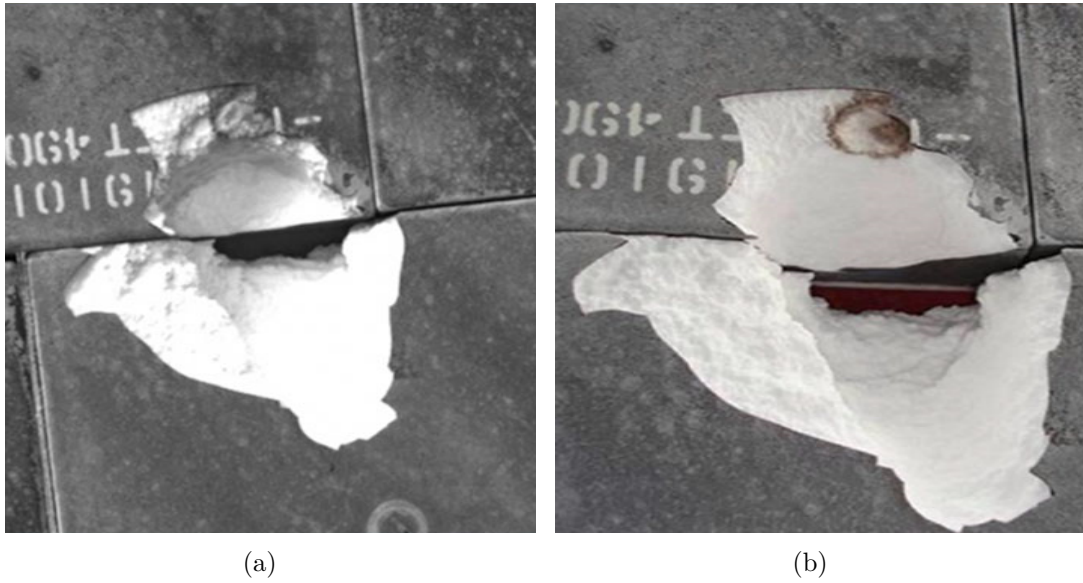


Figure 1.3 - (a) TPS on orbit fly, (b) TPS post fly

sulation was released from the external tank of the Space Shuttle Endeavour during the vehicle ascent in its mission STS-118 in August 2007 (PALMER et al., 2009). The impact of the foam in the TPS tile caused a defect like a cavity,  $0.076\text{ m}$  long by  $0.051\text{ m}$  wide, designated as damage site D-118, as illustrated in Fig.1.3 (a). The photograph shown in Fig.1.3 (a) was produced during the damage site inspection performed when the Orbiter Endeavour was docked to the International Space Station (ISS). A group of analysts, scientists from NASA Ames and NASA Langley Research Centers, known as the Damage Assessment Team (DAT), performed computational fluid dynamic (CFD) simulations in order to provide insight into the flow structures and flow physics in the interior of the cavity, during the STS-118 mission. Based on the detailed CFD solutions generated by the DAT, it was decided not to perform a spacewalk to repair the damage site but rather to fly Space Shuttle Endeavour back to Earth with the damage site. Fortunately, the Space Shuttle Endeavour successfully reentered the Earth's atmosphere and landed on August 21, 2007 and the final condition of the piece of insulation is shown in Fig.1.3 (b).

These examples emphasize the importance of the flow in gaps or cavities and indicate that a precise investigation in the aerothermodynamic loads is needed in the design of a reentry vehicle. In the development of a capsule, the modeling of the aerothermodynamics re-entry is one of the biggest challenges. The precise knowledge of the aerodynamics of the capsule along the trajectory on reentry allows a better understanding of the capsule performance, possibly resulting in increased payload as well

as a reduction in the thickness of the thermal protection system of the capsule.

In this context, a detailed study of the flow conditions and the thermal loads acting on SARA capsule become necessary, for certain altitudes in its path through the atmospheric reentry, and under certain characteristics, i.e., the presence of discontinuities like a gap on the surface.

## 1.2 Reentry Flow Regimes

Spacecraft re-entering the Earth's atmosphere go through different regimes of speed and flight conditions. The descent phase in which space vehicles enter the part of the upper atmosphere with a significant density is denoted by reentry. In this phase, space vehicles undergo not only different velocity regimes, hypersonic, supersonic and subsonic, but also different flow regimes, free molecular flow, transition and continuum. Therefore, the vehicle flight trajectories transverse a wide range of Mach, Reynolds and Knudsen numbers.

During the descent phase, important physical interactions arise between the vehicle and the environment around the space vehicle. At high altitudes, the interaction between the vehicle and the atmospheric air is characterized by the free molecular flow regime. In this regime, molecules collide with the surface of the vehicle, interact with the surface and then are reflected from the surface. However, collisions of reflected molecules with incoming molecules from the freestream are not frequently in this flow regime. As a result, they are ignored.

As the space vehicle enters a little deeper into the dense atmosphere, the mean free path between incoming atmosphere molecules decreases, and collisions between molecules reflected from the vehicle surface and the molecules incoming from the freestream can no longer be ignored. As a result, the flow in this condition defines the transition flow regime, i.e., transition between the collisionless flow regime and the continuum flow regime. In the transition flow regime, the contribution of aerodynamic forces and heat flux to the vehicle surface start increasing rapidly with decreasing altitude, causing large changes in the aerodynamic characteristic of the vehicle when compared with those observed in the free molecular flow. The flow-field in front of the vehicle is not in equilibrium, because interactions between gas particles with exchange of energy are rare and gas velocity is extraordinary high (SCHLINGLOFF, 2005).

As the space vehicle continues to enter into the atmosphere, it finally reaches the

continuum flow regime. In this regime, the flow around the space vehicle is treated by a macroscopic model that considers the air as a continuum, and the description of the flow is made in terms of spatial and temporal variations of the primary properties, such as velocity, pressure, density and temperature.

In order to quantify the relative importance of treating the fluid as a collection of particles vis-à-vis a continuum, a nondimensional parameter called Knudsen number is used and it is defined as Eq. (1.1):

$$Kn = \frac{\lambda}{L} \quad (1.1)$$

where  $\lambda$  is the mean free path and  $L$  is the characteristic length.

The mean free path  $\lambda$  is the distance traveled by molecules between collisions. For a gas in thermodynamic equilibrium, it depends on the number density of the gas,  $n$ , which varies with the altitude of the reentry vehicle, and with the diameter  $d$  of the gas molecule according to the following equation:

$$\lambda = \frac{1}{\sqrt{2}\sigma n} \quad (1.2)$$

where  $\sigma$  is the collision cross-section.

It is important to mention that the effective diameter of the gas particles,  $d$ , depends on temperature, however, the variation of  $d$  is not as significant a factor as the density (REGAN; ANANDAKRISHNAN, 1992).

A flow is defined in the continuum regime when the Knudsen number tends to zero. In this situation, molecules are considered to be so densely packed that the mean free path is insignificant compared with the flow dimensions. On the other hand, a flow is defined in the free molecular flow as the Knudsen number goes to infinity. Figure.1.4 presents the classification of flow regimes as a function of the overall Knudsen number.

Techniques used to analyze the flowfield structure of a hypersonic flow around reentry vehicles depend to a considerable degree on the shape of the vehicle and on a predicted atmospheric trajectory. Therefore, some regimes may be required to define the flowfield structure for a given flight conditions. For flows around reentry space vehicles in the range from 120 to 60 *km* of altitude, the molecular mean free path  $\lambda$

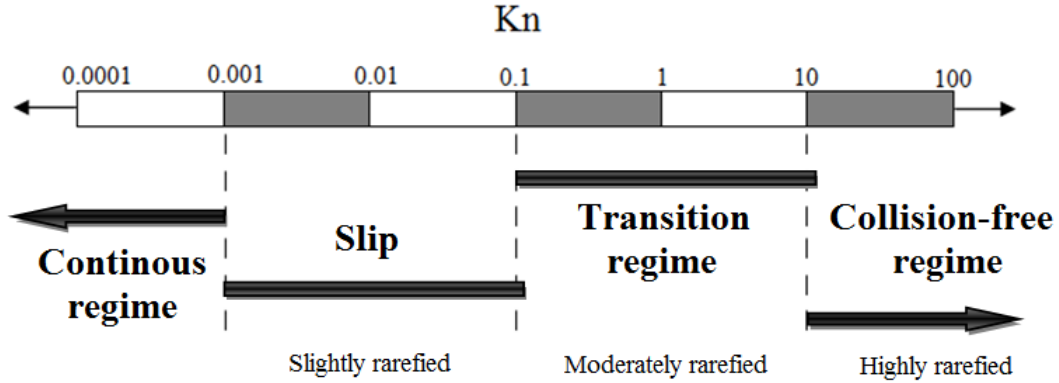


Figure 1.4 - Flow regimes as a function of the Knudsen number.

may be of the order of the dimensions of gaps or cavities related to a discontinuity on the vehicle surfaces. As a result, the Knudsen number, which indicates the degree of flow rarefaction, may be in the range of the transition flow regime, i.e., between the continuum regime and the molecular flow regime.

As a base of comparison, the depth  $H$  or length  $L$  for gaps or cavities, which represent a discontinuity on the vehicle surface, are usually on the order of 3 to 6  $mm$  (WEINSTEIN et al., 1975; GAI; MILTHORPE, 1995; EVERHART et al., 2006). In addition, for 90, 80, 70, and 60  $km$  of altitude, the molecular mean free path is 26.03, 4.11, 0.929, and 0.265  $mm$ , respectively. As a result, for  $H$  (or  $L$ ) of 3  $mm$ , the overall Knudsen number is the order of 8.67, 1.37, 0.31, and 0.088, for altitudes of 90, 80, 70 and 60  $km$ , respectively. By considering  $H$  (or  $L$ ) of 6  $mm$ , the overall Knudsen number is reduced by half. In this manner, the overall Knudsen number is in the transition flow regime, usually defined by the range  $0.1 < Kn < 10$ , as shown in Figure .1.4. Under the aforementioned assumptions, in the transition flow regime, the concepts of the continuum hypothesis can not be applied, and the molecular structure of the gas must be considered.

### 1.3 Previous Work

Because of the amount and quality of the data available for surface discontinuities, a survey of relevant references was carried out to establish trends of the flowfield that could be generalized and applied to only cavities and gaps. Without neglecting the contribution of many other research studies, a great deal of effort has been proceed on cavities and gaps (BREWER et al., 1973; DUNAVANT; THROCKMORTON, 1974; WEINSTEIN et al., 1975; BOHON et al., 1975; THROCKMORTON, 1976; BERTIN; KEISNER, 19778; SCOTT; MARAIA, 1979; BERTIN; GOODRICH, 1980; PITTS; MURBACH, 1982;

AVERY et al., 1983; SMITH et al., 1983; PETLEY et al., 1984; AVERY, 1985; HIGDON, 1985; CHARBONNIER; BOERRIGTER, 1993; HINDERKS et al., 2004; TRAINEAU et al., 1983; HINDERKS; RADESPIEL, 2006; PATIL et al., 2006; XU et al., 2015). In general, these research studies have been conducted in order to understand the physical aspects of a subsonic, supersonic or hypersonic flow past to these types of surface discontinuities. Therefore, it is proper at this time to digress a moment and to comment on some of these research studies.

Wieting (WIETING, 1970) performed an experimental investigation of heat-transfer distribution in rectangular cavities with width-to-depth ratios varying from 0.063 to 0.524 *in* hypersonic separated flow. Results indicate that the local convective heat flux to the cavity increases as the cavity width is increased, and it is maximum at the top of the rear surface, decreasing monotonically along the wetted perimeter of the cavity where it is less than 10 percent of the corresponding flat-plate heat flux on the bottom surface.

Dunavant and Throckmorton (DUNAVANT; THROCKMORTON, 1974) conducted an experimental investigation of the heat transfer to RSI tile surfaces with gap intersections. They found on the tile surface heating rates as high as 75% above the reference, undisturbed value were measured. Also, no appreciable increase in heating was shown where the boundary-layer bridges the gap and reattaches at the forward lip of the tile. The average heating rate to the surface was 24% greater than that to the same area on the undisturbed plate. Moreover, as expected, surface mismatch caused the worst heating condition with heating rates as high as three times the undisturbed value measured on the 0.1-in. protruding tile.

Bohon *et al.* (BOHON et al., 1975) exposed RSI panels in wind tunnel. The panel was subjected to a total of 23 thermal cycles to 1200 *K* surface temperature with 12 wind tunnel exposures. Top surface was at uniform temperature of 1200 *K*, however, gap temperatures in some cases exceeded 1400 *K*. Furthermore, pressure gradients induced transverse flow in gaps that significantly increased gap heating and stacked tile orientation is susceptible to flow in gaps causing increased sidewall heating, which could impose a tile thickness penalty. Also, the local impingement heating rates as much as three times the flat plate value. Staggered tile orientations were subjected to local impingement heating rates as much as three times the flat plate value.

Weinstein and Avery (WEINSTEIN et al., 1975) performed an aerodynamic heating to the gaps and surfaces of RSI in turbulent flow at Mach 6.6. Results indicated that

the maximum heating rate to an in-line tile arrangement occurred at the largest gap width and was 1.8 times the local-flat plate value. The maximum heating for this tile arrangement consistently occurred on the top of the tile just behind the leading-edge radius. The heating along the center line for this arrangement was only mildly affected by variations in both gap width and boundary-layer displacement thickness. The maximum heating rate to a staggered tile arrangement was approximately 2.9 times the local flat plate value.

Hinderks *et al.* (HINDERKS *et al.*, 2004) have investigated the gap flow structure. They showed that a complex flow within the gap exist, consisting of a vortex superposed by an axial flow. The analysis showed that the heat flux transferred to the structure depends on the thermal state of the structure. Also, effects due to changes in the gap geometry caused by deformations in the gap structure demonstrated that deformations should be considered in the design analysis.

Traineau *et al.* (TRAINEAU *et al.*, 1983) presented new recommendations on the gap heating prediction methodology based in experimental and simulations investigations. It was verified that heating in the transverse gap and the tee-gap regions was found different and depending on the nature of the flow i.e. laminar vs. turbulent for Mach numbers between 3.2 and 6.5. Also, they found that an increase in the angle of attack from 10 to 15 degrees for the same case studied, generated a 48% increase in pressure at the surface and 22% increase in heat transfer. They also showed that increasing the depth and length of the gaps caused a significant increase in temperature.

Everhart *et al.* (EVERHART *et al.*, 2006) investigated experimentally the effect of a pressure gradient on the local heating disturbance of rectangular cavities in a hypersonic flow conditions using a Mach 10 tunnel. This experimental study showed that, for open cavities, pressure gradient has a minimal effect on the average floor augmentation. Conversely, for closed cavities, pressure gradient increased the average heating by a factor of 50% above the zero gradient conditions, which was approximately 0.3. An assessment of the maximum increasing on the end wall revealed no apparent effect for the short or open cavity. However the analysis was inconclusive for the long or closed cavity.

According to Everhart *et al.* (EVERHART *et al.*, 2006), based on studies available in the current literature, the flow topology over cavities in the continuum flow regime may be generally identified by the length-to-depth ( $L/H$ ) ratio. In this framework, for the range  $L/H > 14$ , the cavity is known as closed cavity; the mainstream flow is

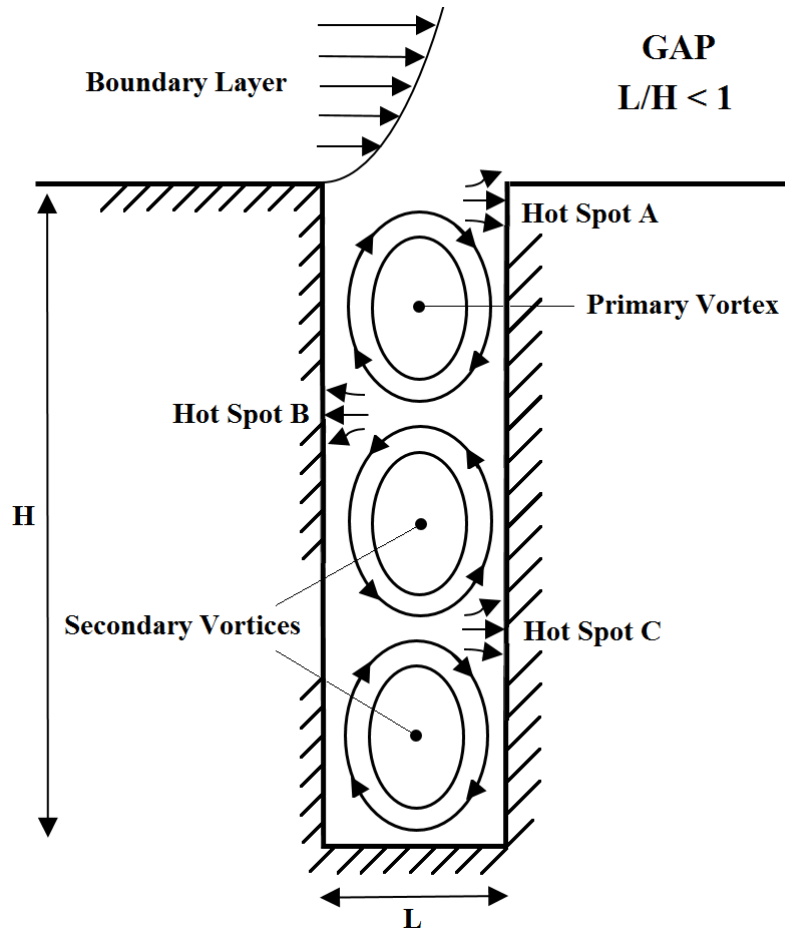


Figure 1.5 - Drawing illustrating the flowfield structure inside a gap in the continuum flow regime.

able to enter into the cavity and to impinge on the floor, and the flow is also stable. For the range  $10 < L/H < 14$ , the cavity is known as transitional cavity, since the flow is unsteady and alternates between the two stable bounding conditions. For the range  $1 < L/H < 10$ , the cavity is defined by open cavity; the mainstream flow does not enter the cavity directly, and the flow is stable. Finally, very short or deep cavity with  $L/H < 1$  is known as gap. For this particular  $L/H$  range, the gap flow topology is usually defined by the development of a column of counter-rotating vortices within the gap caused by the main stream flow, where the number of vortices is approximately given by  $H/L$ . In addition, alternating hot spots are developed in the gap when the vortices directionally align and impinge on the gap sidewall. For completeness, Figure.1.5 illustrates the flow topology in a gap.

Patil *et al.* (PATIL *et al.*, 2006) simulated a lid-driven flow in rectangular deep cavities for several Reynolds number. They concluded that as the Reynolds number increases,

the center of the primary vortex begins to move downwards at first, with respect to the top lid. However, as the Reynolds number increases beyond a value of 1000, the center of the primary vortex remains at almost a constant depth for both cases of rectangular cavity ratio ( $K=H/L$ ) investigated,  $H$  being the cavity-depth and  $L$  the cavity width. For the second primary vortex, when Reynolds number is low, it is located at the mid-plane i.e.,  $X_C = L/2$  but at higher Reynolds number it drifts towards the left walls i.e.,  $X_C < L/2$ . Another observation was that increasing the depth of the cavity does not affect the structure of the primary vortex nearest to the lid. Finally, they proposed that the center of two successive primary eddies are spaced at a vertical distance of  $\sim 1.355L$ .

Xu *et al.* (XU *et al.*, 2015) simulated two dimensional flow around a gap using finite volume method. It was observed that the heating ratio presents basically *U-shaped* distribution along the surface of the gap. The peak value appears at the corner of the windward surface of gaps because of the subsequent shock wave, and the gap effect depends not only on the angle of attack, but also on the Mach number. Also, it was confirmed that chamfer in the windward corner can effectively reduce gap effect coefficient, whereas the convex angle would increase gap effect coefficient.

#### 1.4 Problem Definition and Scope of Current Work

The majority of the available research studies on surface discontinuities pointed out in the previous subsection has gone into considering laminar or turbulent flow in the continuum flow regime. Nevertheless, there is little understanding of the physical aspects of a rarefied hypersonic flow past to these surface discontinuities related to the severe aerothermodynamic environment associated to a reentry space vehicle. In this fashion, the purpose of this dissertation is to investigate the impact of surface discontinuities on the flowfield structure and on the aerodynamic surface quantities of a reentry vehicle in a hypersonic flow in the transition flow regime. In this work, the flowfield structure is defined by the distribution of the primary properties, such as velocity, density, pressure, and the kinetic temperature, adjacent to the vehicle surfaces. Aerodynamic surface quantities are identified by the heat flux, and the normal and tangential forces acting on the vehicle surface.

In the present account, surface discontinuities are modeled by gaps situated on a surface of a reentry vehicle at hypersonic flow in a sufficiently high altitude where the appropriate mean free path becomes large, as compared to the gap dimensions, for the use of continuum hypothesis but not large enough for applying free molecular concept. At high altitudes, and therefore, low density, the molecular collision rate

is low and the energy exchange occurs under non-equilibrium conditions. In such a circumstance, the conventional continuum gas dynamics that are based on the concept of local equilibrium is inappropriate, and an approach based on molecular gas dynamics is required.

In order to assess the overall performance of these gaps, a parametric study related to the effects of the length-to-depth ( $L/H$ ) ratio for three different nose radius will be explored. In an attempt to assess such effects, an axi-symmetric blunt body with a gap in hypersonic flow will be investigated by employing the Direct Simulation Monte Carlo (DSMC) method.

The research behind the contributions of this work is described in detail in the remainder of this dissertation. In order to guide the reader, a breakdown of the purpose and contents of the following chapters is provided below.

Chapter 2: In this chapter, a description of the appropriate computational method is presented. Particular emphasis is placed on the DSMC methodology, molecular model, collision model, internal degrees of freedom and boundary conditions.

Chapter 3: The computational procedure is explored in this chapter. It includes the simulation conditions, the definition of the geometry analyzed in this research as well as the important geometric parameters.

Chapter 4: This chapter outlines the procedure for the verification and validation process of the DSMC code employed in the simulations. These procedures are applied in a test case defined by an axi-symmetric cone. The DSMC code is validated with simulation of a hypersonic flow over a an axi-symmetric blunt geometry and comparisons with previous experimental and numerical results.

Chapter 5: The purpose of this chapter is to present the computational results and discussion. In this chapter, the major features of the primary properties, velocity, density, pressure and kinetic temperatures, are discussed in details. Moreover, the aerodynamic surface quantities, number flux to the surface, heat transfer, pressure, shear stress, and total drag expressed in a coefficient form, are carefully examined. In addition, a special subsection is devoted to a comparison of simulation data to experimental data available in the literature.

Chapter 6: The final chapter of this dissertation contains a summary of the results obtained throughout the course of this work, and the conclusions that were drawn from them. Recommendations are made regarding further computational work that

should be undertaken on the topic of this dissertation.



## 2 COMPUTATIONAL METHOD

### 2.1 Methods for Modeling Transition Flows

Reentry vehicles, such as the SARA, experience different flow regimes during the course of their flight trajectories, because the Earth's atmosphere varies in density as a function of altitude. As the vehicle moves from one flow regime to another, it is observed that flow characteristics change continuously, and thereby, there are no discrete Knudsen numbers demarcating the various flow regimes. Generally, experiences and rules of thumb have been used as a guide, defining the regimes. It is common accepted that for  $M/Re > 3$  the flow is in free molecular regime and for  $M/\sqrt{Re} < 0.01$  the flow is in continuum regime (REGAN; ANANDAKRISHNAN, 1992). However, the density and hence the mean free path in the flowfield around the vehicle vary quite widely, making the freestream Knudsen number, based on the freestream mean free path  $\lambda_\infty$ , not be the most judicious choice for determining the flow regime.

It is important to recall that the mean free path  $\lambda$ , the speed of sound  $a$ , and the kinematic viscosity  $\mu$  are related by  $\mu \sim \lambda a$ . Hence, the Knudsen number may be expressible in terms the Mach number  $M (= V/a)$  and Reynolds number  $Re (= VL/\mu)$  by the relation  $Kn \sim M/Re$ , where  $V$  is the reference gas velocity and  $L$  a characteristic length.

Probstein (PROBSTEIN, 1961) followed by Cox and Crabtree (COX; CRABTREE, 1965) proposed a more appropriate Knudsen number based on mean free path that takes into account the state of particles emitted from the vehicle surface, i.e.,

$$\lambda_w = \frac{4}{\sqrt{\pi\gamma}} \sqrt{\frac{T_w}{T_\infty}} \frac{\lambda_\infty}{M_\infty} \quad (2.1)$$

where  $\gamma$  is the specific heat ratio,  $T_w$  is the wall temperature,  $T_\infty$  is the free stream temperature, and  $M_\infty$  is the freestream Mach number.

Bird (BIRD, 1986) proposed a broad rule of thumb for determining the flow regime based on the local Knudsen Number. Based in Eq. (1.1), the local Knudsen number is the ratio of the local mean free path to the scale length of any macroscopic gradient. This macroscopic gradient is defined by the following expression,

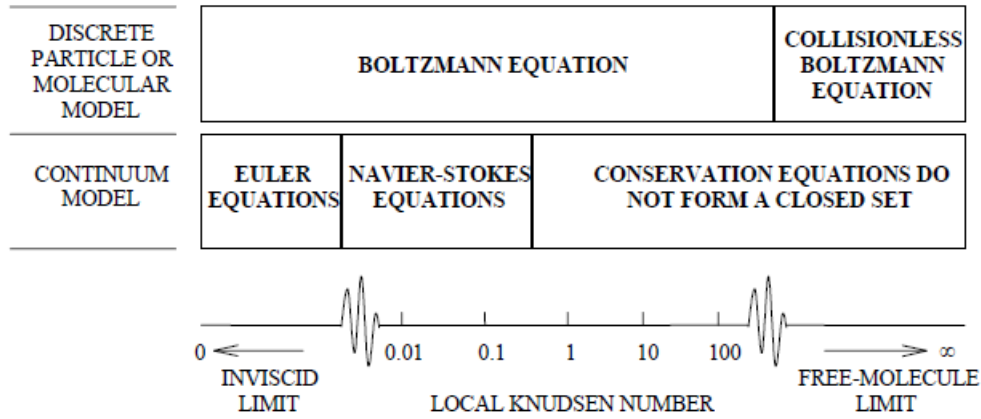


Figure 2.1 - Validity of the conventional mathematical models as function of local Knudsen number.

Adapted from Bird (BIRD, 1986).

$$l = \frac{\varphi}{\left| \frac{\partial \varphi}{\partial x} \right|} \quad (2.2)$$

where  $\varphi$  may be the density, velocity, pressure or temperature.

As a base of comparison, Fig. 2.1 illustrates the range of validity of the conventional mathematical formulations as a function of the local Knudsen number.

In the macroscopic model or continuum flow model, the general expressions of the fundamental conservation principles that govern the motion of gases are valid for all flow regimes. The Navier-Stokes equations may be assumed to be valid when the Knudsen number is very small in comparison with unity. In this case, the velocity distribution function departs from the Maxwellian distribution. However, the departure is still sufficiently small for the Chapman-Enskog theory (CHAPMAN; COWLING, 1970) for the transport coefficients to be valid.

When the transition flow regime is entered from the continuum flow regime, the first failure of the continuum theory occurs at the fluid-surface interface. As a result, the boundary condition of the continuity of the tangential velocity and temperature at the surface break down, leading to slip and temperature jump boundary conditions. This region is called the slip flow region given when  $0.1 > M/\sqrt{Re} > 0.01$ .

Extensive studies done by Boyd *et al.* (BOYD *et al.*, 1995) have pointed out that

the departure from the Maxwellian distribution becomes important when the local Knudsen number is  $Kn > 0.05$ , indicating that both the Chapman-Enskog theory and the Navier-Stokes equations cease to be valid. One alternative approach to this problem of the failure of the Navier-Stokes equations is to perform the Chapman-Enskog expansion to higher order to obtain the Burnett equations (BURNETT, 1936). Each level of approximation implies a different distribution function that deviates from the Maxwellian distribution.

Interest in the use of Burnett equations, based on the second order of the Chapman-Enskog expansion for calculating rarefied hypersonic flows, increased in the last decades (TANNEHILL; EISLER, 1976; FISCKO; CHAPMAN, 1988; FISCKO; CHAPMAN, 1989; LUMPKIN III; CHAPMAN, 1992; ZHONG et al., 1993; LEE, 1994; COMEAUX et al., 1995; KEON-YOUNG et al., 2001). However, their applications face additional difficulties related to the correct formulation of the boundary conditions and linear instability of these equations to short-wave disturbances. Furthermore, the Burnett equations increase the order of the differential equations that govern momentum and heat transport in the gas. These equations are more difficult to be solved numerically, and fail when the degree of rarefaction is sufficiently high. Finally, the Burnett equations can also lead to second-law impossibilities in certain situations, such as a negative dissipation function or a heat flux in an isothermal gas (COMEAUX et al., 1995). Cheng and Emanuel (CHENG; EMMANUEL, 1995) present a more detailed description of the use of Burnett equations for rarefied hypersonic flows.

In the microscopic model or molecular flow model, the gas is treated as a collection of molecules whose positions and velocities are individually tracked. Such a system requires solution of the Boltzmann equation (CERCIGNANI, 1988). Solutions of the Boltzmann equation are readily obtained in the free molecular limit as the Knudsen number tends to infinity. However, analytical difficulties are faced at finite Knudsen numbers. The Boltzmann equation is an integro-differential equation with the velocity distribution function as the only dependent variable. In contrast, the Navier-Stokes equations have the flow velocity and macroscopic thermodynamic properties as dependent variables. The reduction in the number of dependent variables is made at the expense of increasing the number of independent variables from those of physical space to those of phase space. In this way, an one-dimensional steady flow of a monatomic gas has an axially symmetric velocity distribution function so that the problem is three-dimensional in phase space.

Analytical solutions are generally limited to flows involving a simple molecular

model, one independent macroscopic variable and small disturbances. In addition, rarefied hypersonic flow problems often involve physical effects, such as chemical reactions and thermal radiation, which have not yet been incorporated into the Boltzmann formulation. Consequently, the mathematical difficulties associated with the direct solution of the Boltzmann equation have stimulated the development of physically-based numerical methods. The Boltzmann equation may be solved numerically by the following approaches: molecular dynamics method (ALDER; WAINWRIGHT, 1957; ALDER; WAINWRIGHT, 1958; DOMINIK; JÜRIG, 2009; AKIRA, 2011), test-particle method (HAVILAND; LAVIN, 1962; HAVILAND, 1965; FRENKEL; SMIT, 2009), direct numerical integration method (YEN, 1971; YEN, 1984) and the Direct Simulation Monte Carlo method (BIRD, 1976; BIRD, 1994; BIRD, 2013). For the purpose of this dissertation, only the Direct Simulation Monte Carlo method will be discussed.

## 2.2 Direct Simulation Monte Carlo (DSMC) Method

The Direct Simulation Monte Carlo method, or DSMC, introduced by Bird (BIRD, 1994), is a numerical method for the solution of the Boltzmann equation, quite different from the finite-difference method (YOSHIO, 2007). It is based on the physical concepts of rarefied gases and on the physical assumptions that form the basis for the phenomenological derivation of the Boltzmann equation. However, it is not derived from the Boltzmann equation itself. As well as the Boltzmann equation, the DSMC method was derived from the classical kinetic theory, and for this reason, both are subjected to the same restrictions. One of these restrictions is related to the gas be dilute, i.e., the average molecular diameter is much smaller than the average spacing between molecules in the gas. It allows the molecular motion to be decoupled from the molecular collisions over discrete time step intervals, which are small in comparison to the local mean collision time (BIRD, 1994; BIRD, 2013). However, studies of Alexander, Garcia and Alder (ALEXANDER *et al.*, 1995) demonstrated that the DSMC is also a potential method for investigating dense gases. The other restriction is the molecular chaos, in which the velocities of colliding particles are uncorrelated, and independent of position.

DSMC models the flow as being a collection of discrete molecules, each one with a position, velocity and internal energy. The state of the molecules is stored and modified with time as the molecules move, collide and undergo boundary interactions in simulated physical space. Particle motions are modeled deterministically, while the collisions are treated statistically. The simulated molecules represent a large

number of real molecules, since the computational cost would make it impossible to get the solution of the problem investigated using the actual number of molecules (ALEXANDER et al., 1995; SHU et al., 2005). DSMC simulations can vary in size from tens of thousands or millions of simulated molecules for very rarefied two-dimensional problems.

According to Bird (BIRD, 1978), the major advantage of the method is its relative ease of application in terms of both programming effort and computation time, but its procedures are such that the computation time is directly proportional to the number of simulated molecules. It has become a very popular methodology for the simulation of fluids, where molecular effects are important (PRASANTH; KAKKASSERY, 2006).

The method has been extensively tested in high Knudsen number flows over the past 50 years, and found to be in excellent agreement with experimental data (MOSS; SCOTT, 1986; MOSS et al., 1995; HARVEY; GALLIS, 2000). Comparisons with experimental data have given credibility, besides being of paramount importance to the conquest and widespread acceptance of the method. Although DSMC is richer in physical content and more capable of delivering higher-fidelity simulations than its continuum counterparts, its molecular nature makes DSMC computationally demanding. Even today, more than 50 years since the introduction of DSMC, the quest for speed is the main concern of DSMC researchers because speed appears to limit the range of applicability as well as the level of sophistication of molecular procedures (GALLIS et al., 2014).

### 2.2.1 DSMC Methodology

The core of the DSMC algorithm consists of four primary processes: (1) move the molecules, (2) index the molecules, (3) simulate collisions, and (4) sample the molecular properties. For convenience, the main phases of the DSMC algorithm is illustrated in Fig. 2.2.

A computational domain, which represents the physical space to be investigated, is initialized with uniform equilibrium gas conditions that agree with freestream conditions. This computational domain is divided into a set of cells where molecules are inserted with a velocity that was assumed to be a linear combination of the thermal velocity and the freestream velocity. Boundary conditions corresponding to the desired flow are imposed at time zero and should be such that a steady flow is established at a sufficient large time. In addition, the desired steady result a time

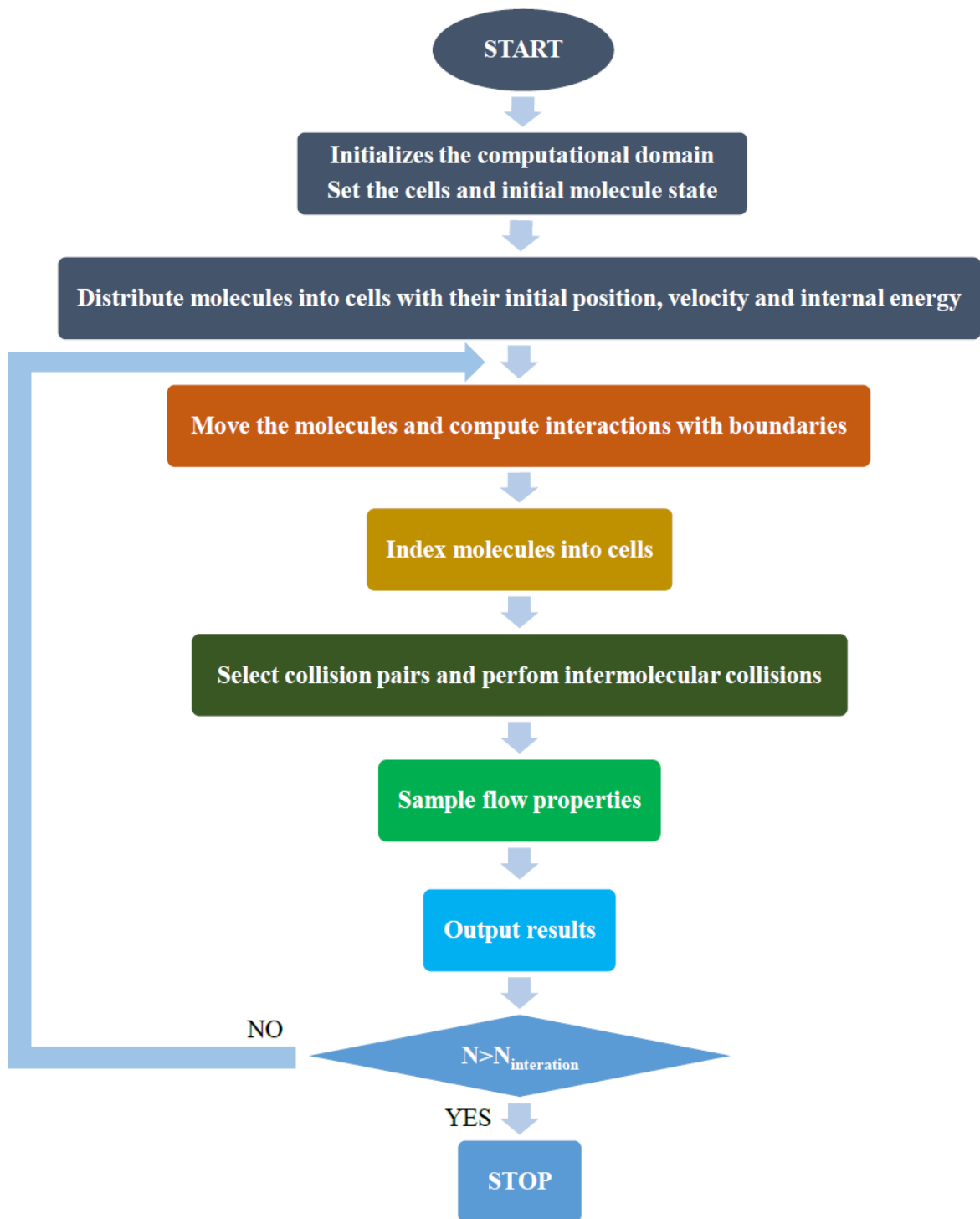


Figure 2.2 - Flow Chart of DSMC method.

average of all values calculated after reaching the steady state. Density, temperature, velocity and internal energy of entering molecules, generated during each time step,

are specified by the known boundary conditions.

After setting the position and velocity of each molecule, the first process occurs, i.e., all molecules are moved through distances appropriate to their velocity components and the discrete time-step. Once a molecule has been moved, its location in the computational domain must be determined. This may be achieved in a number of different ways. For simple cartesian meshes, molecule destinations are quickly computed, and the new cell is computed by using indexing schemes (BIRD, 1994). For structured and unstructured grids, efficient particle tracing schemes are outlined by Dietrich (DIETRICH, 1990) and Laux (LAUX, 1997), respectively. Nevertheless, for more complex grids, such as hexahedral or tetrahedral, ray-tracing techniques can be used to determine the particle position (WILMOTH et al., 1996; NANCE et al., 1997; SHU et al., 2005).

After establishing the location of the molecules, appropriate action is taken if the molecule crosses boundaries as solid surfaces, outer boundary, lines or surfaces of symmetry. Molecules crossing the side of the computational domain are removed from the flow. New molecules are introduced to the simulation at the outer boundaries of the computational domain for freestream boundary conditions or from within the domain from sources. Collisions with surfaces can be treated as being either fully specular, fully diffuse or some combination of the two. The microscopic boundary conditions are specified by the behaviour of the individual molecules according to the conservation laws, rather than in terms of the distribution function. Such application allows the DSMC method to be extended to include physical effects such as chemical reactions, catalytic walls, radiation effects and ionized flows by inserting modifications in the basic algorithm.

The next step involves the second DSMC process. Molecules must be indexed and tracked for the two subsequent procedures: calculation of collisions and sampling the flowfield. For the selection and calculation of intermolecular collisions, each cell must be given a base index from which all other molecules in the cell can be reached through a cross-reference list. Bird (BIRD, 1976) proposed a fast indexing scheme in the original version of the DSMC algorithm. A different indexing scheme was presented by Cybyk et al. (CYBYK et al., 1995). Their indexing scheme combines the DSMC method with the Monotonic Lagrangian Grid (MLG). The MLG maintains a direct correspondence between the indexing and the position of the molecules. The basic idea is to keep molecules that are close in physical space close in index space and hence close in computer memory.

The third step simulate the collisions. It is a probabilistic process that sets DSMC apart from deterministic simulation methods such as molecular dynamics. Several different collision modeling schemes have been formulated and applied in the DSMC method. Among them, one has the time-counter (TC) technique (BIRD, 1976), Nanbu scheme (NANBU, 1986), null-collision (NC) technique (KOURA, 1986), no-time-counter (NTC) technique (BIRD, 1989) and the generalized scheme (ABE, 1989) of the no-time-counter technique. The probability of a collision between two molecules in a homogenous gas is proportional to the product of their relative speed and total collision cross-section. The mean value of the product is calculated for each cell, and the maximum value is also recorded. The collision pairs is then chosen by using the acceptance-rejection method. The probability of a particular pair of molecules being chosen depends on the ratio of their product to the maximum product. However, this procedure would have a computation time directly proportional to the square of the total number of molecules in the cell. For this reason the NTC scheme proposed by Bird (BIRD, 1989) for the DSMC is the preferred model currently used along with the subcell approach. The time step, the cell volume and the number of molecules resident in the cell will determine the number of candidate collision pairs that will be evaluated. The molecules are randomly selected as collision partners with the restriction that their mean separations be a fraction of the molecular mean free path. This restriction is enforced by selecting collision pairs from the list of molecules in the same subcell. The DSMC method evaluates individual collision in a probabilistic basis, conserving momentum and energy.

Finally, the fourth step is completed by considering the sampling of the macroscopic flow properties. Macroscopic flow properties such as density, velocity, pressure and temperature are computed by appropriate averaging of the microscopic state of molecules in each cell.

### 2.2.2 Molecular Models

One of the most important inputs to a DSMC simulation is the molecular model that specifies the interaction between the simulated molecules (VENKATRAMAN; ALEXEENKO, 2010). Several molecular models have been proposed during years to simulate different physical situations. Figure. 2.3 shows the timeline of the phenomenological molecular models. The development of phenomenological models requires the knowledge of what is physically significant and what is not (BIRD, 1998). No model is universally applicable and the choice of a particular model is a tradeoff between its capability to approximate a physical situation and the computational

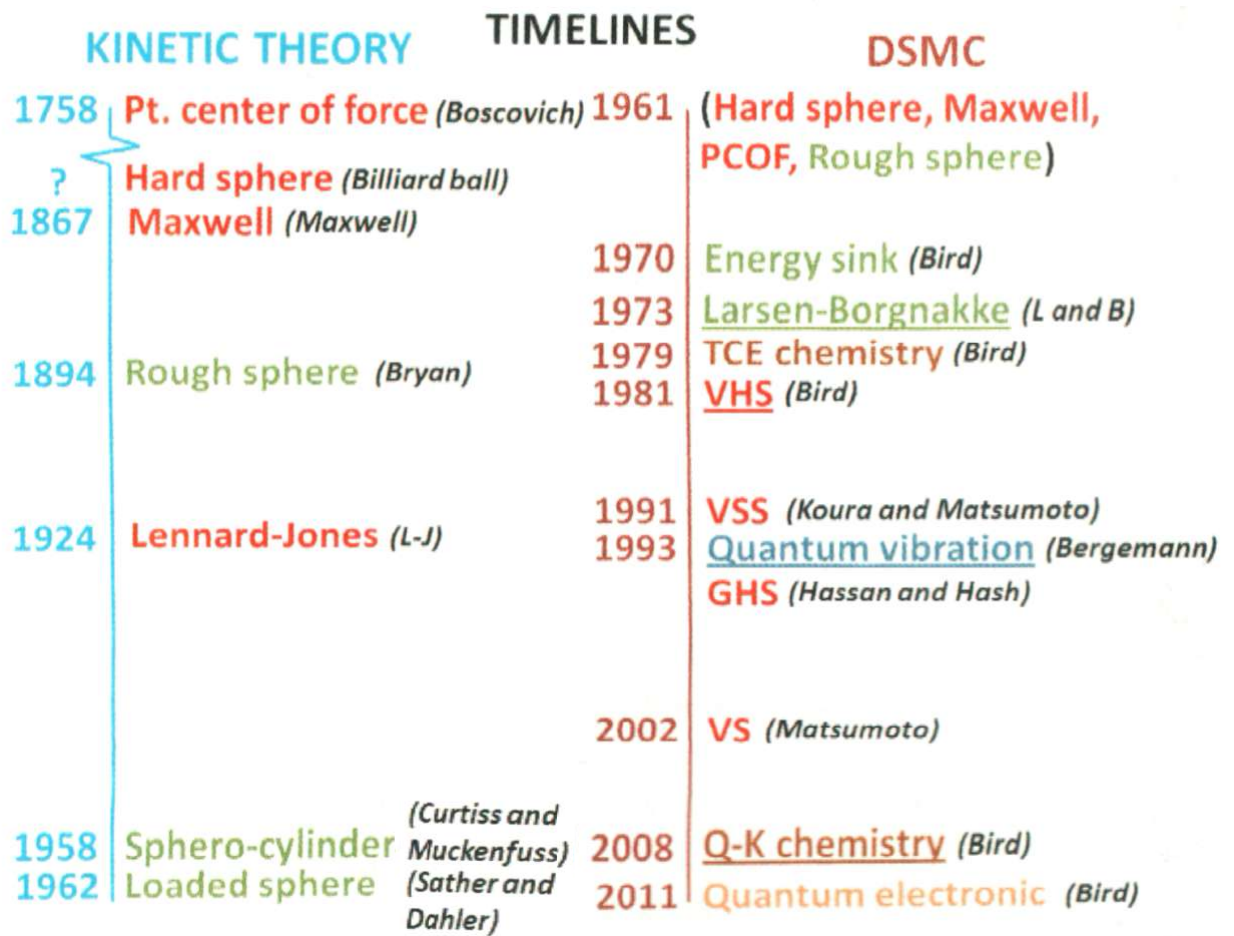


Figure 2.3 - Phenomenological models timeline. Adapted from Bird (BIRD, 2013).

requirements/constraints, among other factors (PRASANTH; KAKKASSERY, 2006).

A simple molecular model that is accurate enough for most hypersonic calculations is the inverse power potential. The intermolecular force potential is modeled as an inverse power repulsive force by,

$$F = \frac{k}{r^\eta} \quad (2.3)$$

where  $r$  is the distance between colliding molecules and  $k$  and  $\eta$  are constants characterizing the molecule.

Setting  $\eta$  equals 5, 9, and  $\infty$ , one obtain the Maxwell, Inverse Power Law or Hard Sphere model.

Simulations involving engineering problems usually employ millions, billions or even trillions of collisions. Faced with this fact, it becomes imperative to employ a simple interaction model. The most common molecular models used in DSMC include the Hard Sphere (HS) and Variable Hard Sphere (VHS) models. Both disregard the large range attractive force that exists between molecules.

In the HS model, also called billiard ball model, the collision cross section is invariant for a single gas species, the scattering angle is isotropic, and the post-collision relative velocity is sampled from a uniform solid angle distribution. However, such a model is not realistic because its total collision cross-section  $\sigma_T$  does not depend on the relative velocity of the colliding molecules. When the intermolecular force law is given by Eqs. 2.3, the Chapman-Enskog theory yields a direct relationship between the coefficient of viscosity and the gas temperature given by,

$$\mu \sim T^s \tag{2.4}$$

$$\frac{1}{2} < s \leq 1 \tag{2.5}$$

$$w = \frac{2}{\eta - 1} \tag{2.6}$$

$$s = w + \frac{1}{2} \tag{2.7}$$

Finally,

$$\mu \sim T^{\frac{2}{\eta-1} + \frac{1}{2}} \tag{2.8}$$

According to Eqs. 2.8, the coefficient of viscosity has a fixed temperature exponent of 1, 0.75 and 0.5 for Maxwellian, inverse power law and hard sphere models, respectively (BIRD, 1981). The hard sphere and Maxwellian models are theoretical gases which can be viewed as the limiting cases for the behavior of a real gas since for almost all real gases  $s$  is generally in the range from 0.6 to 0.9.

The VHS model, introduced by Bird (BIRD, 1981), is characterized by the well-

defined molecular diameter as well as the classical hard sphere scattering law, i.e., all directions are equally possible for the post-collision velocity in the center-of-mass frame of reference. However, the molecular diameter  $d$  is an inverse power law function of the relative collision energy between the colliding molecules. Thus, the total collision cross section  $\sigma_T$  is allowed to vary with the relative speed of colliding molecules as follows,

$$\frac{\sigma_T}{\sigma_{T_{ref}}} = \left( \frac{c_r^2}{c_{r_{ref}}^2} \right)^w \quad (2.9)$$

where  $w = 2/(\eta - 1)$ ,  $\sigma_T$  is the total cross section and  $c_r$  is the relative speed of the colliding molecules.

It should be mentioned in this context that the inverse power-law exponent  $\eta$  and the reference values are calculated by matching the viscosity of the simulated gas to that of its real counterpart.

Koura and Matsumoto (KOURA; MATSUMOTO, 1991; KOURA; MATSUMOTO, 1992) further improved the VHS model by introducing the Variable Soft Sphere (VSS) molecular model. The VSS model accounts for the anisotropic post-collision scattering law. The second free parameter introduced by the post-collision scattering dynamics in the VSS model is chosen in order to reproduce correctly the actual viscosity and diffusion coefficients of the gases.

Hassan and Hash (HASH; HASSAN, 1993b) introduced the Generalized Hard Sphere (GHS) molecular model, which is an extension of the VHS and VSS models. The GHS model accounts for both repulsive and attractive parts of the particle-particle interaction. In this model, molecules scatter like hard sphere, as was considered in the VHS model. Since the GHS model is capable of reproducing the effects of the attractive portion of an interaction potential, then it is appropriate to simulate low temperature flows, which are dominated by the attractive collisions (HASH; HASSAN, 1993a; HASH et al., 1994; KUNC et al., 1995).

### 2.2.3 Collision Models

Several different collision-modeling schemes have been formulated and applied in the DSMC method. Among them, the time-counter (TC) technique (BIRD, 1976), Nanbu scheme (NANBU, 1986), null-collision (NC) technique (KOURA, 1986), no-time-counter (NTC) technique (BIRD, 1989) and the generalized scheme (ABE, 1993)

of the no-time-counter technique. For the purpose of this work, only the TC and NTC schemes will be described.

The procedures for the establishment of the correct collision rate are based on the cells, while individual collision pairs are chosen in the subcell. The time step  $\Delta t$ , the cell volume  $V_c$ , and the number of molecules  $N$  resident in the cell will determine the number of candidate collision pairs that will be evaluated. From kinetic theory, it may be shown that the number of collisions that must be simulated over a time step  $\Delta t$  is given by,

$$N_{coll} = \frac{1}{2} N \Delta t \overline{n \sigma_T c_r} \quad (2.10)$$

where  $n$  is the number density (BIRD, 1994).

In order to determine the correct total number of collisions during the time step  $\Delta t$ , it would be necessary to compute the average product of the relative speed  $c_r$  and the collision cross section  $\sigma_T$  for all possible pairs of molecules. An algorithm that uses this approach would have a computational time proportional to  $N^2$ , where  $N$  is the total number of simulated molecules. In order to overcome this difficulty, Bird (BIRD, 1976) introduced the parameter  $(\sigma_T c_r)_{max}$ , where the subscript max denotes the largest value for the cell, and should be updated during a binary collision if the real product  $\sigma_T c_r$  were greater than  $(\sigma_T c_r)_{max}$ . Furthermore, the parameter  $(\sigma_T c_r)_{max}$  is used to determine a real collision according to the following three operations:

(1) Two molecules are randomly selected in the cell. The probability that these molecules collide is then given by,

$$P = \frac{\sigma_T c_r}{(\sigma_T c_r)_{max}} \quad (2.11)$$

if this probability is larger than  $R_f$ , where  $R_f$  is a uniform random number in the range  $[0,1]$  then the pair of molecules is accepted for collision. Otherwise, a new pair is randomly selected and the procedure is repeated. This is the acceptance-rejection method described by Bird (BIRD, 1994) to select collision partners.

(2) If the pair of simulated molecules is accepted for collision, then a time counter for the current cell is advanced by the amount

$$\delta t = \frac{2}{Nn\sigma_{Tc_r}} \quad (2.12)$$

A number of collisions is calculated in the cell until the sum of a number of  $\delta t$ 's is just greater than the time step  $\Delta t$ . This is the time-counter (TC) scheme proposed by Bird (BIRD, 1976).

In the *TC* scheme, the total number of collision within the given time step  $\delta t$ 's depends on the product  $\sigma_{Tc_r}$  related to the collision pairs, which are randomly chosen. In addition to that, it is not possible to calculate the total number of collisions at the beginning of the iteration step. Consequently, a complete vectorization of the collision process is not possible. The difficulty in treating the *TC* scheme is due to the vector dependency associated with the implementation of summing several values of  $\delta t$  given by Eq. (2.12) (BAGANOFF et al., 1993).

In the *NTC* scheme, the time increment related to a randomly chosen pair of simulated molecules is independent of the real product  $\sigma_{Tc_r}$ . The parameter  $(\sigma_{Tc_r})_{max}$  is fixed during a time iteration  $\delta t$  and modified after performing all collisions. The idea of a time counter is replaced with the expression for the total number of collisions  $N_{coll}$  to be sampled in each cell by,

$$N_{coll} = \frac{1}{2} \frac{N\bar{N}F_N(\sigma_{Tc_r})_{max}\delta t}{V_c} \quad (2.13)$$

where  $F_N$  is the number of real molecules represented by a single simulated molecule,  $N$  is a fluctuating quantity and  $\bar{N}$  is an average value. The probability of collision for each pair sampled is again given by Eq. (2.11).

The *NTC* scheme was introduced to alleviate difficulties found with the *TC* scheme in regions of highly nonequilibrium flows such as strong shock waves. The problem is related to the acceptance of an unlikely collision pair with a relatively small collision probability (one with a very small value for  $\sigma_{Tc_r}$ ). Under such conditions, the time increment determined by Eq. (2.12) may substantially exceed the decoupled time step  $\delta t$ .

Recently Bird (BIRD, 2007) proposed the substitution of  $N\bar{N}$  by  $N(N-1)$ .

### 2.2.4 Binary Elastic Collisions

It was pointed out in the previous subsections that DSMC is subjected to the restriction of dilute gases. For dilute gases, the intermolecular collision are considered as being binary collisions. Also, an elastic collision is defined as one in which there is no interchange of translational and internal energy.

Given two molecules, their pre-collision velocities can be denoted by  $\vec{c}_1$  and  $\vec{c}_2$ . Getting their physical properties and orientation of their trajectories, one can determine their post-collision velocities  $\vec{c}_1^*$  and  $\vec{c}_2^*$ . Both momentum and energy must be kept in the collision process. In this manner, for the molecular masses denoted by  $m_1$  and  $m_2$  and the velocity of the centre of mass of the pair of molecules denoted by  $c_m$ , one has the following equations:

$$m_1 \vec{c}_1 + m_2 \vec{c}_2 = m_1 \vec{c}_1^* + m_2 \vec{c}_2^* = (m_1 + m_2) \vec{c}_m \quad (2.14)$$

$$m_1 \vec{c}_1^2 + m_2 \vec{c}_2^2 = m_1 \vec{c}_1^{*2} + m_2 \vec{c}_2^{*2} \quad (2.15)$$

Equation (2.14) shows that the centre of mass velocity is not affected by the collision. The values of pre- and post-collisions, and the relative velocity between the molecules can be defined by:

$$\vec{c}_r = \vec{c}_1 - \vec{c}_2 \quad (2.16)$$

$$\vec{c}_r^* = \vec{c}_1^* - \vec{c}_2^* \quad (2.17)$$

By combining Eq. (2.14) with Eq. (2.15) and (2.16), one obtains the following expressions:

$$\vec{c}_1 = \vec{c}_m + \frac{m_2}{m_1 + m_2} \vec{c}_r \quad (2.18)$$

$$\vec{c}_2 = \vec{c}_m - \frac{m_1}{m_1 + m_2} \vec{c}_r \quad (2.19)$$

The pre-collision velocities relative to the centre of mass are  $\vec{c}_1 - \vec{c}_m$  and  $\vec{c}_2 - \vec{c}_m$ . Similarly, the post-collision velocities are given by:

$$\vec{c}_1^* = \vec{c}_m + \frac{m_2}{m_1 + m_2} \vec{c}_r^* \quad (2.20)$$

$$\vec{c}_2^* = \vec{c}_m - \frac{m_1}{m_1 + m_2} \vec{c}_r^* \quad (2.21)$$

Based on these equations, it is seen that the post-collision velocities are also anti-parallel in the centre of mass frame of reference.

The conservation of angular momentum requires that the projected distance between the post-collision velocities be equal to the projected distance between the pre-collision velocities. As a result, Eqs. (2.18),(2.19) with (2.20) and (2.21) show that:

$$m_1 \vec{c}_1^{\perp} + m_2 \vec{c}_2^{\perp} = (m_1 + m_2) \vec{c}_m^{\perp} + m_r \vec{c}_r^{\perp} \quad (2.22)$$

$$m_1 \vec{c}_1^{*\perp} + m_2 \vec{c}_2^{*\perp} = (m_1 + m_2) \vec{c}_m^{\perp} + m_r \vec{c}_r^{*\perp} \quad (2.23)$$

where  $m_r$  is called the reduced mass and is given by:

$$m_r = \frac{m_1 m_2}{m_1 + m_2} \quad (2.24)$$

By comparing Eqs. (2.22) and (2.23) with the energy conservation Eq. (2.15), it appears that the magnitude of the relative velocity is unchanged by the collision, i.e.,

$$|\vec{c}_r^*| = |\vec{c}_r| \quad (2.25)$$

Since  $\vec{c}_m$  and  $\vec{c}_r$  can be calculated from the pre-collision velocities, then the determination of post-collision velocity is reduced to calculating the change in direction of the  $\chi$  relative to the velocity vector. If  $\vec{F}$  is the force between two spherically symmetric points, and  $\vec{r}_1$  and  $\vec{r}_2$  their position vectors, the equations of motion of

the molecules are as following:

$$m_1 \ddot{\vec{r}}_1 = \vec{F} \quad (2.26)$$

$$m_2 \ddot{\vec{r}}_2 = \vec{F} \quad (2.27)$$

By combining these two equations, one has,

$$m_1 m_2 (\ddot{\vec{r}}_1 - \ddot{\vec{r}}_2) = (m_1 + m_2) \vec{F} \quad (2.28)$$

By denoting the relative velocity vector by  $\vec{r}$ , then one obtains,

$$m_r \ddot{\vec{r}} = \vec{F} \quad (2.29)$$

In this way, the motion of the molecule of mass  $m_1$  relative to the molecule of mass  $m_2$  is equivalent to the movement of the molecule of mass  $m_r$  relative to a fixed center of force.

For completeness, the aforementioned transformations are illustrated in Fig. 2.4. According to these plots, the transformation from the centre of mass coordinate system changes a three-dimensional trajectory into a two-dimensional trajectory, which is symmetric about the apse line  $AA'$ . The two trajectories are reduced to one in the further transformation to the reduced mass frame of reference, and this trajectory remains symmetrical about the transformed apse line, which passes through the scattering centre  $O$ .

This symmetry reflects the symmetry of the equations related the pre- and post-collision velocities. Another consequence of this symmetry becomes apparent if one considers a collision between two molecules of velocities  $\vec{c}_1$  and  $\vec{c}_2$ , and such that the separation of their undisturbed trajectories in the center of mass frame of reference is again equal to  $b$ . This collision results in a post-collision velocities of  $\vec{c}_1$  and  $\vec{c}_2$  and is called the inverse of the original or direct collision.

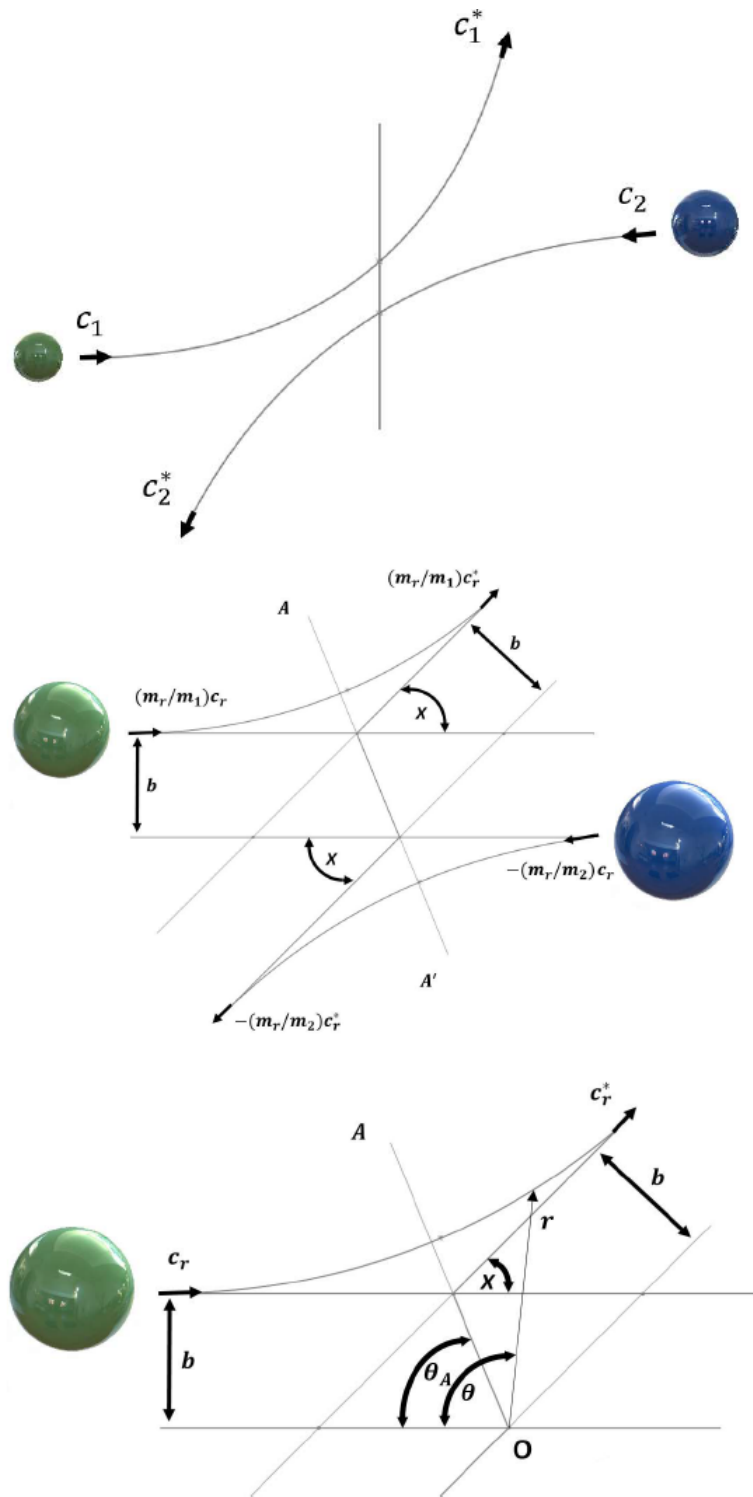


Figure 2.4 - Binary collision in the centre of mass frame reference.  
Adapted from Bird (BIRD, 1994).

### 2.2.5 Internal Degrees-of-Freedom

One of the most significant effects observed in rarefied flows is the presence of a large degree of nonequilibrium between the various internal energy modes of the gas. For polyatomic gases, the transfer of energy to and from the internal modes has to be considered. However, energy transfer among translational, rotational and vibrational degrees of freedom cannot be accurately predicted using simple collision models.

The internal energy transfer between the various modes is usually implemented into the DSMC method by the phenomenological model introduced by Borgnakke and Larsen (BORGNAKKE; LARSEN, 1975), named as Larsen-Borgnakke (LB) statistical model. The essential feature of this model is that a fraction  $\phi$  of translational collisions are assumed to be inelastic, and the remaining  $(1 - \phi)$  collisions are considered as elastic. The fraction  $\phi$  can be interpreted as the average probability of rotational or vibrational energy exchange for translational collisions. This average probability can be determined from measured relaxation times. The relaxation time is a function of the local flow properties and can be related to a relaxation number (or collision number)  $Z$ . The relaxation or collision number  $Z$  is usually defined by,

$$Z = \frac{\tau_i}{\tau_c} \quad (2.30)$$

where  $\tau_i$  is the relaxation time and  $\tau_c$  is the mean collision time.

The relaxation or collision number is the average number of molecular collisions that are required for a particular mode to attain equilibrium energy. In general, the relaxation time  $\tau_i$ , which is usually several times larger than the collision time, is introduced to characterize the relaxation rate given by,

$$\tau_i = \frac{Z_i}{\nu} \quad (2.31)$$

where  $\nu$  is the collision frequency (PRASANTH; KAKKASSERY, 2008).

Once this number is determined, the average probability  $\phi$  for each mode in a given collision is conveniently defined as,

$$\phi = \frac{1}{Z} \quad (2.32)$$

In general, DSMC calculations use the rotational collision number  $Z_R$  on the order of 5. This means that, on average, a molecule rotationally relaxes once every five collisions. This is generally a good engineering approximation. However, more realistic models for rotational collision number as a function of the translational temperature or translational energy have been proposed by Boyd (BOYD, 1990a; BOYD, 1990b; BOYD, 1990c). In the present work, the rotational collision number  $Z_R$  was obtained in a collision energy-based procedure, as suggested by Boyd (BOYD, 1998).

The vibrational relaxation number  $Z_V$  is also computed as a function of the flow properties. The relaxation number can be easily determined if the collision frequency and the relaxation time, Eq. (2.30), are known. The relaxation time of the vibrational mode is usually at least an order of magnitude larger than that associated with the rotational mode of a molecule.

Repartition energy among internal and translational modes is controlled by the Larsen-Borgnakke statistical model (BORGNAKKE; LARSEN, 1975). The Larsen-Borgnakke statistical model can be applied to the vibrational modes through either a classical or a quantum procedure. In the classical procedure, the vibrational energy is treated as a continuous distribution described by a number of vibrational degrees of freedom  $\zeta_V$ , which is fixed. In the quantum procedure, the discrete nature of vibrational spectrum is taken into account, since the vibrational spectrum of real molecules is characterized by large gaps between the neighboring energy levels. The quantum procedure allows sampling of post-collision vibrational energy levels from the discrete form of the Simple Harmonic Oscillator (SHO). This procedure does not require the value of  $\zeta_V$  to be estimated for the whole flowfield. Instead,  $\zeta_V$  varies according to the local energy content of the flow. Both procedures are discussed at length by Bird (BIRD, 1994). Vibrational relaxation number as a function of the collision energy is presented by Boyd and Bergemann (BERGEMANN; BOYD, 1994) and as a function of temperature by Hash and Hassan (HASH; HASSAN, 1993a) and Bird (BIRD, 1998). In the present account, vibrational  $Z_V$  collision number was obtained in a collision temperature-based procedure, as suggested by Bird (BIRD, 2008).

## 2.2.6 Translational-Rotational Energy Exchange

In a gas, molecules are always colliding one to each other, and thus energy is continually being transferred between the various internal modes. These collisions tend

to push the internal distributions toward their equilibrium state. The number of collisions required to bring these modes into equilibrium is called collision number  $Z$ . Each internal mode has a different collision number and it is generally:

$$Z_{Translation} < Z_{Rotation} < Z_{Vibration} \quad (2.33)$$

The vibrational mode is the one who need the greater collision number for reached the equilibrium, followed by rotational and translational.

In the present work, the energy exchange model between the translational and rotational modes proposed by Boyd (BOYD, 1990c) was employed. He proposed a full expression for the average value that is given by:

$$\phi_R \frac{(Z_R)_\infty}{Z_t} = 1 + \frac{\Gamma(2 - \omega)}{\Gamma(3/2 - \omega)} \left( \frac{2kT^*}{m_r c_r^2} \right)^{1/2} \frac{\pi^{3/2}}{2} + \frac{\Gamma(2 - \omega)}{\Gamma(1 - \omega)} \left( \frac{2kT^*}{m_r c_r^2} \right) \left( \frac{\pi^2}{4} + \pi \right) \quad (2.34)$$

where  $(Z_R)_\infty$  is the limiting value,  $Z_t$  is the translational collision number,  $\omega$  is the viscosity index used in the variable hard sphere (VHS) collision model of Bird (BIRD, 1994),  $k$  is the Boltzmann constant,  $T^*$  is the characteristic temperature of the intermolecular potential,  $m_r$  is the reduced mass and  $c_r$  is the relative velocity.

After evaluation of the rotational energy exchange probability, a random number is used to decide whether the collision leads to energy exchange. For those collisions involving rotational energy exchange, the LB model (BORGNAKKE; LARSEN, 1975) is employed to assign new postcollision rotational energies. The LB model assumes local equilibrium and samples postcollision energies from equilibrium distributions. Once the new rotational energy is assigned, the remaining energy is the new translational energy and hence it determines the new post-collision relative speed.

### 2.2.7 Translational-Vibrational Energy Exchange

The vibrational collision number is extremely dependent on temperature. The use of a uniform value in a cell means that significant effects due to the distribution of collision energies within that cell are not taken into account (BIRD, 2001). This problem was solved using the collision temperature quantized in the same fashion as the vibrational energy, thereby attaining the exact vibrational equipartition. DSMC

implementations generally adopt the Chapman and Cowling (CHAPMAN; COWLING, 1970) definitions of non-equilibrium temperatures and relaxation times (BIRD, 2001). The variation of the vibrational collision number, introduced by Bird (BIRD, 2008), is expressed as a function of temperature by the following equation,

$$Z_v = Z_d \left( \frac{\Theta_d}{T} \right)^w \left[ \frac{Z_c}{Z_d} \left( \frac{\Theta_v}{\Theta_d} \right)^w \right]^{[(\frac{\Theta_d}{T})^{\frac{1}{3}} - 1] / [(\frac{\Theta_v}{\Theta_d})^{\frac{1}{3}} - 1]} \quad (2.35)$$

where  $\Theta_v$  is the characteristic temperature of vibration,  $\Theta_d$  is the characteristic temperature of dissociation,  $Z_c$  and  $Z_d$  are their related collision numbers, respectively.

According to Bird (BIRD, 2008), Eq. (2.35) leads to unphysical collision numbers, i.e., less than unit at the dissociation temperature, for instance, about 0.6 for oxygen and 0.15 for nitrogen. This is physically impossible and a new equation proposed by Bird (BIRD, 2008) was implemented setting the second temperature to an arbitrary temperature,  $T_{ref}$ , where the collision number is  $Z_{ref}$ .

$$Z_v = Z_d \left( \frac{\Theta_d}{T} \right)^w \left[ Z_{ref} \left( \frac{\Theta_d}{T_{ref}} \right)^{-w} \right]^{[(\frac{\Theta_d}{T})^{\frac{1}{3}} - 1] / [(\frac{\Theta_d}{T_{ref}})^{\frac{1}{3}} - 1]} \quad (2.36)$$

### 2.2.8 Boundary Conditions

In principle, there are two basic types of boundary conditions in the gas dynamics problems. One of them is specified by quantities given in the undisturbed freestream, and the other one is specified at a solid surface, where molecules interact or reflect directly.

The first condition is easily represented as a gas in equilibrium is moving with an imposed velocity. The molecular velocity distribution can be given as Maxwellian with an imposed velocity. This distribution holds for any ideal gas independently of the type of forces between molecules. The second condition depends on the treatment of gas-surface interactions. The influence of the gas-surface-interaction model on the aerodynamic forces and heat transfer increases substantially as the gas rarefaction increases. Therefore, the correct choice of the model for calculating hypersonic rarefied flows plays an important role.

Three models of gas-surface interactions may be employed in the DSMC method: (1) specular reflection, (2) diffuse reflection, and (3) a combination of these two methods.

In a specular reflection, molecules are reflected like a perfectly elastic sphere with reversal of the normal component of velocity and no change in either the parallel components of velocity and energy. In a diffuse reflection, the molecules are reflected equally in all directions with a complete thermal accommodation. The final velocity components of the reflected molecules are independent of their incident velocity and direction. The combination of diffuse reflection with specular reflection (Maxwell model) introduces a single parameter  $f$  to indicate the fraction of those molecules reflected diffusely in a completely accommodated fashion according to a Maxwellian distribution based on wall temperature, the remaining fraction,  $(1 - f)$ , is assumed to reflect specularly.

The Maxwell model was followed by the introduction of three accommodation coefficients that describe the degree of accommodation of the incident normal momentum, tangential momentum and kinetic energy to the surface. A variety of definitions for accommodation coefficients exist in the literature. The traditional definition is usually expressed as being,

$$\alpha_r = \frac{e_i - e_r}{e_i - e_w} \quad (2.37)$$

$$\alpha_n = \frac{p_i - p_r}{p_i - p_w} \quad (2.38)$$

$$\sigma_n = \frac{\tau_i - \tau_r}{\tau_i} \quad (2.39)$$

where  $e_i$ ,  $\tau_i$  and  $p_i$  are fluxes of energy and of tangential and normal momentum, respectively, incident on the surface;  $e_r$ ,  $\tau_r$  and  $p_r$  are the fluxes of these quantities reflected from the surface; and  $e_w$  and  $p_w$  ( $\tau_w = 0$ ) are the fluxes which would be reflected by a gas in complete Maxwellian equilibrium with the surface.

Data from many experiments show that molecules reflected or reemitted from solid surfaces present lobular distributions under high vacuum conditions and are poorly represented by the Maxwell model. However, this model is widely used because it satisfies the principle of detailed balance or reciprocity. Detailed balance means that at equilibrium every molecular process and its inverse process must individually balance.

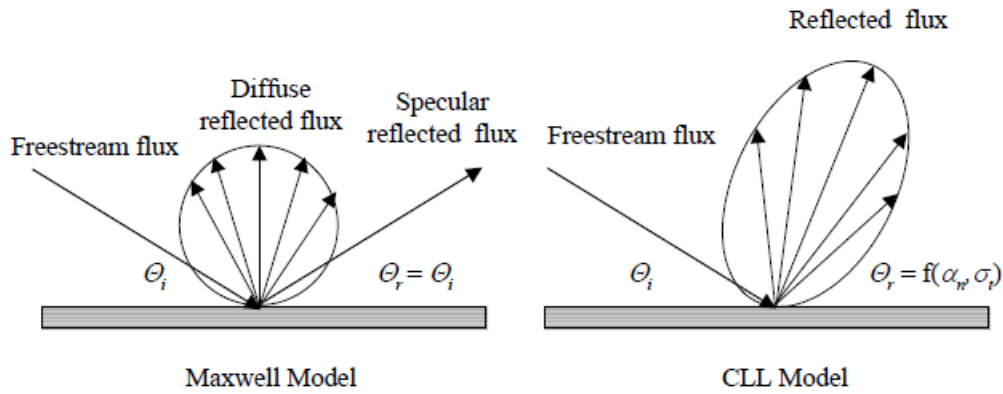


Figure 2.5 - Drawing illustration of the Maxwell and CLL reflection model.  
Adapted from Leite (LEITE, 2009).

A phenomenological model that satisfies detailed balance and has demonstrated improvement over the Maxwell model has been proposed by Cercignani and Lampis (CERCIGNANI; LAMPIS, 1971) (C-L model). This model is based on the definition of the accommodation coefficients  $\sigma_t$  and  $\alpha_n$  that represent the accommodation coefficients for the kinetic energy associated with the normal and tangential components of velocity. The C-L model provides a continuous spectrum of behavior from specular reflection at one end to diffuse reflection with complete energy accommodation at the other, and produces physically realistic distributions of direction and energy reemitted molecules. Lord (LORD, 1991) has shown that the C-L model is suited for the DSMC method, and described how to incorporate it into the DSMC method. The DSMC method with Lord's implementation is referred as the Cercignani-Lampis-Lord (CLL) method.

Figure 2.5 displays a schematic comparison of the Maxwell reflection model and the CLL reflection model. The C-L model has also been extended for covering diffuse scattering with partial energy accommodation and for simulating the accommodation of vibrational energy of a diatomic molecule modeled as simple harmonic oscillator (LORD, 1991) and an anharmonic oscillator (LORD, 1994).



### 3 COMPUTATIONAL PROCEDURE

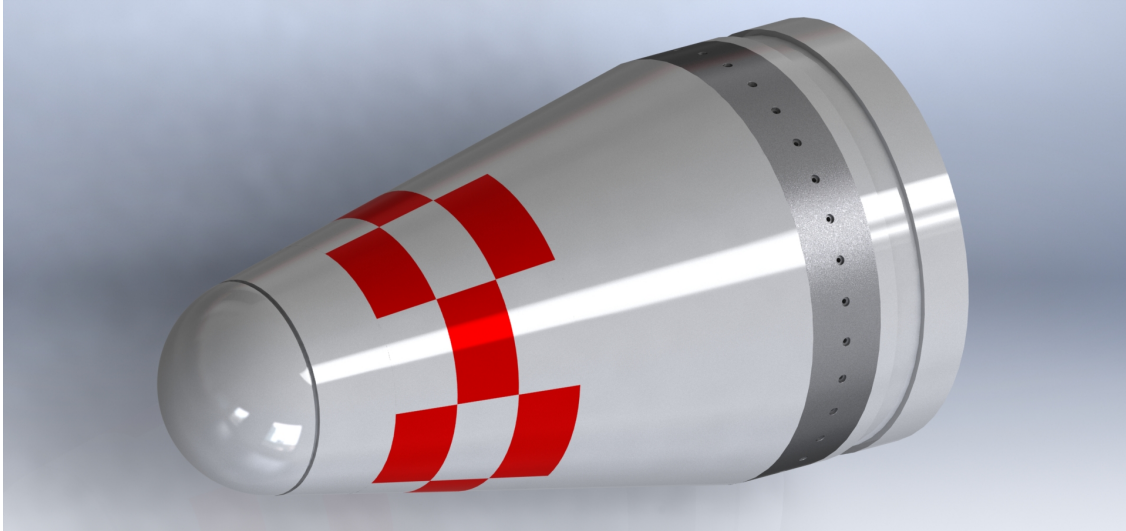
#### 3.1 Geometry Definition

In the present account, the reentry capsule is an axisymmetric design consisting of a spherical nose with a 11.4-degree half-angle conical afterbody. The nose radius  $R$  is 0.2678  $m$ , the afterbody base has a radius  $R_B$  of 0.5035  $m$ , and the total length  $l$  is 1.410  $m$ . A gap with a length-to-depth ( $L/H$ ) ratio of 1, 1/2 and 1/4 is positioned at the junction of the spherical nose and the conical afterbody. Figure 3.1 illustrates schematically the capsule shape and the main important physical and geometric parameters related to the hypersonic flow on the capsule.

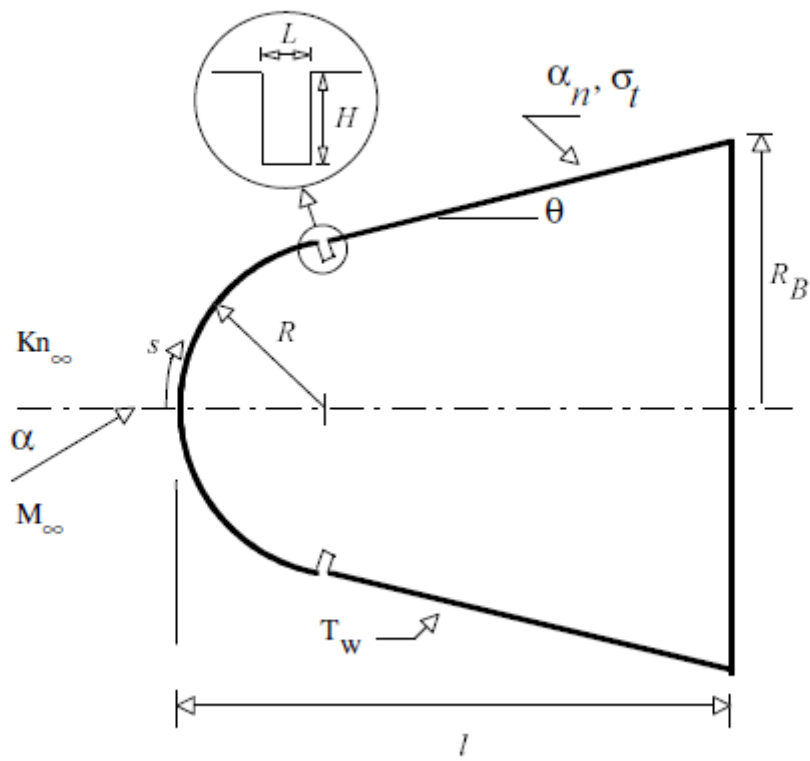
Based on the Fig. 3.1, the main physical parameters are defined as follows:  $M_\infty$  is the freestream Mach number,  $Kn_\infty$  stands for the Knudsen number,  $T_w$  is the wall temperature,  $\alpha_n$  and  $\alpha_t$  are parameters related to the gas-surface interaction,  $\alpha$  is the angle of attack,  $\Theta$  corresponds to the angle of the afterbody, and, finally,  $s$  is the arc length along the body surface measured from the stagnation point. It should be remarked that this geometry corresponds to the small ballistic reentry Brazilian vehicle named SARA (acronyms for SATélite de Reentrada Atmosférica).

According to the current literature, the gap depth  $H$  is generally of the order of 2.54 to 25.4  $mm$  (WIETING, 1970; SCOTT; MARAIA, 1979; BERTIN; GOODRICH, 1980; GAI; MILTHORPE, 1995; ENGBLOM; GOLDSTEIN, 1996; GROTOWSKY; BALLMANN, 2000; JACKSON et al., 2001; EVERHART et al., 2006; HINDERSKS; RADESPIEL, 2006; MOHRI; HILLIER, 2011). Based on this range, a depth  $H$  of 12  $mm$  and a length  $L$  of 12  $mm$ , 6  $mm$ , and 3  $mm$  defined the gap dimensions in the present work. This set of gaps corresponds to  $L/H$  ratio of 1, 1/2, and 1/4. In addition, in order to account for the bluntness effect, three different nose radius for the reentry vehicle were investigated, i.e.,  $R$ ,  $R/2$ , and  $R/4$ . These nose radii correspond to  $H/R$  of 0.045, 0.090, and 0.179, respectively. For convenience and later reference, Tab. 3.1 tabulates the cases investigated in this work.

In order to obtain a better understanding of the gap length-to-depth ( $L/H$ ) ratio effects on the flowfield structure and on the aerodynamic surface properties of a capsule, it becomes imperative to compare these properties with those of a capsule without such discontinuities, i.e., without gaps. Thus, the solution obtained for a vehicle without discontinuities will represent a benchmark solution when compared to the cases with gaps.



(a)



(b)

Figure 3.1 - Drawing illustrating a (a) schematic view of the capsule, and (b) the important parameters.

Table 3.1 - Geometric cases investigated.

Case	R [mm]	L [mm]	H [mm]	H/R	L/H
1	267.80	12	12	0.045	1.00
2	267.80	6	12	0.045	0.50
3	267.80	3	12	0.045	0.25
4	133.90	12	12	0.0225	1.00
5	133.90	6	12	0.0225	0.50
6	133.90	3	12	0.0225	0.25
7	66.95	12	12	0.01125	1.00
8	66.95	6	12	0.01125	0.50
9	66.95	3	12	0.01125	0.25

### 3.2 Freestream Flow conditions

The freestream flow conditions used for the numerical simulation of flow past the capsule are those given by Santos (SANTOS, 2012), which correspond to those experienced by the capsule SARA during its reentry trajectory in the Earth's atmosphere for 100, 90, and 80 *km* of altitude, summarized in Tabs 3.2, 3.3 and 3.4 respectively. This range of altitude is associated with the transition flow regime, which is characterized by the overall Knudsen number of the order of or larger than  $10^{-1}$ .

Table 3.2 - Freestream flow conditions for 100 km.

Properties	Values	Unit
Velocity ( $U_\infty$ )	7862.24	<i>m/s</i>
Temperature ( $T_\infty$ )	210.02	<i>K</i>
Pressure ( $p_\infty$ )	$3.007 \times 10^{-2}$	<i>N/m<sup>2</sup></i>
Density ( $\rho_\infty$ )	$4.9895 \times 10^{-7}$	<i>kg/m<sup>3</sup></i>
Number density ( $n_\infty$ )	$1.0372 \times 10^{19}$	<i>m<sup>-3</sup></i>
Viscosity ( $\mu_\infty$ )	$1.1860 \times 10^{-5}$	<i>Ns/m<sup>2</sup></i>
Mean free path ( $\lambda_\infty$ )	$1.236 \times 10^{-1}$	<i>m</i>

The velocity-altitude map for the SARA capsule (SANTOS, 2012) is demonstrated in Fig. 3.2. This velocity-altitude map was generated based on predefined conditions, such as an initial velocity of 7,626.30 *m/s*, an initial altitude of 300 *km*, a drag coefficient of 0.80, a lift coefficient of 0.0, a reference area of 0.785 *m<sup>2</sup>*, a total mass of 150 *kg*, and finally, a gravity acceleration of 8.95 *m/s<sup>2</sup>*.

According to Fig. 3.2, for altitudes of 100, 90, and 80 *km*, the freestream velocity  $V_\infty$  is 7862, 7864, and 7820 *m/s*, respectively. These values correspond to a freestream

Table 3.3 - Freestream flow conditions for 90 km.

Properties	Values	Unit
Velocity ( $U_\infty$ )	7864.1	$m/s$
Temperature ( $T_\infty$ )	180.65	$K$
Pressure ( $p_\infty$ )	$1.6438 \times 10^{-1}$	$N/m^2$
Density ( $\rho_\infty$ )	$3.1705 \times 10^{-6}$	$kg/m^3$
Number density ( $n_\infty$ )	$6.590 \times 10^{19}$	$m^{-3}$
Viscosity ( $\mu_\infty$ )	$1.10998 \times 10^{-5}$	$Ns/m^2$
Mean free path ( $\lambda_\infty$ )	$1.945 \times 10^{-2}$	$m$

Table 3.4 - Freestream flow conditions for 80 km.

Properties	Values	Unit
Velocity ( $U_\infty$ )	7820.1	$m/s$
Temperature ( $T_\infty$ )	180.65	$K$
Pressure ( $p_\infty$ )	1.0365	$N/m^2$
Density ( $\rho_\infty$ )	$1.9992 \times 10^{-5}$	$kg/m^3$
Number density ( $n_\infty$ )	$4.1562 \times 10^{20}$	$m^{-3}$
Viscosity ( $\mu_\infty$ )	$1.1001 \times 10^{-5}$	$Ns/m^2$
Mean free path ( $\lambda_\infty$ )	$3.085 \times 10^{-3}$	$m$

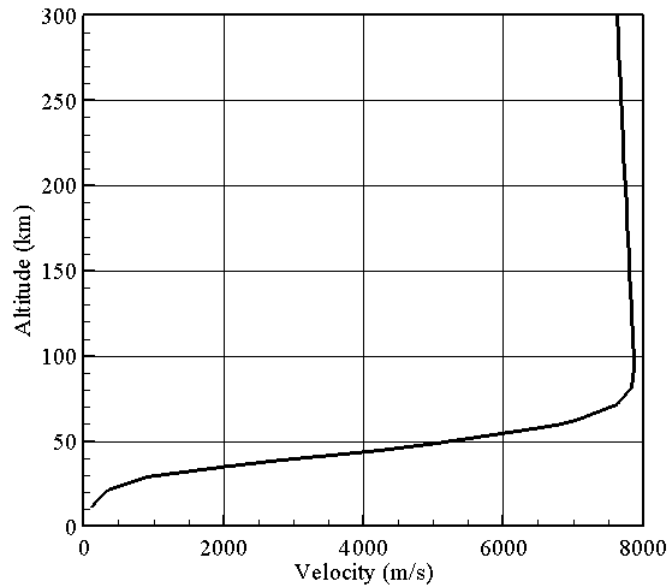


Figure 3.2 - Velocity-altitude map for the SARA capsule.

Mach number  $M_\infty$  of 27.1, 29.2, and 29.0, respectively. In the present account, the capsule surface was kept at a constant wall temperature  $T_w$  of 880  $K$  for all cases investigated. In addition, a flow with a zero-degree angle of attack was assumed in

this investigation.

Under the aforementioned conditions, the overall Knudsen number,  $Kn_\infty$ , by considering the nose radius  $R$  as the characteristic length, corresponds to 0.4615, 0.0726, and 0.0115 for altitude of 100, 90, and 80 *km*, respectively. In addition, the Reynolds number  $Re_\infty$  is around 92, 609, and 15249, for altitude of 100, 90, and 80 *km*, respectively, also based on conditions in the undisturbed stream.

### 3.3 Numerical Simulation Conditions

In the present investigation, molecular collisions was modeled by using the variable hard sphere (VHS) molecular model, and the No-Time-Counter (NTC) method was employed as a collision-sampling technique. The energy exchange between kinetic and internal modes is controlled by the Larsen-Borgnakke (LB) phenomenological model (BORGNAKKE; LARSEN, 1975). These inelastic collisions ensure the energy exchange between the various internal modes. Furthermore, they tend to push the internal energy distributions toward their equilibrium state. The relaxation numbers, which is the number of collisions, on average, required to bring these modes into equilibrium, were assumed to have a temperature dependence as cited earlier and defined by Boyd (BOYD, 1990c) for rotation and Bird (BIRD, 2008) for vibration.

Simulations are performed using a nonreactive air as working fluid with two chemical species,  $N_2$  and  $O_2$ . The freestream coefficient of viscosity  $\mu_\infty$  and freestream mean free path  $\lambda_\infty$  are evaluated from a consistent definition (BIRD, 1983) by using the VHS collision model with the temperature exponent  $s$  (Eq. 2.4) equal to 0.74 and 0.77 for  $N_2$  and  $O_2$ , respectively. Table 3.5 summarizes the air characteristics used in the DSMC calculations.

The computational domain used for the calculation is made large enough so that the capsule disturbances do not reach the upstream and side boundaries, where freestream conditions are specified. A schematic view of the computational domain is shown in Fig. 3.3. Advantage of the flow symmetry is taken into account, and molecular simulation is applied to one-half of a full configuration.

The computational domain around the capsule is divided into four regions (R1, R2, R3 and R4), which are subdivided into computational cells. The cell provides a convenient reference for the sampling of the macroscopic gas properties. In addition, the cells are further subdivided into subcells. The subcell provides a reference for the collision process. The collision partners are selected from the same subcell in

Table 3.5 - Characteristics of simulated air for DSMC calculations

Properties	Values	Unit
Working fluid	$N_2 + O_2$	
Molecular weight	28.96	<i>kg/kgmole</i>
Molecular mass of $O_2$	$5.312 \times 10^{-26}$	<i>kg</i>
Molecular mass of $N_2$	$4.650 \times 10^{-26}$	<i>kg</i>
Molecular diameter of $O_2$	$4.070 \times 10^{-10}$	<i>m</i>
Molecular diameter of $N_2$	$4.170 \times 10^{-10}$	<i>m</i>
Moles fraction of $O_2$	0.237	
Moles fraction of $N_2$	0.763	
Viscosity index of $O_2$	0.77	
Viscosity index of $N_2$	0.74	
Degrees of freedom of $O_2$	5 to 7	
Degrees of freedom of $N_2$	5 to 7	

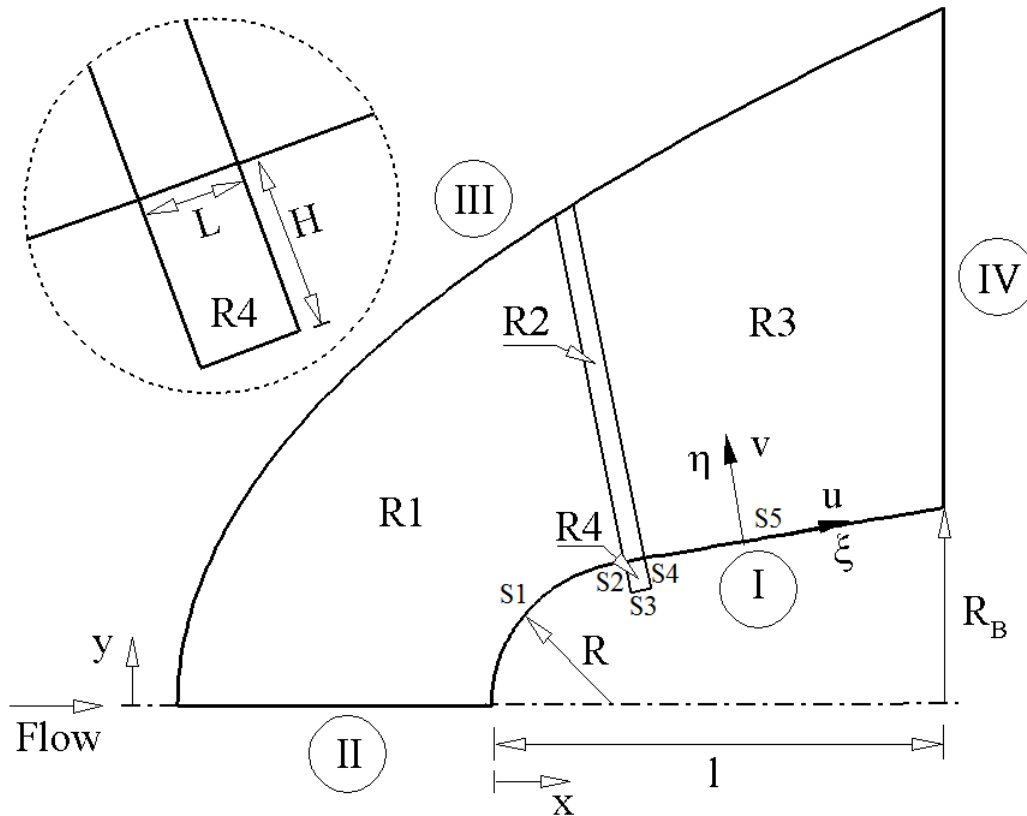


Figure 3.3 - Drawing illustrating a schematic view of the computational domain.

order to establish the collision rate. In the present investigation, it was defined two subcells/cell in each coordinate direction. As a result, the physical space network is used to facilitate the choice of simulated molecules for collisions as well as for the sampling of the macroscopic flow properties, such as temperature, pressure, density, etc.

In addition, time is advanced in discrete steps such that each step is small in comparison with the mean collision time. It should be remarked that each region has an appropriate value for the time step,  $\Delta t$ , and for the scaling factor,  $F_N$ , which relates the number of real molecules to the number of simulated molecules. The ratio of these two quantities,  $F_N$  and  $\Delta t$ , is the same in every region.

According to Fig. 3.3, side I is defined by the capsule surface. Diffuse reflection with complete surface accommodation is the condition applied to this side. Side II is a plane of symmetry, where all flow gradients normal to the plane are zero. At the molecular level, this plane is equivalent to a specular reflecting boundary. Side III is the freestream side through which simulated molecules enter and exit. Finally, the flow at the downstream outflow boundary, side IV, is predominantly supersonic and vacuum condition was assumed at this boundary (BIRD, 1994). As a result, simulated molecules can only exit at this boundary. It should be mentioned in this context that, close to the wall, molecules may not be moving at supersonic speed. Consequently, in this subsonic region close to the wall, there is an interaction between the flow and the downstream boundary. Nevertheless, the extent of the upstream effect of this boundary condition can be determined by changing the length of the cone surface. In doing so, it was found that the upstream disturbance is approximately of  $2\lambda_\infty$  for the altitudes investigated.

The mesh generation, the effect of the mesh resolution, and the verification and validation process employed in the present work are discussed in the next chapter.



## 4 CODE VERIFICATION AND VALIDATION

Before proceeding with the analysis of the computational results, it proves instructive to first examine the verification and validation processes. The processes of verification and validation in the DSMC code consist of four basic steps; (1) verification by increasing the number of computational cells, (2) verification by increasing the number of simulated particles, (3) verification by increasing the time step, and (4) validation by comparing with experimental data or numerical results available in the literature. In this fashion, the purpose of this Chapter is to discuss at length these four basic steps.

### 4.1 Computational Requirements

The DSMC method has become the most common computational technique for modeling complex transitional flows of engineering interest. The DSMC method models a gas flow by using a computer to track the trajectory of simulated molecules. Each simulated molecule represents a fixed number of real gas molecules. The simulated molecules are allowed to move and collide, while the computer store their position coordinates, velocities and energies. In order to do that, a computational mesh is used as a reference in the selection process of the collision pairs, and for sampling and averaging macroscopic flowfield properties. Currently, several methods of mesh generation have been used for different body shapes, each with its complexity and computational cost. For instance, the body fitted, coordinate system implemented by Abe (ABE, 1989), the transfinite interpolation method made by Olynick et al. (OLYNICK et al., 1989) and multi-level Cartesian mesh proposed by Rault (RAULT, 1994).

In general, three basic types define mesh schemes: (1) uniform cartesian mesh, (2) structured body-fitted mesh, and (3) unstructured body-fitted mesh. Each of these schemes has advantages and disadvantages such as a low cost during the movement of molecules, the use of cells with non-uniform size in regions where the gradients are more intense, and application in simulation of complex geometries. Wilmoth (WILMOTH et al., 1996) and Nance (NANCE et al., 1997) discuss in details the advantages of each scheme, in terms of accuracy, computational efficiency and ease of use.

Three primary constraints on the DSMC method must be considered when evaluating computational requirements: (1) the simulation time step must be less than the local average collision time, (2) the cell size must be smaller than the local mean free

path, and (3) the number of simulated molecules per cell must be roughly constant in order to preserve collision statistics.

An important assumption in the DSMC method is that the gas is dilute, meaning that the average molecular diameter is much smaller than the average spacing between molecules in the gas. This assumption allows that the molecular motion be decoupled from the molecular collisions over a small local time interval. Thus, the successful application of the method requires that the time step must be a fraction of the average time between collisions, as well as the cell dimensions must be of the order of one third of the local mean free path.

In order to accurately model the collisions through a statistical process, the cell size should be around one third of the local mean free path  $\lambda$ , becoming even smaller than  $\lambda$  in the directions in which the gradients are more intense (BIRD, 1994). In the vicinity of the body surface, the cell size in the normal direction to the surface should also be the order of or smaller than one third of the local mean free path. The reason for that is because in certain regions, such as the vicinity of adiabatic surfaces, flowfield gradients must be very small, and the cell size must be small enough to adequately capture flowfield physics near the body surface. Otherwise, the most energetic molecules so close to the far edge of the cell could transfer energy and momentum to molecules located immediately adjacent to the body surface. This leads to over prediction of heat flux to and the aerodynamic forces acting on the body surface. This type of error can be minimized by reducing the cell size relative to the local mean free path of simulated molecules near the surface. The cell size should be small in regions within the flowfield where the physical properties vary rapidly. For instance, in regions where the density is large, the cell size should be reduced in order to limit not only the number of simulated molecules in each cell but also the number of collisions in a given time step.

In order to adequately model the physics of interest, the number of simulated molecules in the computations must be greater than a certain number. To obtain accurate collision statistics, it is desirable to have 20 - 30 simulated molecules in each cell (FALLAVOLLITA et al., 1993; ALEXANDER et al., 2000). However, it is difficult to maintain this requirement when the density distribution in the computational domain is no longer uniform. As pointed out by Kannenberg and Boyd (KANNENBERG; BOYD, 2000), the number of simulated molecules in the cell varies inversely with the gas density. Therefore high-density regions will tend to have few simulated molecules, while low-density regions will have a large number of simulated molecules

resulting in over resolution in the flow domain. In order to overcome this difficulty, a variable scaling factor  $F_N$  is used to control the distribution of simulated molecules within the grid.  $F_N$  is the ratio of real molecules to simulated molecules.

In this scenario, the computational effort is substantially reduced by subdividing the flowfield into an arbitrary number of regions where the time step  $\Delta t$  and the scaling factor  $F_N$  remain constant within a region, but they can vary from one region to another. The combination of subdividing the flowfield into regions along with the use of variable cell sizes provides the flexibility to substantially reduce the total number of molecules used in the simulation and also resolves the flow gradients. It is important to mention that, although  $F_N$  and  $\Delta t$  can vary from region to region, the ratio  $F_N/\Delta t$  must be the same for all regions in order to conserve mass across region boundaries in the flow.

More details for estimating the computational requirements of DSMC simulations are presented at length by Rieffel ([RIEFFEL, 1999](#)).

## 4.2 Computational Mesh Generation

In order to generate the computational grid, the grid generation scheme, proposed by Bird ([BIRD, 1994](#)) in his G2 algorithm, was employed. Proceeding in a manner analogous to the Bird treatment, the physical domain is divided into a number of arbitrary four-sided regions, as shown in Fig. 3.3. For each region, two opposite sides may be either straight or curved (for instance, sides I and III in region 3 in Fig. 3.3) and the other two sides are straight (the two vertical lines in region 3 in Fig. 3.3). Along the boundaries, point distributions are generated in such way that the number of points on each opposite side is the same. In the following, the cell structure is defined by joining the corresponding points on each side by straight lines and then dividing each of these lines into segments which are joined to form the system of quadrilateral cells. The point distribution can be controlled by a number of different distribution functions which allow the concentration of points in areas where high flow gradients or small mean free paths are expected, for instance, close to the body surface, side I, shown in Fig. 3.3. In addition, the point distributions may be chosen independently for each region.

## 4.3 Computational Mesh Adaptation

In order to improve the solution accuracy and the grid efficiency, a mesh adaptation technique is also adopted in the present study. Initially, calculation is made on a

coarse mesh until a converged solution is obtained. Afterwards, the value of adaptation indicators is examined for each cell based on the flow properties, such as the ratio of the mean free path to the cell size, the ratio of the time step to the time related to the collision frequency. The main steps for the mesh adaptation employed in this study are summarized as follows: (1) an initial region and cell mesh structure are generated from consideration of the freestream conditions, (2) assumed values of  $F_N$  are chosen for each region,  $\Delta t$  are then estimated subject to the condition that the ratio  $F_N/\Delta t$  be the same for all regions, (3) these parameters are iteratively modified until an acceptable number of simulated molecules, cell size distribution, and simulation time step are obtained.

#### 4.4 DSMC Test Case

The problem of a hypersonic flow past a flat-ended circular cylinder was selected as a test case in order to elucidate the requirements posed on the verification and validation processes related to the axisymmetric version of the DSMC code. The flat-ended circular cylinder model has been selected because numerical simulations (PULLIN et al., 1977) are available in the open literature for comparison. Therefore, code verification and validation efforts were performed based in a code-to-code comparison. In pursuit of this goal, the axisymmetric DSMC code employed was adapted in order to reproduce the numerical DSMC data given by Pullin et al. (PULLIN et al., 1977).

In the computational solution, it was assumed that the flat-ended circular cylinder is immersed in a uniform stream flowing parallel to the cylinder itself. The cylinder is modeled with a frontal-face radius  $R$  of 0.0185 m, which corresponds to a  $6\lambda_\infty$ , and a total length  $L$  of  $30\lambda_\infty$ , where  $\lambda_\infty$  stands for the freestream mean free path, defined subsequently. Figure 4.1 displays a schematic view of the model employed and the flow direction. Since the wake region behind the flat-ended cylinder is not of interest in this investigation, it was assumed that the flat-ended cylinder is infinitely long but only a length  $L$  is considered. Moreover, Pullin et al. (PULLIN et al., 1977) adopted on its simulation the inverse power law collision model where the internal energy exchanges were based on the Larsen-Borgnakke statistical model, described in chapter 2.

The freestream flow conditions used in the present numerical simulation of the flow past the flat-ended circular cylinder are those given by Pullin et al. (PULLIN et al., 1977), summarized in Tab. 4.1. The gas properties are those given by Bird (BIRD, 1994), and are shown in Tab. 4.2.

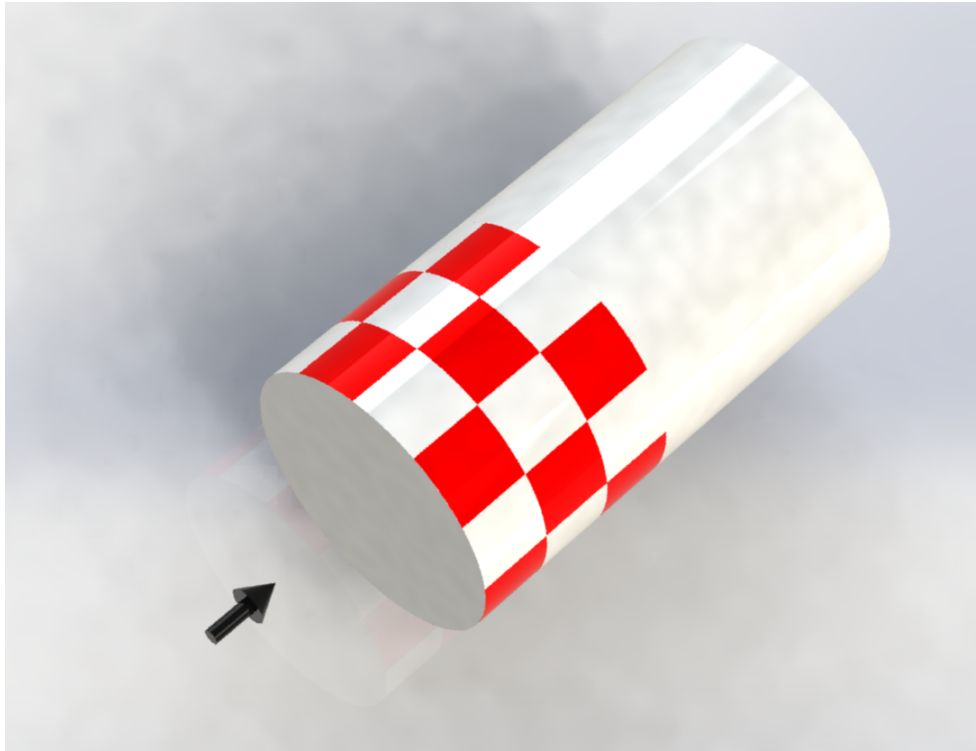


Figure 4.1 - Drawing illustrating the flat-ended circular cylinder.

Table 4.1 - Freestream flow conditions.

Properties	Values	Unit
Altitude	80	<i>km</i>
Velocity ( $U_\infty$ )	2694	<i>m/s</i>
Temperature ( $T_\infty$ )	180.7	<i>K</i>
Pressure ( $p_\infty$ )	1.0366	<i>N/m<sup>2</sup></i>
Density ( $\rho_\infty$ )	$1.999 \times 10^{-5}$	<i>kg/m<sup>3</sup></i>
Number density ( $n_\infty$ )	$4.1562 \times 10^{20}$	<i>m<sup>-3</sup></i>
Mean free path ( $\lambda_\infty$ )	$3.085 \times 10^{-3}$	<i>m</i>

Table 4.2 - Gas properties.

$\chi$	$m(kg)$	$d(m)$	$\omega$	
$N_2$	1.0	$4.650 \times 10^{-26}$	$4.17 \times 10^{-10}$	0.74

According to Tabs. 4.1 and 4.2,  $T_\infty$ ,  $p_\infty$ ,  $\rho_\infty$ ,  $n_\infty$ ,  $\lambda_\infty$  and  $U_\infty$  stand, respectively, for freestream temperature, pressure, density, number density, molecular mean free path, and velocity, also  $\chi$ ,  $m$ ,  $d$  and  $\omega$  stand, respectively, for mass fraction, molecular mass, molecular diameter and viscosity index.

The freestream velocity  $U_\infty$  is assumed to be constant at 2694 m/s, which corresponds to a freestream Mach number  $M_\infty$  of 10. The wall temperature  $T_w$  is assumed constant at 570 K. This temperature is chosen in order to correspond the temperature ratio  $T_w/T_\infty$  of 3.15 assumed by Pullin et al. (PULLIN et al., 1977).

Finally, by considering the diameter  $D$  of the cylinder as the characteristic dimension of the flowfield, then the overall Knudsen number  $Kn_D$  corresponds to 0.167, and the Reynolds number  $Re_D$  corresponds to 90.7, based on the conditions in the undisturbed stream.

For the numerical treatment of the problem, the flowfield around the flat-ended cylinder is divided into two regions, which are subdivided into computational cells. The cells are further subdivided into subcells, two subcells/cell in each coordinate direction. As mentioned earlier, the cell provides a convenient reference for the sampling of the macroscopic gas properties, while the collision partners are selected from the same subcell for the establishment of the collision rate. Therefore, the physical space network is used to facilitate the choice of simulated molecules for collisions and for the sampling of the macroscopic flow properties such as temperature, pressure, density, etc.

The computational domain used for the calculation is made large enough so that body disturbances do not reach the upstream and side boundaries, where freestream conditions are specified. The computational domain lies  $18\lambda_\infty$  ahead of the frontal face and extends radially up to  $28\lambda_\infty$  from the cylinder surface. A schematic view of the computational domain is depicted in Fig. 4.2. Advantage of the flow symmetry is taken into account, and molecular simulation is applied to one-half of a full configuration. Based on this figure, side I is defined by the body surface. Diffuse reflection with complete thermal accommodation is the condition applied to this side. Side II is a plane of symmetry, where all flow gradients normal to the plane are zero. At the molecular level, this plane is equivalent to a specular reflecting boundary. Side III is the freestream side through which simulated molecules enter and exit. Finally, the flow at the downstream outflow boundary, side IV, is predominantly supersonic and vacuum condition is specified (BIRD, 1994; GUO; LIAW, 2001). At this boundary, simulated molecules can only exit.

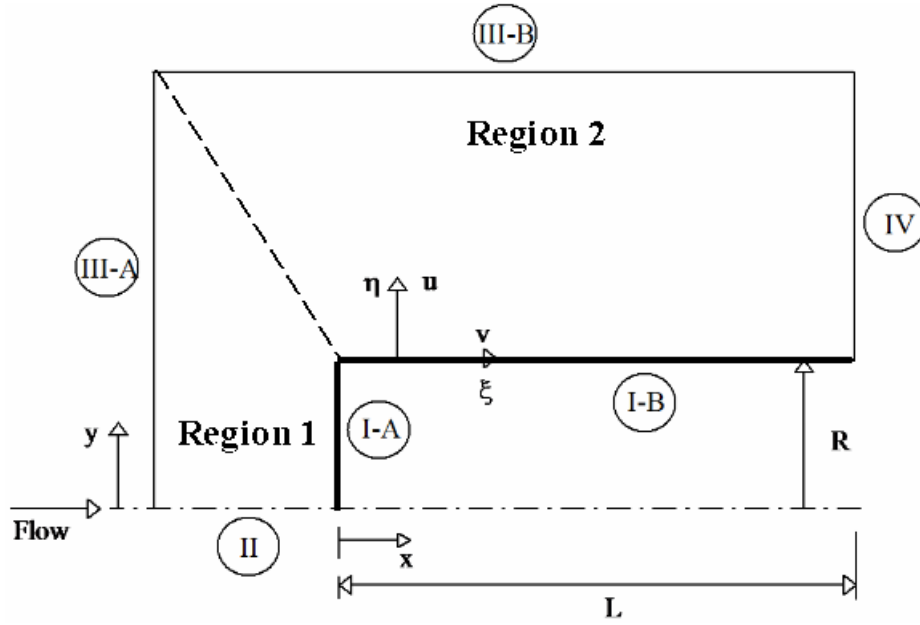


Figure 4.2 - Computational domain for the flat-ended cylinder model.

Still referring to Fig. 4.2, region 1 consisted of 40 cells along side I-A ( $\xi$ -direction) and 60 cells along side II ( $\eta$ -direction). Region 2 consisted of 70 cells distributed along side I-B ( $\xi$ -direction) and 60 cells along side IV ( $\eta$ -direction). This computational mesh was defined as being the standard case. In addition to this mesh, two other meshes, defined by coarse and fine, were used to study the sensitivity of the computations to the mesh resolution.

#### 4.5 Effect of Mesh Resolution

The effect of mesh resolution on computational results is of particular interest for the present study since insufficient grid resolution can reduce significantly the accuracy of predicted aerodynamic heating and forces. Hence, heat transfer, pressure and skin friction coefficients are used as the representative parameters for the grid sensitivity study. The effect of altering the mesh resolution in the  $\xi$ - and  $\eta$ -direction was investigated for a coarse and fine mesh with, respectively, 50% less and 50% more cells with respect to the standard mesh. Furthermore, each mesh was made up of non-uniform cell spacing in both directions.

The effect of changing the number of cells in the  $\xi$ -direction on pressure  $C_p$ , skin friction  $C_f$  and heat transfer  $C_h$  coefficients is illustrated in Fig. 4.3. In this set of plots, the dimensionless length  $s/R$  corresponds to the arc length  $s$  normalized by

Table 4.3 - Number of cells in the ( $\xi$ -direction) and [ $\eta$ -direction] for the flat-ended cylinder model.

	Region 1	Region 2	Total number of cells
<i>Coarse</i>	(20)[60]	(35)[60]	3300
	(40)[30]	(70)[60]	5400
<i>Standard</i>	(40)[60]	(70)[60]	6600
	(60)[60]	(105)[60]	9900
<i>Fine</i>	(40)[90]	(70)[90]	9900

the flat-ended cylinder radius. Based on this set of plots, it is clearly seen that the calculated results are not affected by the range of cell spacing considered for the  $\xi$ -direction in the cases defined by coarse, standard and fine meshes. Also the effect of cell variations on the flowfield properties (not shown) was negligible.

A similar examination was made in the  $\eta$ -direction. The sensitivity of the calculated results to cell size variations in the  $\eta$ -direction is displayed in Fig. 4.4. In this group of plots, a new series of three simulations, with grids with 110 cells in the  $\xi$ -direction and 30, 60 and 90 cells in the  $\eta$ -direction, are compared. The cell spacing in both directions is again nonuniform. According to these plots, the results for three independent meshes are approximately the same, indicating that the standard mesh is essentially grid independent. For the standard case, the cell size in the  $\eta$ -direction is always less than the local mean free path length in the vicinity of the surface.

#### 4.6 Effect of Number of Molecules Variations

A similar examination was made for the number of molecules. The sensitivity of the calculated results to number of simulated molecules variations is demonstrated in Fig. 4.5. The standard grid corresponds to a total of 138100 molecules. Two new cases using the same grid were investigated. These new cases correspond to, on average, 69100 and 207300 molecules in the entire computational domain. The number of simulated molecules was increased by changing the scaling factor  $F_N$  defined earlier. It is seen that the results are the same for all of the cases, indicating that the standard grid with a total of 138100 molecules is enough for the computation of the flowfield properties. For completeness, Fig. 4.6 illustrates the standard grid used in this simulation.

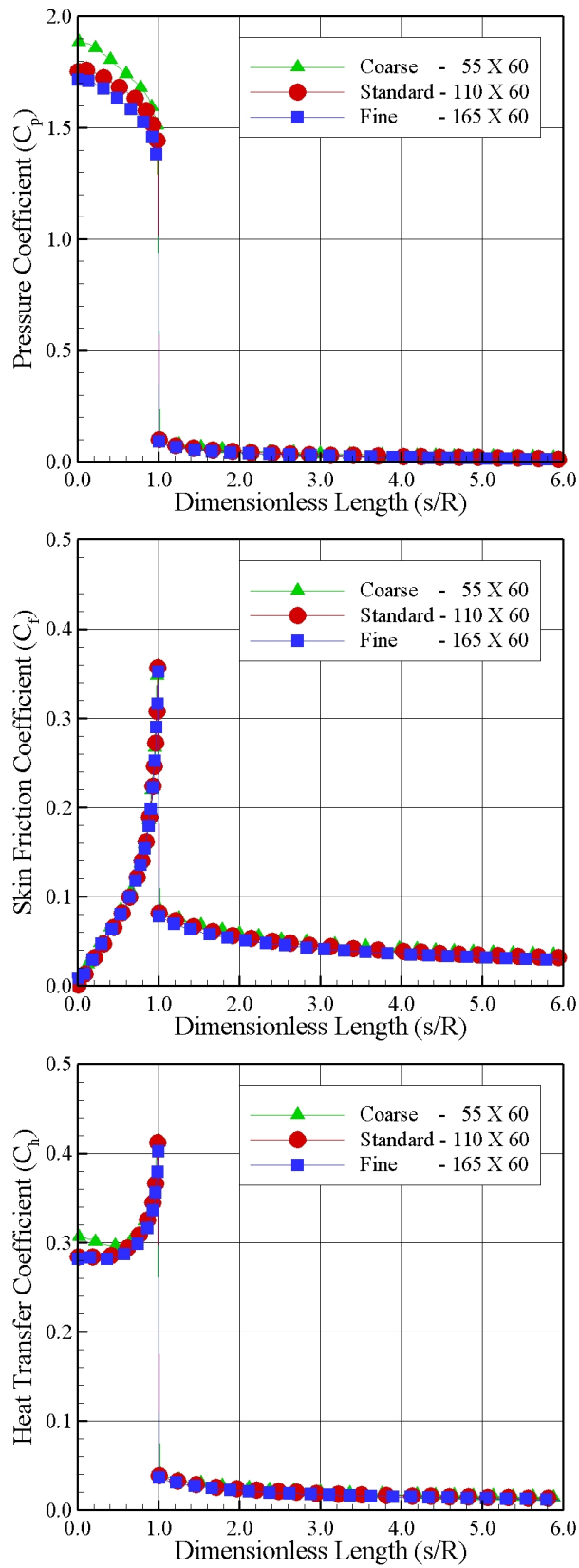


Figure 4.3 - Effect of variation in the cell size in the  $\xi$ -direction coordinate on pressure (top), skin friction (middle) and heat transfer (bottom) coefficients.

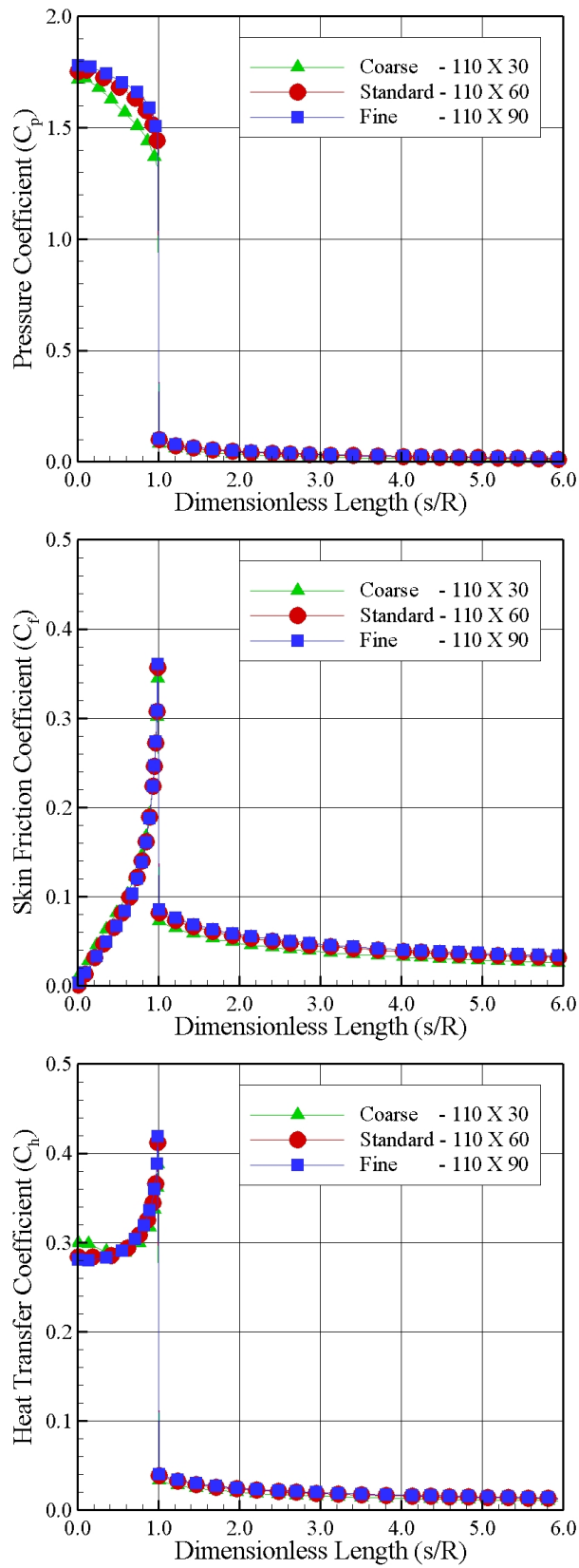


Figure 4.4 - Effect of variation in the cell size in the  $\eta$ -direction coordinate on pressure (top), skin friction (middle) and heat transfer (bottom) coefficients.

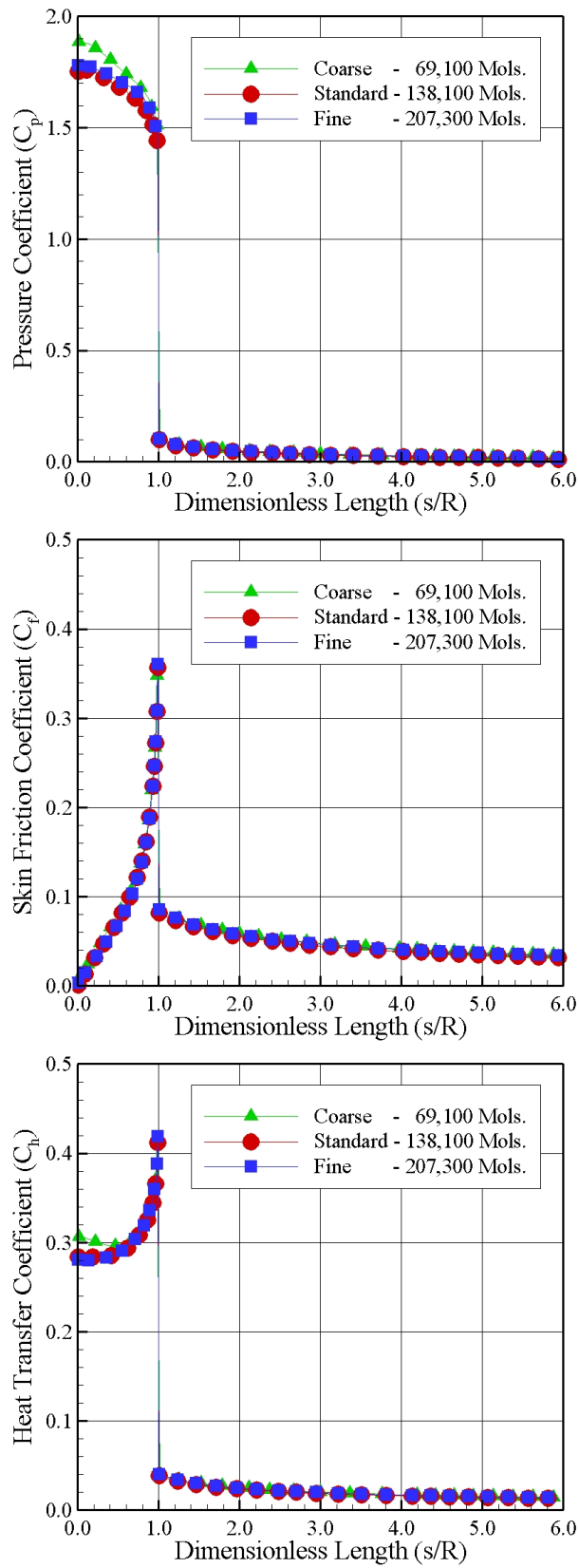


Figure 4.5 - Effect of variation in the number of molecules on pressure (top), skin friction (middle) and heat transfer (bottom) coefficients.

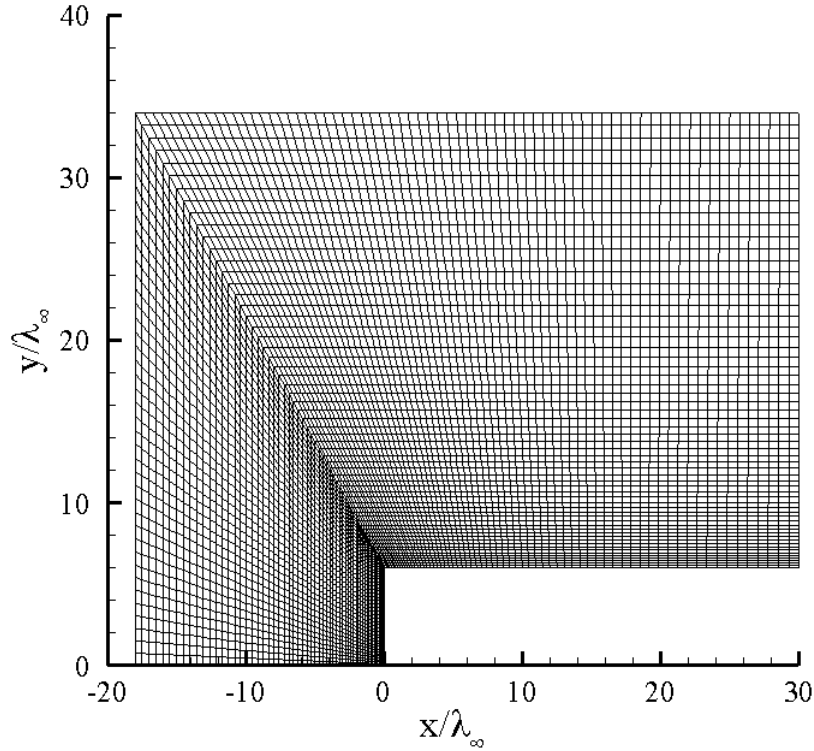


Figure 4.6 - Drawing illustrating the standard grid.

#### 4.7 Numerical Comparisons

Verification of the overall computational model was performed via flowfield property comparisons. In this scenario, the primary flow properties – velocity, density, translational and rotational temperatures – are compared to numerical simulation data (PULLIN et al., 1977) in order to ascertain how well the DSMC algorithm employed in this study is able to predict hypersonic rarefied flows. Since these data have been published elsewhere, details will be kept to a minimum and the discussion restricted to the significant conclusions.

Normal velocity profile along the stagnation streamline is illustrated in Fig. 4.7. In this plot the normal velocity  $u$  is normalized by the freestream velocity  $U_\infty$ , and the distance  $x$  upstream the cylinder is normalized by the frontal-face radius  $R$ . Also, the square symbol represents the present DSMC simulations, and the circle symbol represents numerical data obtained by Pullin et al. (PULLIN et al., 1977). It is immediately evident from Fig. 4.7 that there is a close overall agreement between the present DSMC simulation and the calculated data given by Pullin et al. (PULLIN et al., 1977) at the vicinity of the stagnation region. However, far from the stagnation region, a slight disagreement is observed between the numerical data and those given

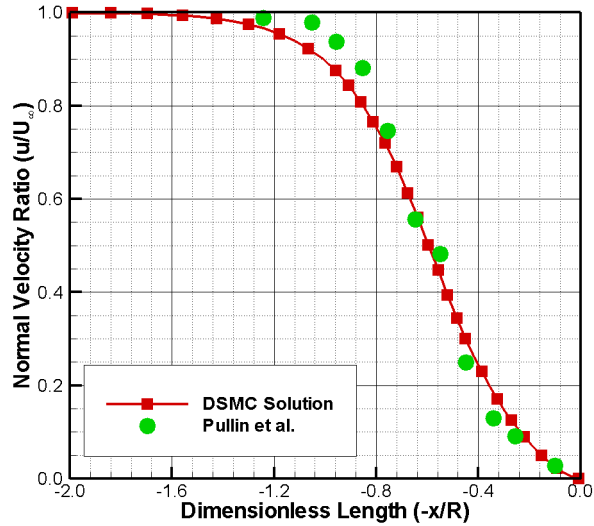


Figure 4.7 - Normal velocity profile along the stagnation line.

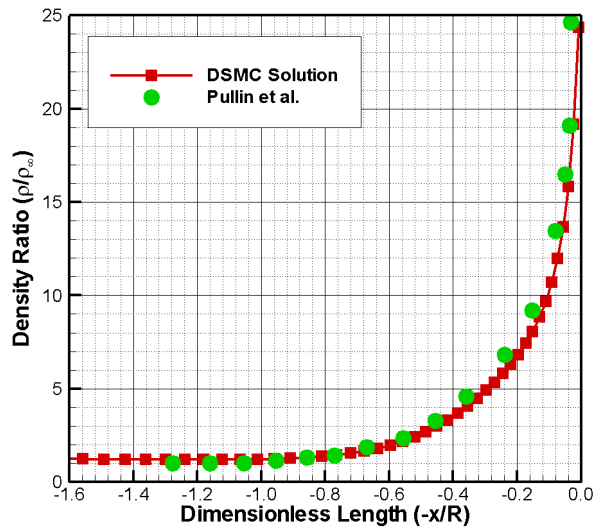


Figure 4.8 - Density ratio profile along the stagnation line.

by the present investigation. It is seen that the disturbance due to the presence of the cylinder is felt more upstream in the velocity profile for the present solution.

Similar to the normal velocity profile, the density ratio  $\rho/\rho_\infty$  profile along the stagnation line is displayed in Fig. 4.8. Again it is clearly seen that the density ratio profile in the present account agrees with that obtained by Pullin et al. (PULLIN et al., 1977) at the vicinity of the stagnation point.

In analogous fashion, variations in kinetic temperature profiles along the stagnation streamline are displayed in Figs. 4.9 and 4.10 for translational and rotational tem-

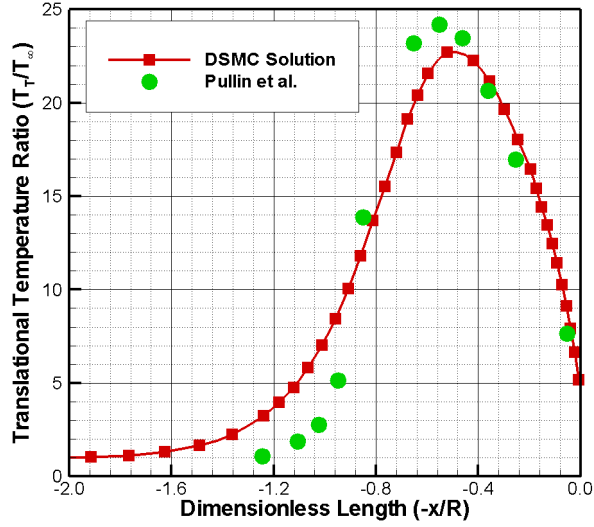


Figure 4.9 - Dimensionless translational temperature ratio profile along the stagnation line.

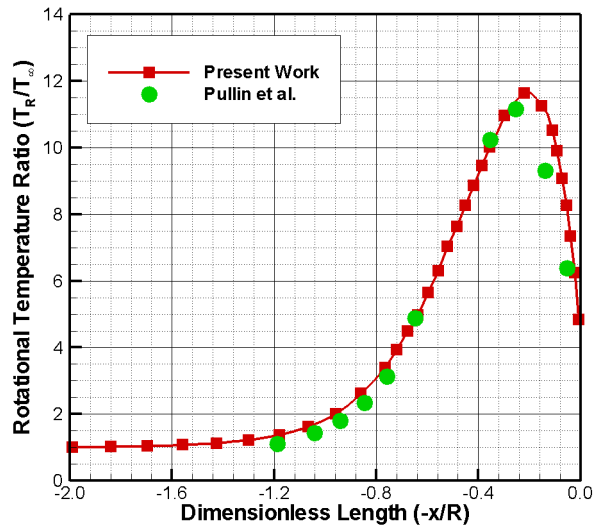


Figure 4.10 - Dimensionless rotational temperature ratio profile along the stagnation line.

peratures, respectively. In this set of plots, translational and rotational temperatures are normalized by the freestream temperature  $T_\infty$ . It is apparent from these figures that thermodynamic non-equilibrium occurs throughout the shock layer, as shown by the lack of equilibrium of the translational and rotational temperatures. Thermal non-equilibrium occurs when the temperatures associated with the translational and rotational modes of a polyatomic gas are different. According to this set of figures, a good agreement is observed on both simulations.

## 5 COMPUTATIONAL RESULTS AND DISCUSSION

Having computed flowfield properties over a wide range of simulation parameters, it proves instructive to summarize the major features of the results. In this fashion, the purpose of this chapter is to discuss and to compare differences in the flowfield properties as well as in the aerodynamic surface properties due to variations on the vehicle altitude, on the nose radius, and on the gap  $L/H$  ratio.

Before proceeding with the analysis, for convenience and late reference, it is desirable to set down the nomenclature employed in this chapter. A100, A90, and A80 stand for altitudes of 100, 90 and 80 *km*, respectively. R1.00, R0.50, and R0.25 correspond to the nose radius of 267.80, 133.90, and 66.95 mm, respectively, investigated in this research, as defined in Table 3.1. In the following, G1.00, G0.50, and G0.25 represent the gap  $L/H$  ratio of 1, 1/2, and 1/4, respectively. The special case of a capsule surface without a gap (SANTOS, 2012) is represented by G0.00.

### 5.1 Flowfield Properties

This section focuses on the calculations of the primary properties obtained from the DSMC results. The primary properties of particular interest in this dissertation are velocity, density, pressure and kinetic temperatures.

#### 5.1.1 Velocity Field

In the DSMC method, the macroscopic properties are computed as averages from the microscopic properties in each cell in the computational domain. As a result, the velocity vector is given by the following expression,

$$\vec{c}_0 = \frac{\sum_{j=1}^N m_j \vec{c}_j}{\sum_{j=1}^N m_j} \quad (5.1)$$

where  $N$ ,  $m$  and  $\vec{c}_j$  represent, respectively, the number of molecules, mass, and the velocity vector of the molecules in each cell.

It is important to mention that the mean molecular velocity  $\vec{c}_j \equiv \vec{c}_0 = u \vec{i} + v \vec{j} + w \vec{k}$  defines the macroscopic mean velocity. In addition, the velocity of the molecules relative to the macroscopic mean velocity, defined by thermal or peculiar velocity, is denoted by  $\vec{c} \equiv \vec{c} - \vec{c}_0$ .

Tangential velocity ratio for three sections along the capsule surface and their de-

pendence on gap  $L/H$  ratio are illustrated in Fig. 5.1 for altitudes of 100 and 80 km. In this set of plots, the tangential velocity  $u$  is normalized by the freestream velocity  $U_\infty$ , the arc length  $s$  along the capsule surface is normalized by the nose radius  $R$ , and the height  $\eta$  in the off-body direction ( $\eta$ -direction in Fig. 3.3) is also normalized by the nose radius  $R$ . In addition, filled and empty symbols correspond to the tangential velocity ratio for altitude of 100 and 80 km, respectively. Results for altitude of 90 km are intermediate and they are not shown. For comparison purpose, the tangential velocity ratio for the capsule surface without a gap are presented in the same plots as a solid line for both altitudes. Furthermore, in an effort to emphasize points of interest, three sections along the body surface, defined by  $s/R$  of 0.7, 1.3, and 1.50, correspond, respectively, to sections located on the spherical nose, immediately upstream and downstream the gap position on the afterbody surface.

Interesting features can be drawn from this set of tangential velocity ratio. As the dimensionless arc length  $s/R$  increases, i.e., as the body slope decreases, the tangential velocity adjacent to the body surface increases. This is to be expected since the flow experiences an expansion as it moves downstream along the capsule surface. It should be noted that the tangential velocity  $u \rightarrow u_\infty$  as  $\eta \rightarrow \infty$ . Therefore, because of the body curvature,  $u_\infty$  varies as a function of the body slope,  $u_\infty \rightarrow U_\infty \cos\theta$ , where  $\theta$  is the surface slope angle, changing from 90 degrees at the stagnation point to 11.4 degrees at the conical afterbody. In addition, it is important to note that  $U_\infty$  is slightly different for each altitude (see Tabs. 3.2, 3.3 and 3.4) and, therefore, the comparison is made in terms of ratio.

Still referring to this set of plots, it is clearly noticed that the tangential velocity ratio is not affected by the gap  $L/H$  ratio investigated in this work, since the tangential velocity ratio for the capsule with a gap in the surface are similar to those for the capsule without a gap in the surface with the same nose radius  $R$ . Therefore, by visual inspection, it is seen that no upstream or downstream disturb is caused by the presence of the gap, for the conditions investigated. Furthermore, it is also noticed that the flow decelerates faster along the surface with decreasing altitude. By decreasing the altitude, the freestream mean free path decreases. As a result, the density increases adjacent to the capsule surface, as shown in subsequent sections.

Another interesting characteristic in these plots is the similarity of the velocity ratio along the body surface. This is an indication that the velocity ratio may be expressed in terms of functions that, in appropriate coordinates, may be independent of one of the coordinate directions. However, no attempts have been made to find such

functions.

Tangential velocity ratio for three sections inside the gaps are shown in Fig. 5.2 parameterized by the gap  $L/H$  ratio. In this group of plots, left- and right column plots correspond, respectively, to the tangential velocity ratio for 100 km and 80 km of altitude. Again, results for altitude of 90 km are intermediate and they are not shown. In addition,  $\xi_L$  represents the distance inside the gap normalized by the gap length  $L$ . Therefore,  $\xi_L$  of 0.25, 0.50 and 0.75 mean that the profiles correspond to the station located in the fourth, half and three-quarter of the gap length.

According to this set of plots, it is noticed that, at the bottom of the gap,  $\eta_H = -1.0$ , the velocity ratio  $u/U_\infty$  is negative for the cases investigated. Approaching the top of the gap, the velocity ratio becomes positive at a section  $\eta_H$  that depends on the gap  $L/H$  ratio and on the altitude. At the top of the gap, at section  $\eta_H = 0.0$ , the velocity ratio is positive, and decreases with decreasing the gap  $L/H$  ratio and increases with increasing  $\xi_L$  from 0.25 to 0.75. As a result, the thickness of the separated boundary layer decreases with increasing the  $L/H$  ratio and slightly increases from section  $\xi_L = 0.25$  to  $\xi_L = 0.75$ .

Normal velocity ratio profiles inside the gaps are displayed in Fig. 5.3 for three sections as a function of the streamwise distance  $\xi_L$  and parameterized by the gap  $L/H$  ratio. In this set of diagrams, the normal velocity  $v$  is normalized by the freestream velocity  $U_\infty$ , and the three sections correspond to the transversal sections defined by the dimensionless height  $\eta_H$  of -0.25, -0.50, and -0.75. Based on these plots, it is observed that, near the gap backward face,  $\xi_L < 0.5$ , the normal velocity ratio profiles present positive values, meaning that the flow is moving upward. Conversely, at the vicinity of the gap forward face,  $\xi_L > 0.5$ , the normal velocity ratio profiles present negative values, indicating that the flow is moving downward. Therefore, based on the two opposite behaviors for the normal velocity ratio, it may be inferred that there is a region of a clockwise circulating flow. This behavior is observed for the three altitudes and nose radius investigated.

At this point, it is worth taking a closer look at the recirculation region. In this manner, streamline traces inside the gaps are depicted in Fig. 5.4, 5.5, and 5.6 for nose radius of  $R$ ,  $R/2$  and  $R/4$ , respectively. In this set of plots, left- and right-column plots correspond to altitudes of 100 km and 80 km, respectively. Based on these plots, it is clearly noticed that the flow within the gaps is characterized by a primary vortex system. In addition, the recirculation region fills the entire gaps. Furthermore, for 100 km of altitude, the vortex core is located at the top-most por-

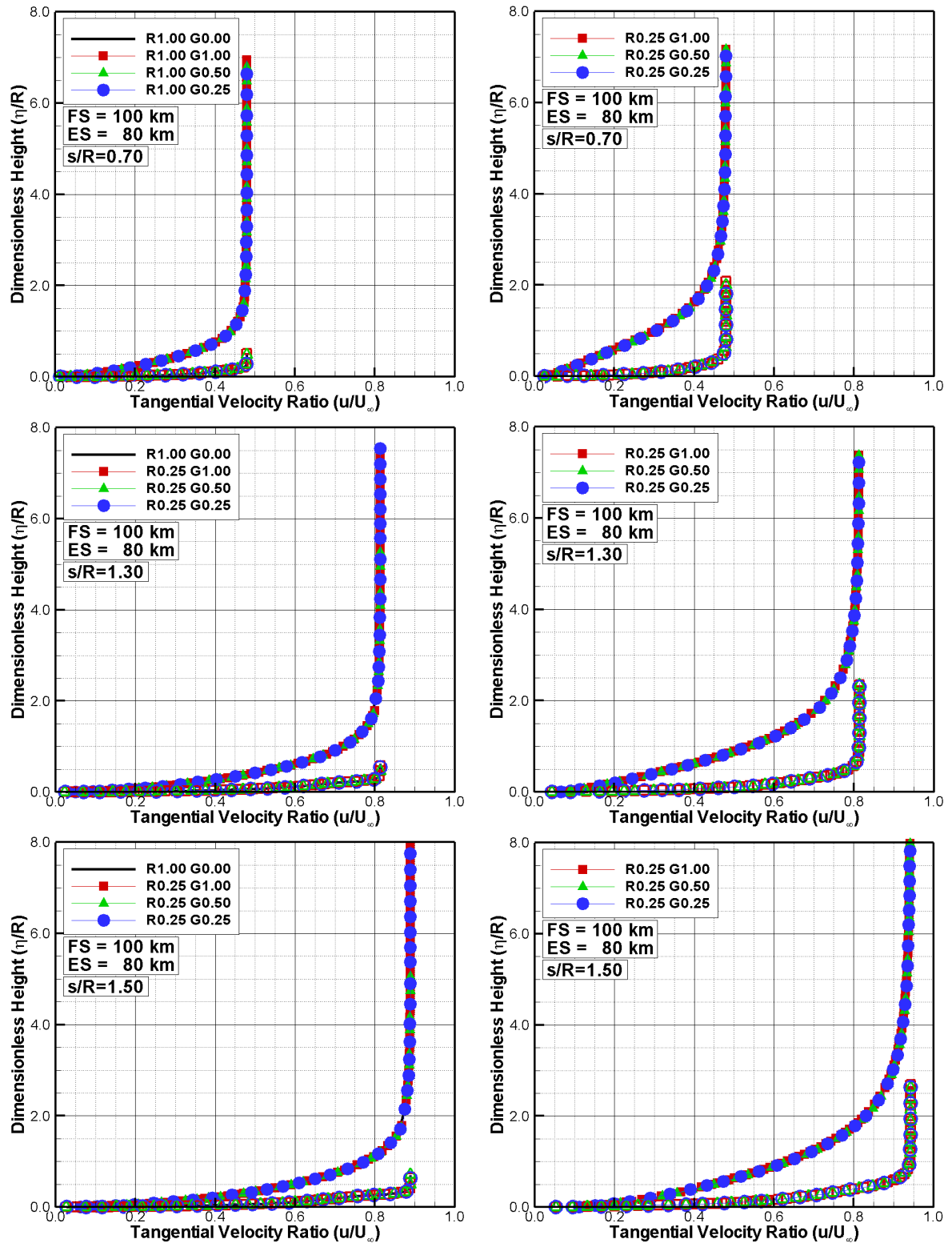


Figure 5.1 - Tangential velocity ratio ( $u/U_\infty$ ) for three sections  $s/R$  along the capsule surface and altitudes of 100 and 80 km, parameterized by the gap  $L/H$  ratio and nose radius  $R$ .

tion of the gaps. Conversely, for 80 *km* of altitude, the vortex core moves to the bottom-most portion of the gaps with decreasing the gap  $L/H$  ratio. Moreover, it should be mentioned that the gap flow topology observed here in a rarefied environment differs from that usually observed in the continuum flow regime, as mentioned in Chapter 1.

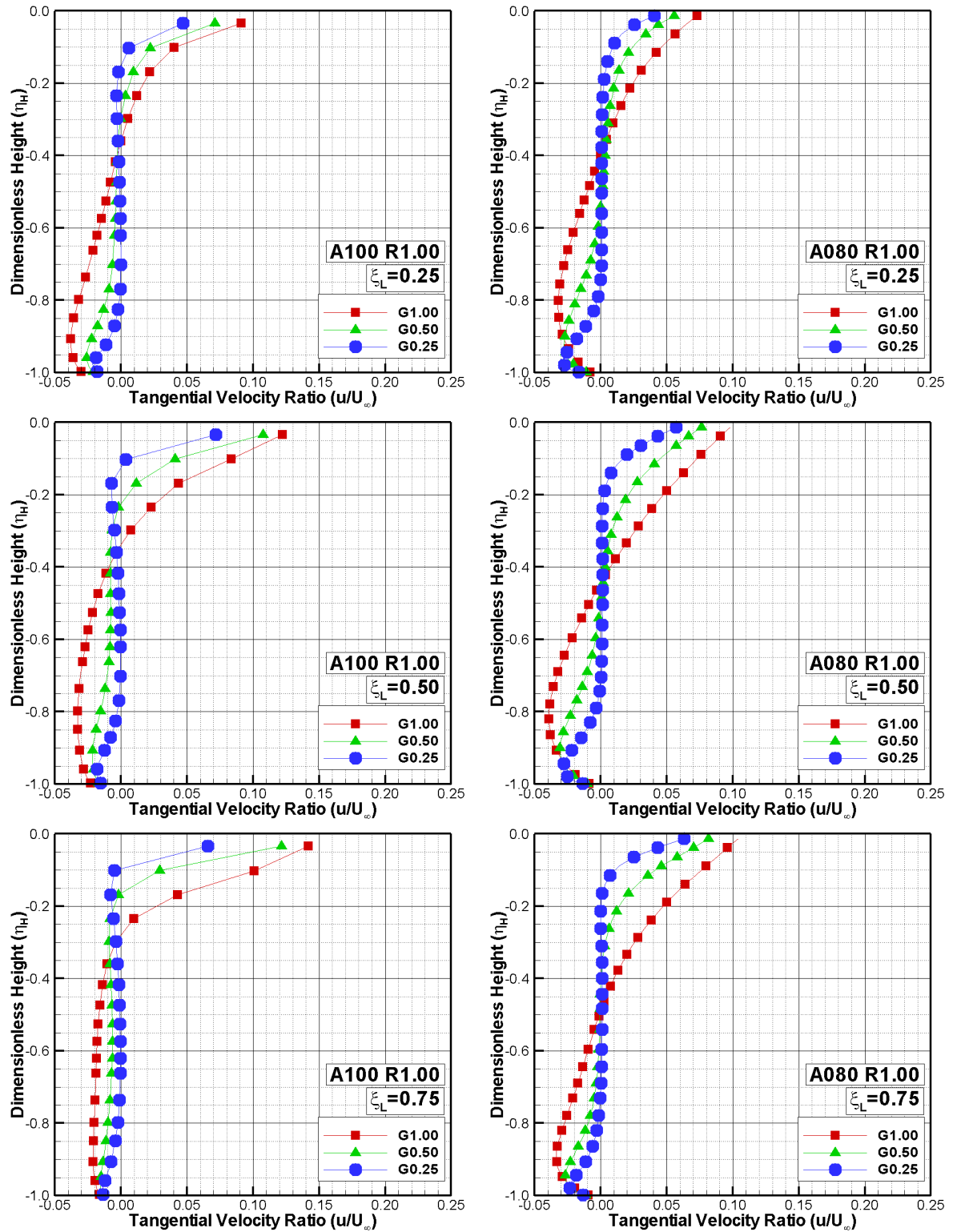


Figure 5.2 - Tangential velocity ratio ( $u/U_\infty$ ) for three vertical sections inside the gap for altitude of 100 km (left) and 80 km (right), nose radius  $R$ , and gap  $L/H$  of 1, 1/2 and 1/4.

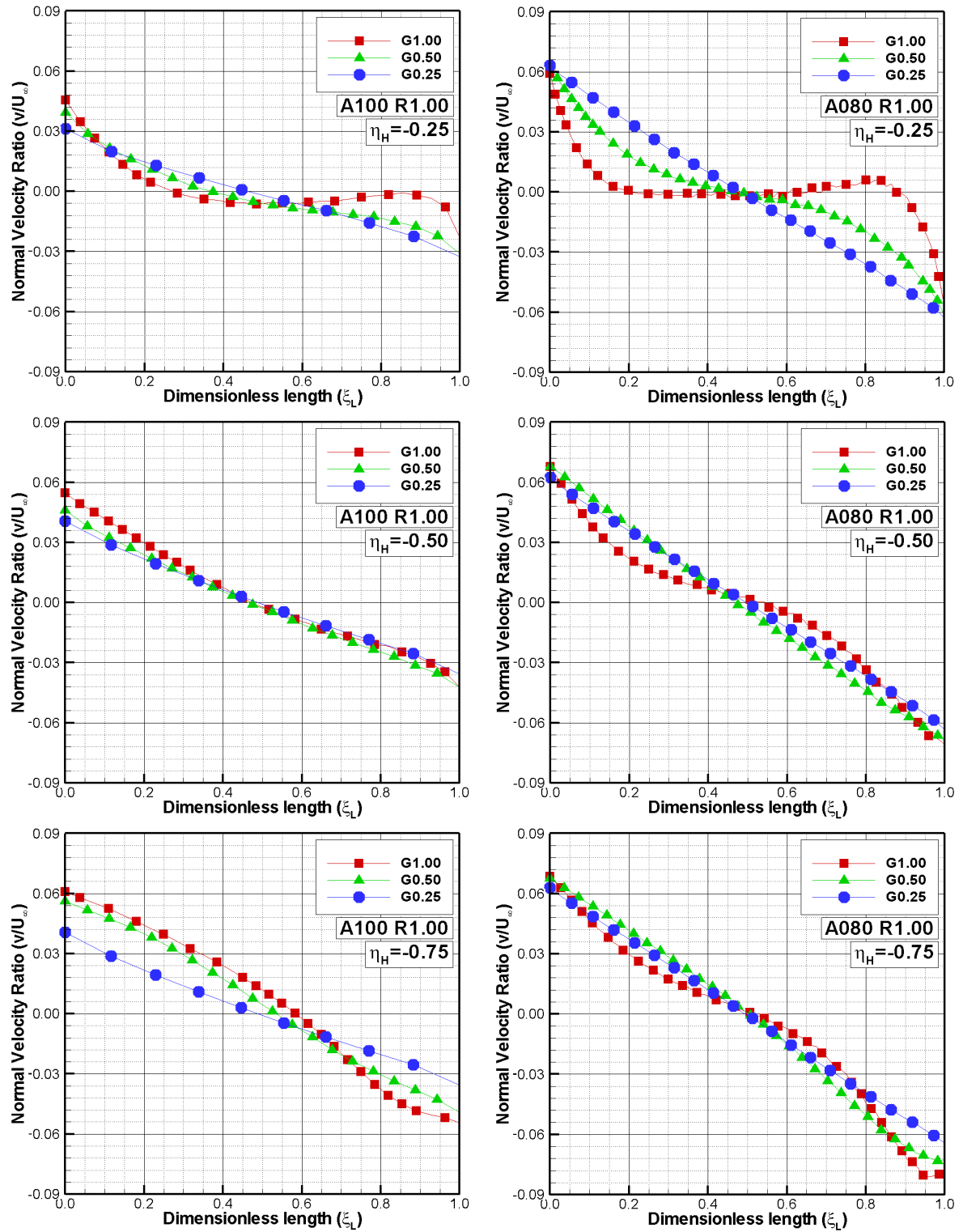


Figure 5.3 - Normal velocity ratio ( $v/U_\infty$ ) for three transversal sections inside the gap for altitude of 100 km (left) and 80 km (right), nose radius  $R$ , and gap  $L/H$  of 1, 1/2 and 1/4.

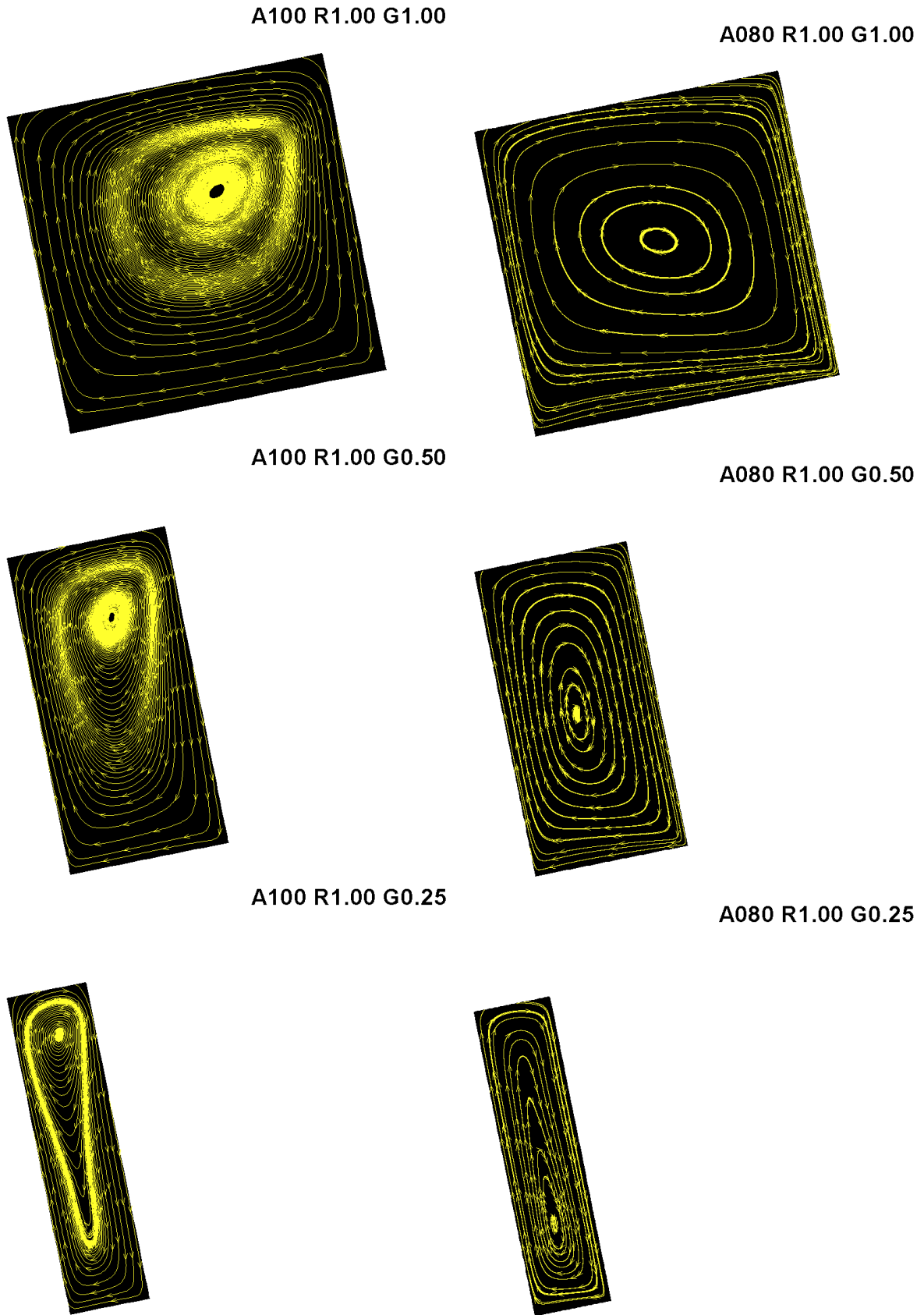


Figure 5.4 - Streamlines traces inside the gap for altitude of 100 km (left) and 80 km (right), nose radius  $R$ , and gap  $L/H$  of 1, 1/2, and 1/4.

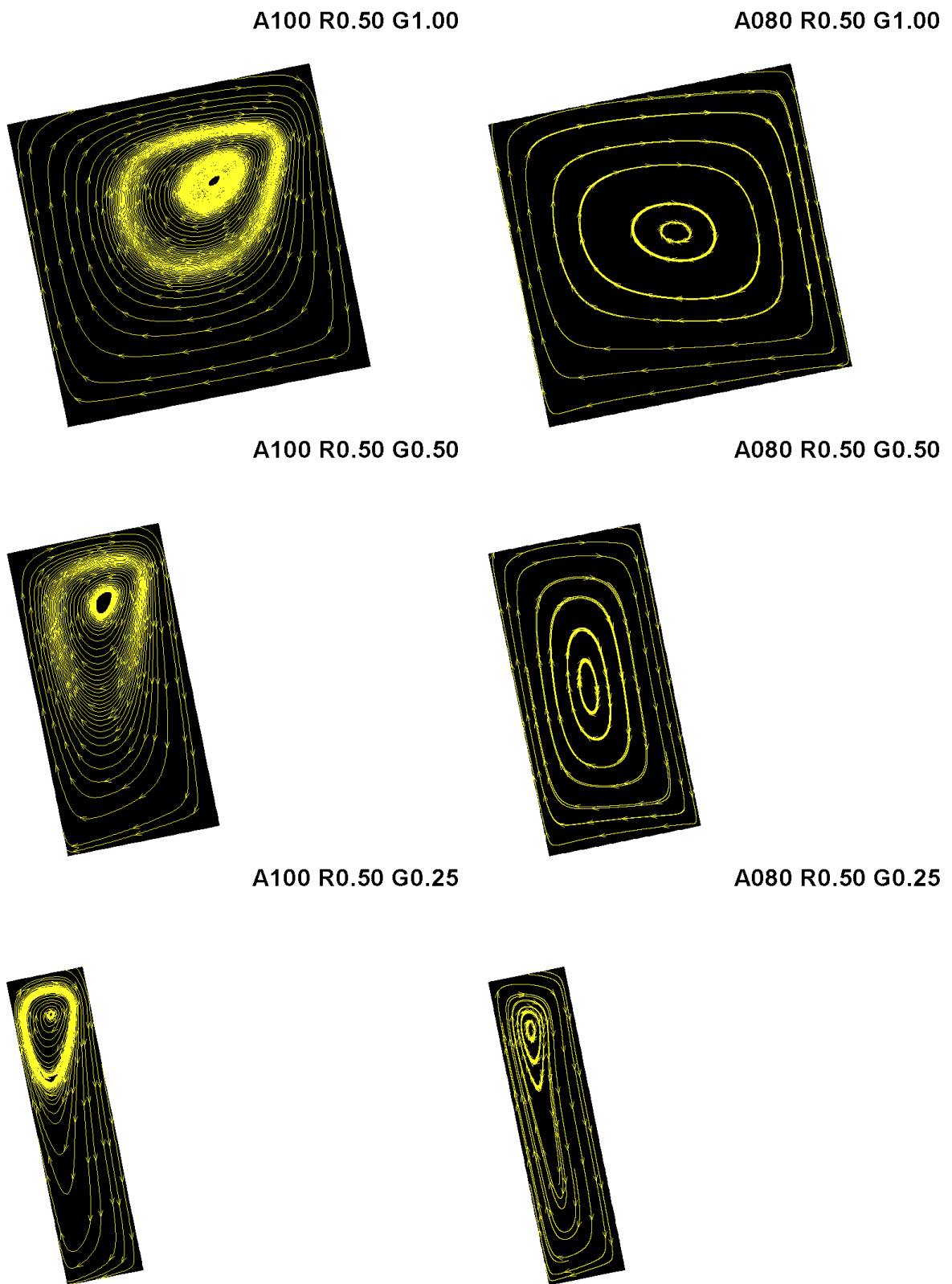


Figure 5.5 - Streamlines traces inside the gap for altitude of 100 km (left) and 80 km (right), nose radius  $R/2$ , and gap  $L/H$  of 1, 1/2, and 1/4.

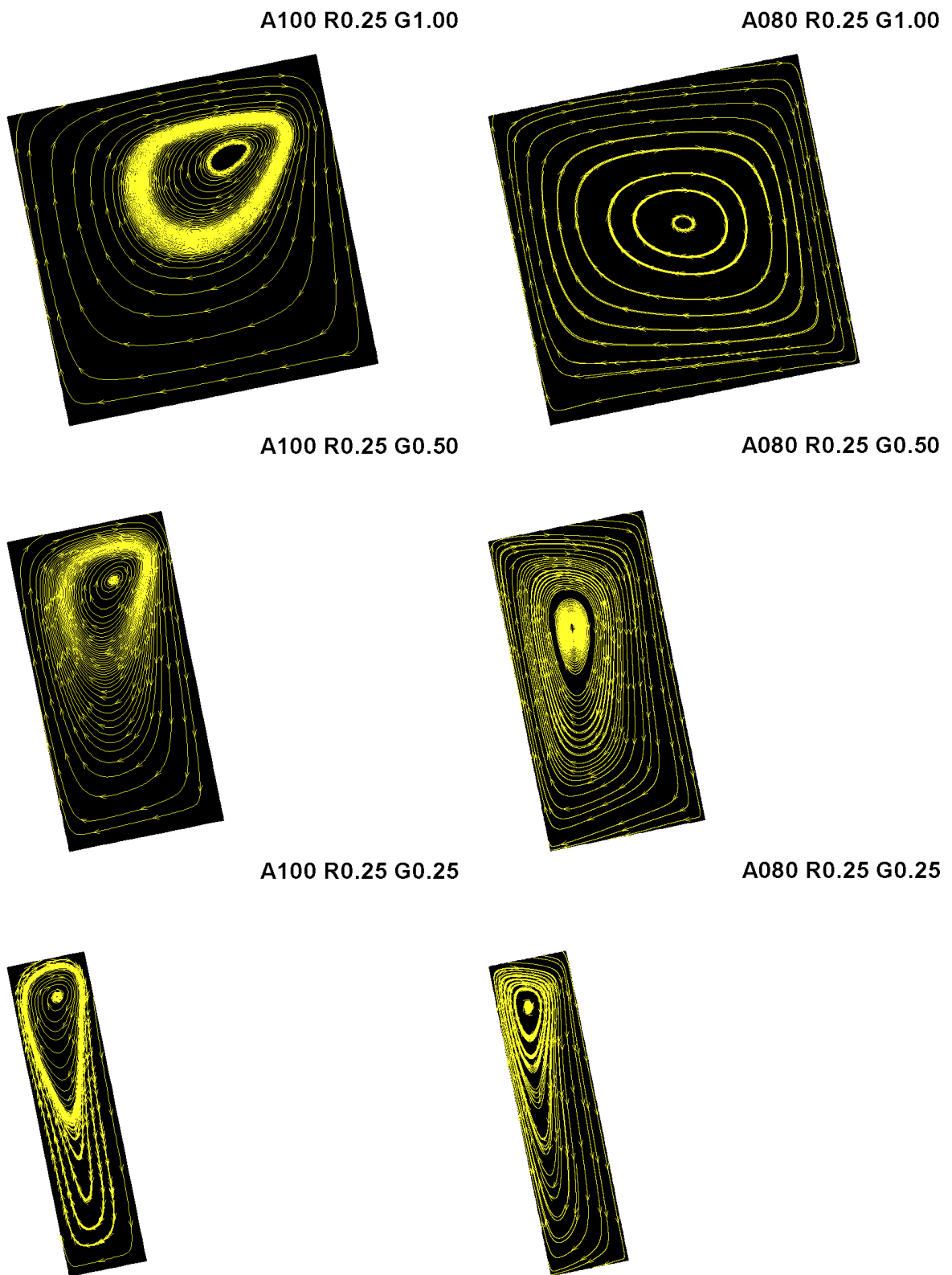


Figure 5.6 - Streamlines traces inside the gap for altitude of 100 km (left) and 80 km (right), nose radius  $R/4$ , and gap  $L/H$  of 1, 1/2, and 1/4.

### 5.1.2 Density Field

The density in each cell in the computational domain is obtained by the following expression,

$$\rho = \frac{1}{V_c} \sum_{j=1}^N m_j \quad (5.2)$$

where  $N$  is the number of molecules in the cell,  $m$  is the mass of the molecules, and  $V_c$  is the volume of the cell.

Effects of the altitude, the nose radius, and the gap  $L/H$  ratio on local density along the body normal direction, expressed as a ratio to the freestream value, are depicted in Fig. 5.7 parameterized by the gap  $L/H$  ratio. This group of plots presents data at three sections that correspond to the dimensionless arc length  $s/R$  of 0.70, 1.30, and 1.50, located on the spherical nose, immediately upstream and downstream the gap position on the capsule surface. In addition, the height  $\eta$  in the off-body direction is also normalized by the nose radius  $R$ . Again, filled and empty symbols correspond to the density ratio for altitude of 100 and 80 km, respectively. As a base of comparison, density ratio for the capsule surface without a gap are presented in the same plots as a solid line for both altitudes.

According to this group of plots, it is clearly noticed that the density experiences significant changes in the direction perpendicular to the wall as the flow moves downstream along the capsule surface. In the direction perpendicular to the wall, the density is high adjacent to the wall and rapidly decreases inside a layer of thickness smaller than one nose radius  $R$ , where the density approaches the freestream value for the altitudes investigated. This characteristic is observed when the body surface is very much colder than the stagnation temperature of the oncoming gas. As a result, the gas near the body tends to be much denser and cooler than the gas in the rest of the boundary layer.

It is very encouraging to observe that density is affected by changes in the altitude, as would be expected. It is seen that the density variation is one order of magnitude greater as compared to the freestream density for the cases investigated. For instance, for section  $s/R = 0.70$ , close to the stagnation region, the compression combined with a relatively cool wall produces a maximum density ratio  $\rho/\rho_\infty$  that lies in the range from 40 to 80. Also, because of the flow expansion along the capsule surface,

the density ratio adjacent to the surface decreases dramatically to the range from 5 to 20 for the section corresponding to  $s/R = 1.50$ , for the same altitudes investigated.

Still referring to Fig. 5.7, it is also observed that the gap  $L/H$  ratio has no significant effect on the density ratio for the sections shown. In contrast, as the capsule nose radius is reduced from  $R$  to  $R/4$ , a significant reduction is observed in the density ratio adjacent to the capsule surface. This behavior is expected in the sense that the body shape is changing from a blunt shape to an aerodynamically sharp.

Density ratio for three sections inside the gaps are exhibited in Fig. 5.8 parameterized by the gap  $L/H$  ratio. In this set of plots, again left- and right-column plots correspond, respectively, to density ratio for 100  $km$  and 80  $km$  of altitude. Based on these plots, it may be recognized that the density ratio increases from the top to bottom of the gap as  $\xi_L$  increases from the backward to the forward face surface. In addition, this increase is more pronounced as the altitude decreases from 100  $km$  to 80  $km$ .

In the following, in attempting to bring out the essential features of the density behavior, Fig. 5.9 illustrates contour maps along with streamline traces for the density ratio distribution inside the gaps. In this group of contour maps, the density is normalized by the freestream density  $\rho_\infty$ . Again, left- and right-column plots correspond to density ratio for altitude of 100 and 80  $km$ , respectively. According to these plots, it is noticed that the density ratio is low at the vicinity of the backward face and high close to the forward face surface. This is an expected behavior in the sense that the flow experiences an expansion around the backward face and a compression on the forward face surface. In addition, it is also noticed that the density  $\rho$  is, at least, thirty times the freestream density  $\rho_\infty$  at the bottom surface of the gaps, for the  $L/H$  ratio investigated.

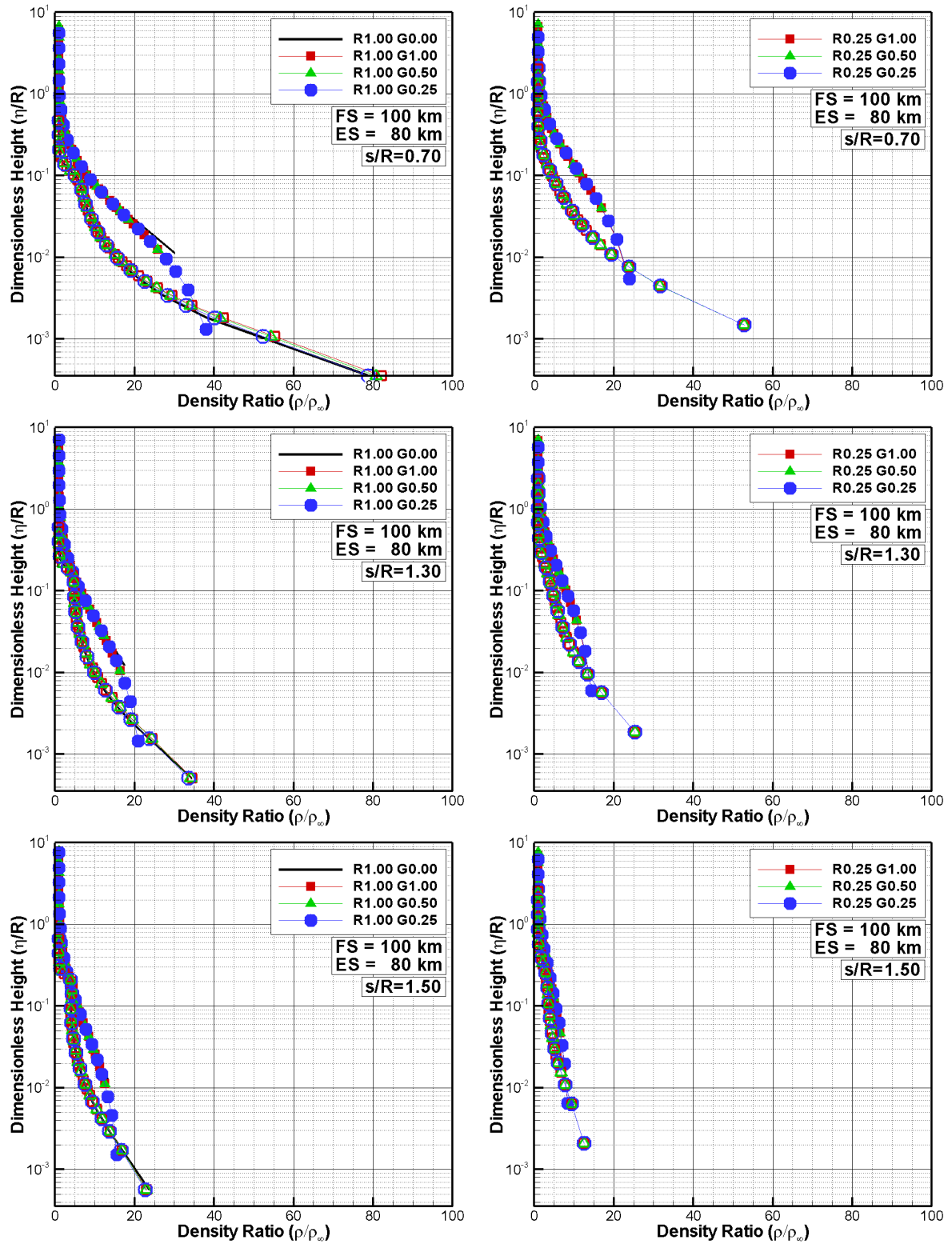


Figure 5.7 - Density ratio ( $\rho/\rho_\infty$ ) for three sections  $s/R$  along the capsule surface and altitudes of 100 and 80 km, parameterized by the gap  $L/H$  ratio and nose radius  $R$ .

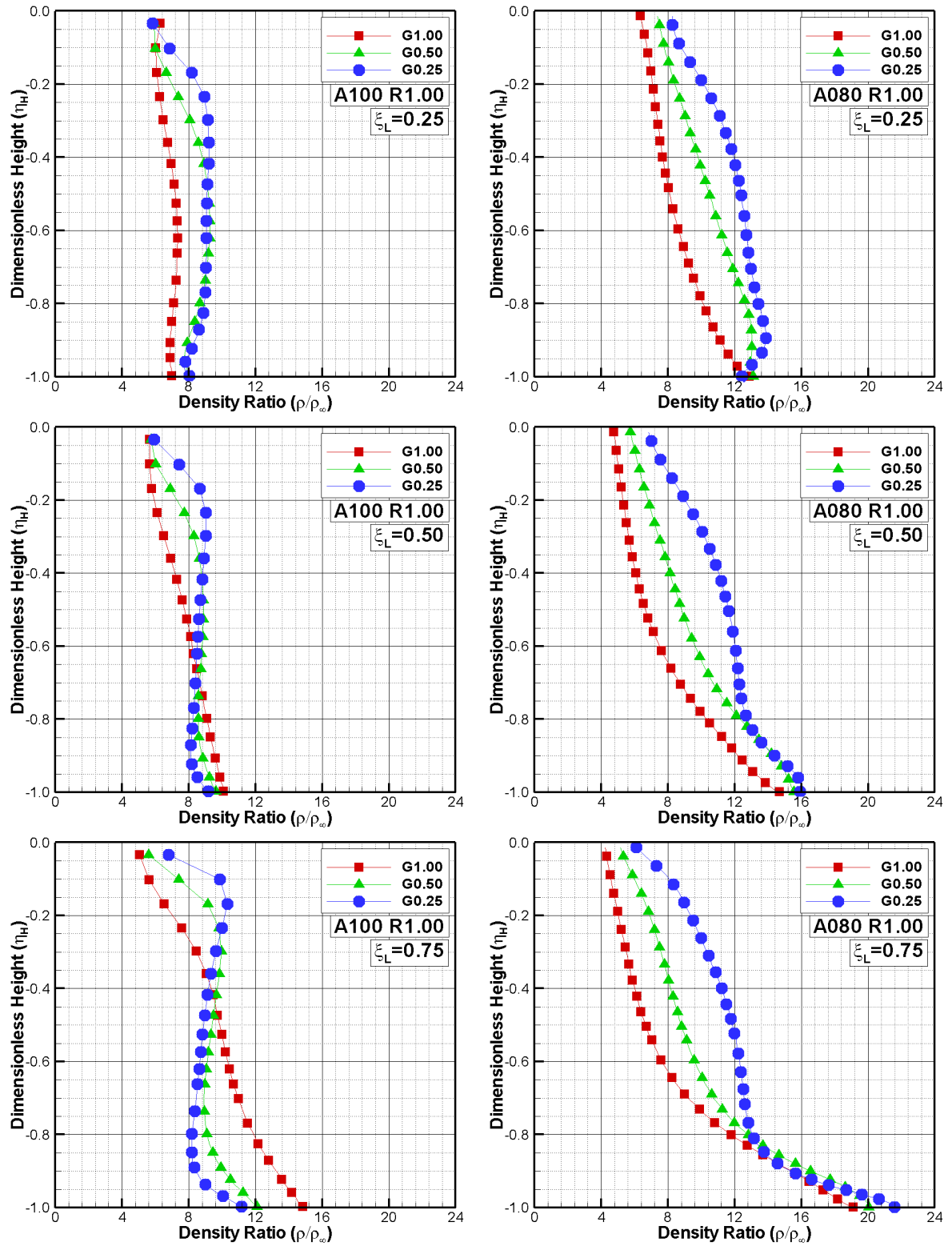


Figure 5.8 - Density ratio ( $\rho/\rho_\infty$ ) for three vertical sections inside the gap for altitude of 100 km (left) and 80 km (right), nose radius  $R$ , and gap  $L/H$  of 1, 1/2 and 1/4.

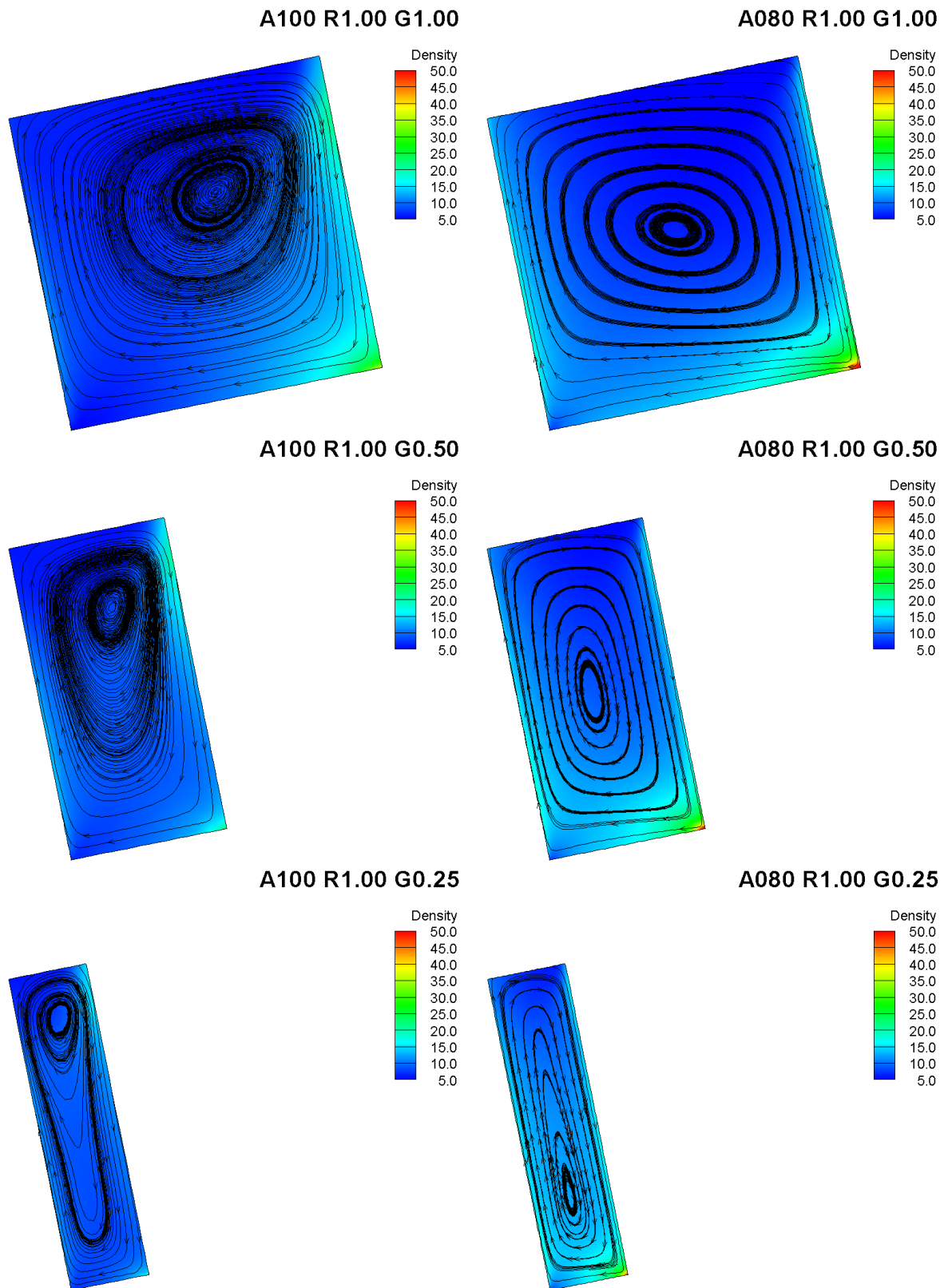


Figure 5.9 - Contour maps for density ratio along with streamline traces inside the gap for altitudes of 100 km (left) and 80 km (right), nose radius  $R$ , and gap  $L/H$  of 1, 1/2, and 1/4.

### 5.1.3 Pressure Field

The pressure in each cell in the computational domain is obtained by the following equation,

$$\bar{p} = \frac{1}{3V_c} \sum_{j=1}^N \frac{(mc'^2)_j}{N} \quad (5.3)$$

where  $N$  is the number of molecules in the cell,  $m$  is the mass of the molecules,  $V_c$  is the volume of the cell, and  $c'$  is the thermal velocity of the molecules.

The impact of the altitude, the nose radius, and the gap  $L/H$  ratio on local pressure ratio, expressed as a ratio to the freestream value  $p_\infty$ , along the body normal direction is demonstrated in Fig. 5.10, for three sections located on the capsule surface. It is apparent from these profiles that pressure is affected with decreasing the altitude as well as the capsule nose radius. Conversely, no impact is observed in the pressure ratio due to variations in the gap  $L/H$  ratio, for the sections shown. For the sections corresponding to  $s/R = 0.70$ , the pressure variation is almost two orders of magnitude larger than the freestream pressure for altitude of 80 km. In this region, at the vicinity of the stagnation point, the compression produces a maximum pressure that is around 800 times the freestream pressure for altitude of 80 km. Due to the flow expansion along the body surface, the pressure adjacent to the surface decreases significantly. For the particular case of 80 km, the pressure ratio  $p/p_\infty$  decreases to 300 for the section corresponding to  $s/R = 1.50$ , a reduction around 60% from section  $s/R$  of 0.70 to 1.50.

Still examining Fig. 5.10, it is noted that the extent of the flowfield disturbance in the off-body direction for pressure is significantly different from that presented by density and velocity. The domain of influence for pressure is higher than that for density and velocity. In the direction perpendicular to the wall, for 100 km of altitude, the pressure is high adjacent to the wall and decreases inside a layer of thickness larger than one nose radius  $R$ , where the pressure approaches the freestream value  $p_\infty$ .

Pressure ratio for three sections inside the gaps are depicted in Fig. 5.11 parameterized by the gap  $L/H$  ratio. Again, in this set of plots, left- and right-column plots correspond, respectively, to density ratio for 100 km and 80 km of altitude. According these plots, it may be realized that the pressure ratio decreases from the top to

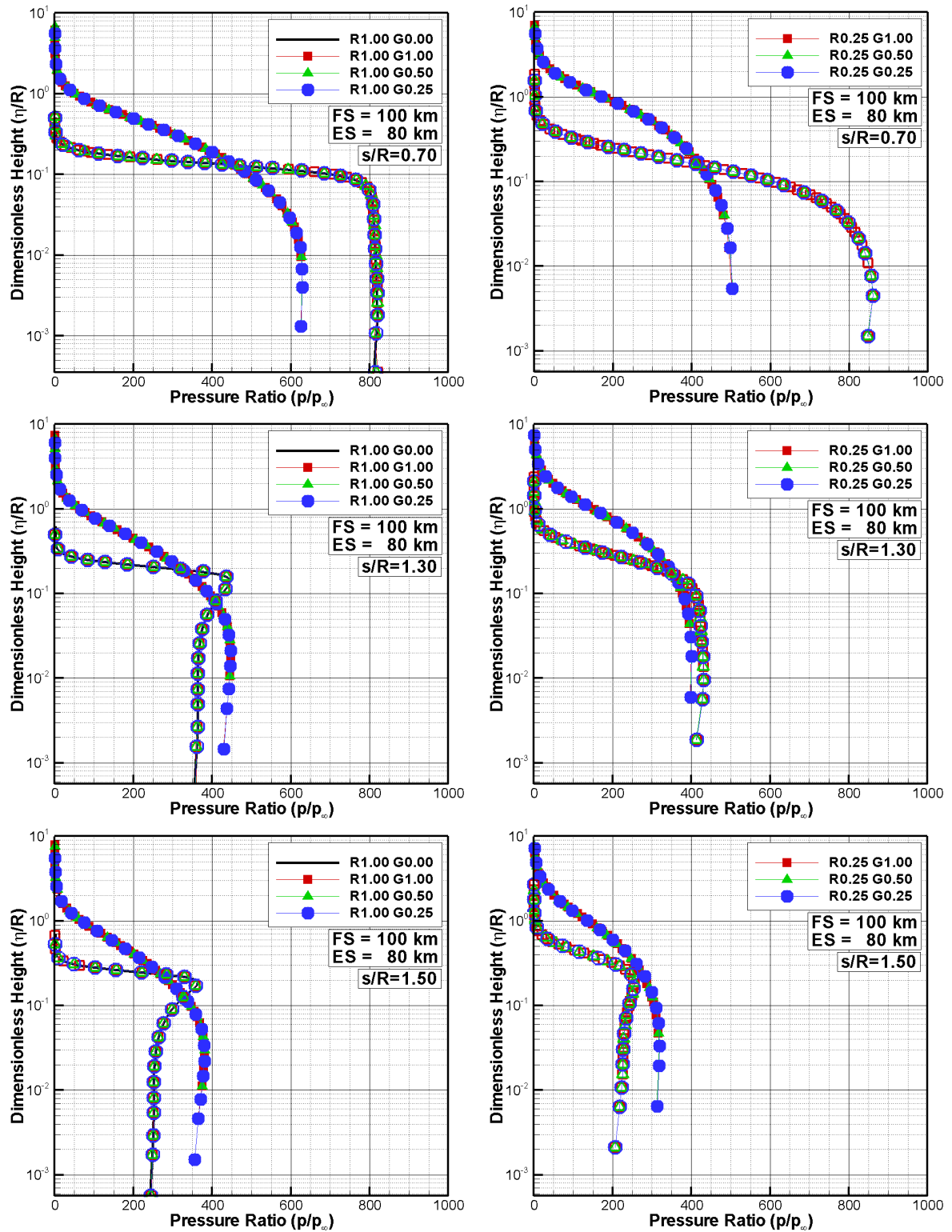


Figure 5.10 - Pressure ratio ( $p/p_\infty$ ) for three sections  $s/R$  along the capsule surface and altitudes of 100 and 80 km, parameterized by the gap  $L/H$  ratio and nose radius  $R$ .

bottom of the gap as  $\xi_L$  increases from the backward to the forward face surface for an altitude of 100 *km*. This behavior is in contrast to that one observed for the density, as shown earlier. In addition, as the altitude decreases from 100 *km* to 80 *km*, pressure ratio is almost constant for the three sections shown. Nevertheless, the pressure increases inside the gap, around two orders of magnitude as compared to the freestream pressure  $p_\infty$ .

In what follows, in order to gain some insight into the pressure behavior, Fig. 5.12 exhibits contour maps along with streamline traces for pressure ratio distribution inside the gaps. In this set of contour maps, the pressure is normalized by the freestream pressure  $p_\infty$ . Again, left- and right-column plots correspond to pressure ratio for altitude of 100 and 80 *km*, respectively. According to these plots, it is observed that peak values for pressure take place at the vicinity of the gap corner on the forward face surface. However, as the altitude decreases from 100 *km* to 80 *km*, pressure ratio also increases in the gap corner close to the bottom surface. Certainly, this behavior is related to the flow entering into the gap with a given angle of attack along with high density. As mentioned earlier, the flow experiences a compression on the forward face surface.

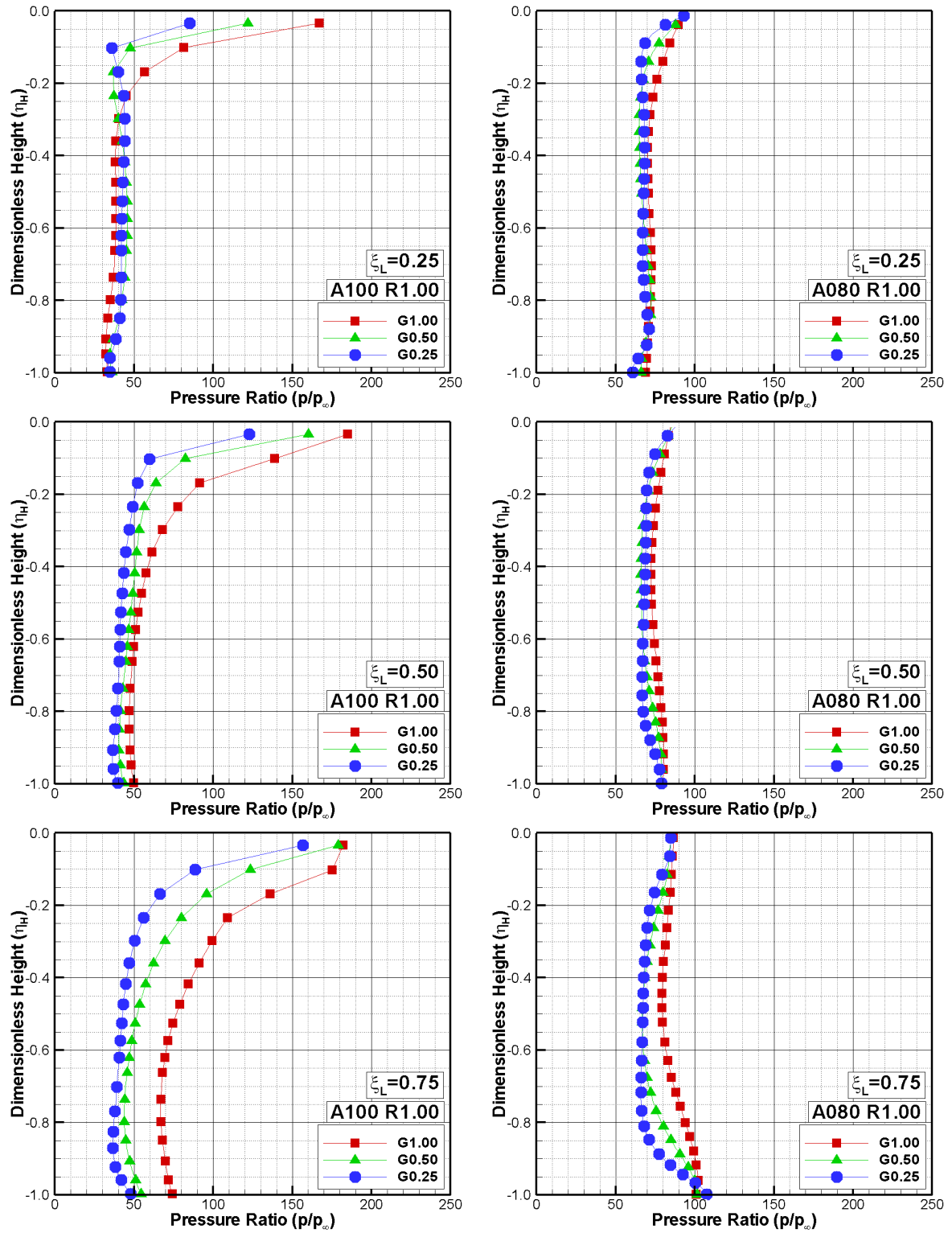


Figure 5.11 - Pressure ratio ( $p/p_\infty$ ) for three vertical sections inside the gap for altitudes of 100 km (left) and 80 km (right), nose radius  $R$ , and gap  $L/H$  of 1, 1/2 and 1/4.

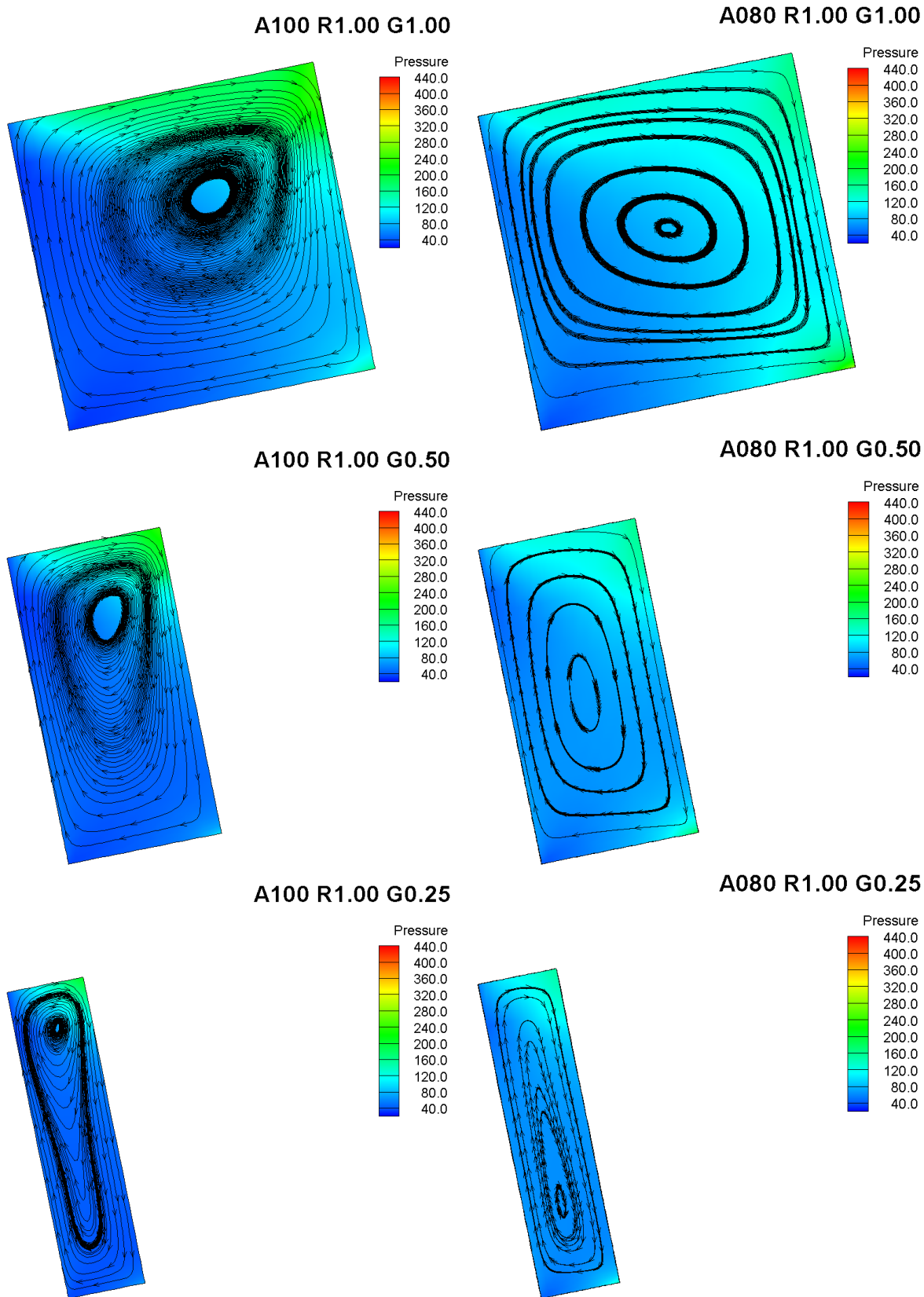


Figure 5.12 - Contour maps for pressure ratio ( $p/p_\infty$ ) along with streamline traces inside the gap for altitude of 100 km (left) and 80 km (right), nose radius  $R$ , and gap  $L/H$  of 1, 1/2, and 1/4.

### 5.1.4 Temperature Field

In a diatomic or polyatomic gas in complete thermodynamic equilibrium, the translational temperature is equal to the temperature related to the internal modes, i.e., rotational, vibrational, or electronic temperatures, and it is identified as thermodynamic temperature. When the equilibrium is disturbed, relaxation processes arise in the system that attempt to return it to the state of the total statistical equilibrium. In diatomic or polyatomic gas, there are processes which results in the establishment of equilibrium with respect to individual degrees of molecular freedom such as translational, rotational, vibrational or electronic. Conversely, in a thermodynamic non-equilibrium gas, an overall temperature is defined as the weighted mean of the translational and internal temperatures (BIRD, 1994) as being,

$$T_O = \frac{\zeta_T T_T + \zeta_R T_R + \zeta_V T_V}{\zeta_T + \zeta_R + \zeta_V} \quad (5.4)$$

where  $T$  and  $\zeta$  stand for the temperature and the degree of freedom, respectively, and subscripts  $T$ ,  $R$  and  $V$  refer to translation, rotation and vibration, respectively.

Translational, rotational, and vibrational temperatures are obtained to each cell in the computational domain by the following equations,

$$T_T = \frac{1}{3k} \sum_{j=1}^N \frac{(mc'^2)_j}{N} \quad (5.5)$$

$$T_R = \frac{2\bar{\epsilon}_R}{k\zeta_R} \quad (5.6)$$

$$T_V = \frac{\Theta_V}{\ln(1 + \frac{k\Theta_V}{\bar{\epsilon}_V})} \quad (5.7)$$

where  $k$  is the Boltzmann constant,  $\Theta_V$  is the characteristic temperature of vibration, and  $\bar{\epsilon}_R$  and  $\bar{\epsilon}_V$  are, respectively, rotation and vibration average energies in each cell.

Starting with Fig. 5.13, it shows the effects of the altitude, the nose radius and the gap  $L/H$  ratio on kinetic and internal modes temperatures normalized by the freestream temperature  $T_\infty$  for three sections  $s/R$  of the capsule. It is evident that the non-equilibrium occurs for all the sections investigated, as shown by the lack of

equilibrium between the translational and internal kinetic temperatures. As mentioned earlier, thermal non-equilibrium occurs when the temperatures associated with the translational, rotational, and vibrational modes of a polyatomic gas are different. It should be mentioned in this context that the overall temperature, defined by Eq. 5.4, is equivalent to the thermodynamic temperature only under thermal equilibrium conditions. In addition, the ideal gas equation of state does not apply to this temperature in a non-equilibrium situation. It should be recognized that, in the undisturbed freestream far from the capsule surface,  $\eta/R \rightarrow \infty$ , the translational and internal kinetic temperatures have the same value and are equal to the thermodynamic temperature.

Still referring to Fig. 5.13, it is possible to infer that near the capsule surface  $\eta/R \rightarrow 0$ , the translational kinetic temperature tends to a constant value on the wall, for the sections investigated, that is above the wall temperature  $T_w \approx 4T_\infty$ , resulting in a temperature jump as defined in continuum formulation (GUPTA et al., 1985), moreover, as the altitude decreases, the thermodynamic non-equilibrium near the leading edge surface becomes lower, due to the fact that the local mean free path decreases and the mean collision frequency increases and, therefore, the flow tends to the thermal equilibrium. It is clear that gap presence did not modified the temperature ratio since it is the same presented for the capsule without a gap showed as a solid black lines.

Variation on the kinetic temperature normalized by the freestream temperature  $T_\infty$  for the same three sections along the capsule surface are exhibited in Fig. 5.14 in function of the variation on the gap  $L/H$  ratio and nose radius ratio. The figures shows that the translational temperature ratio ( $T_T/T_\infty$ ) become smaller as the section  $s/R$  becomes larger, i.e, as the section moves away from the capsule leading edge. An important result is that the effects on the variations of the nose radius ratio seems negligible for the cases where the altitude are equal 80 km and become more apparent when the altitude increases to 100 km.

In the following, the temperature ratio inside the gaps for the nose radius ratio  $R = 1.00$  and section equals  $\xi_L = 0.25, 0.50$  and  $0.75$  are shown in Fig. 5.15. According to this set of plots, it is apparent that the kinetic temperature ratio  $T/T_\infty$  decreases and reaches a constant value on the bottom surface, which corresponds to the wall temperature ( $T_w \approx 4T_\infty$ ). At the bottom surface, it is seen that the flow is thermal equilibrium, once the internal temperatures are equal to the translational temperature. Regarding to altitude effects, it is remarkable that for the 80 km

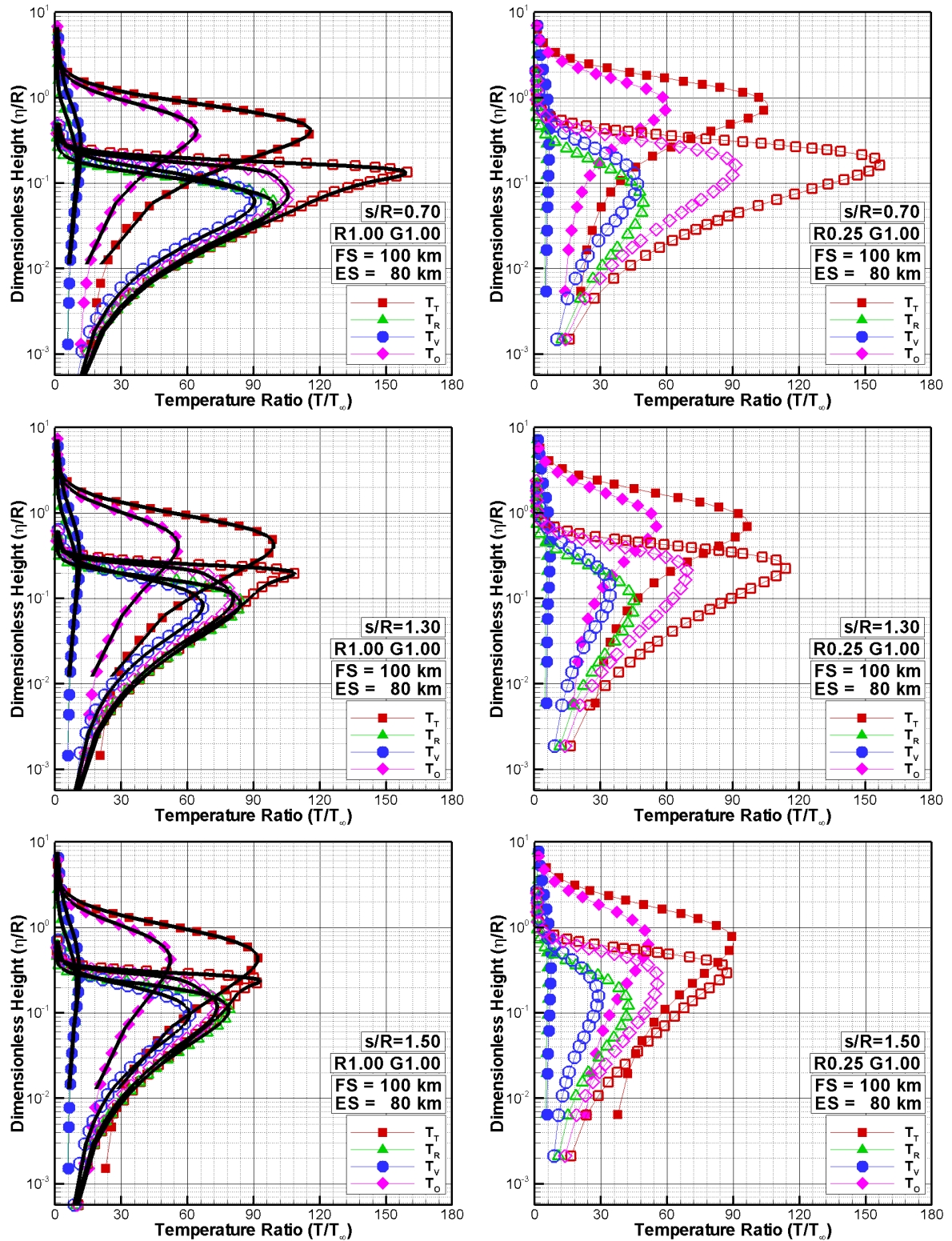


Figure 5.13 - Temperature ratio ( $T/T_\infty$ ) for three sections  $s/R$  along the capsule surface and altitudes of 100 and 80 km, parameterized by the gap  $L/H$  ratio and nose radius  $R$ .

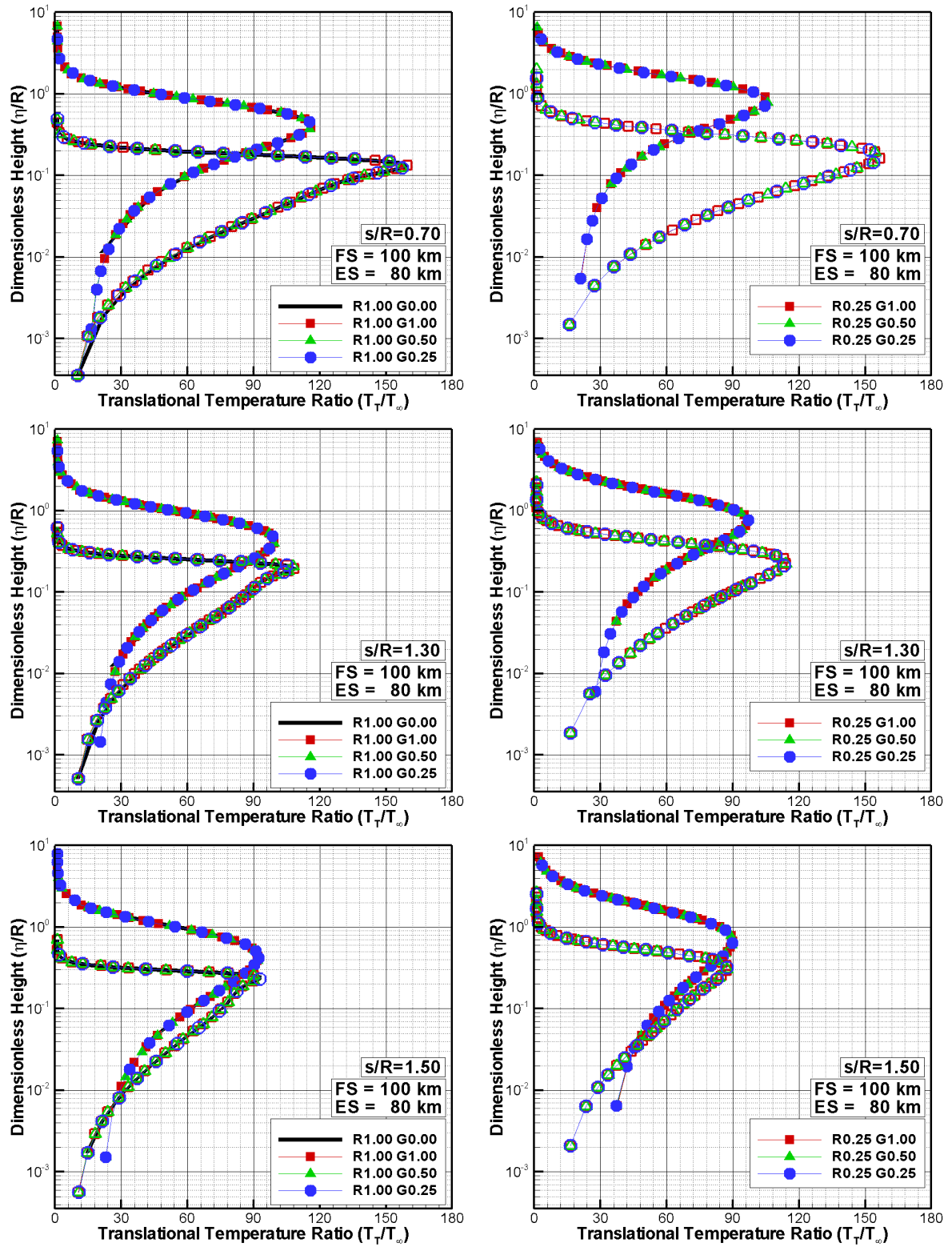


Figure 5.14 - Translational temperature ratio ( $T_T/T_\infty$ ) for three sections  $s/R$  along the capsule surface and altitudes of 100 and 80 km, parameterized by the gap  $L/H$  ratio and nose radius  $R$ .

case, it presents the same behavior as those presented for 100 *km*, however, the nonequilibrium degree is lower.

And finally, the translational temperature ratio ( $T_T/T_\infty$ ) inside the gap for altitudes of 100 and 80 *km* are depicted in Fig. 5.16 due to variations on the nose ratio and gap  $L/H$  ratio. A remarkable behavior in this figure is that as the  $\xi_L$  approaches the forward gap face, higher are the translational temperature ratio since it presents a compression region. Moreover comparing the altitude effects, it is clear that higher altitudes presented higher translational temperature ratio at the top of the gap, near 2 times greater than those presented for 80 *km*.

Lastly, it is desirable to present contour maps for the translational temperature ratio inside the gaps. In this fashion, Fig. 5.17 depicts the translational temperature contour maps along with streamline traces for pressure ratio distribution inside the gaps. In this set of contour maps, the translational temperature is normalized by the freestream temperature  $T_\infty$ . Again, left- and right-column plots correspond to translational temperature ratio for altitude of 100 and 80 *km*, respectively. According to these plots, it is observed that peak values for translational temperature take place at the top of the gap near to the forward face surface.

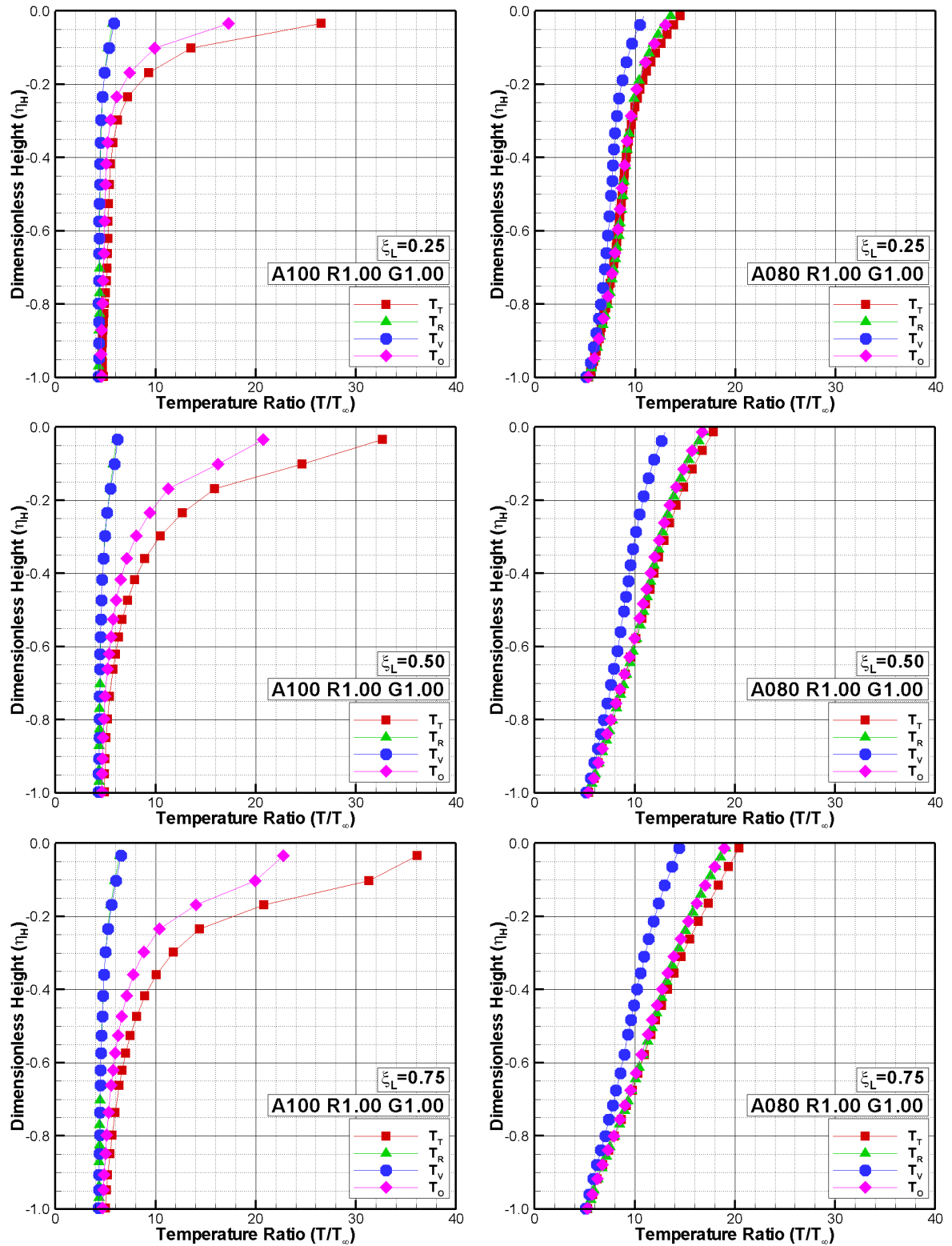


Figure 5.15 - Temperature ratio ( $T/T_\infty$ ) for three sections  $\xi_L$  inside the gap for altitude 100 km (left) and 80 km (right) for radius ratio  $R = 1.00$  and gap ratio  $G = 1.00$ .

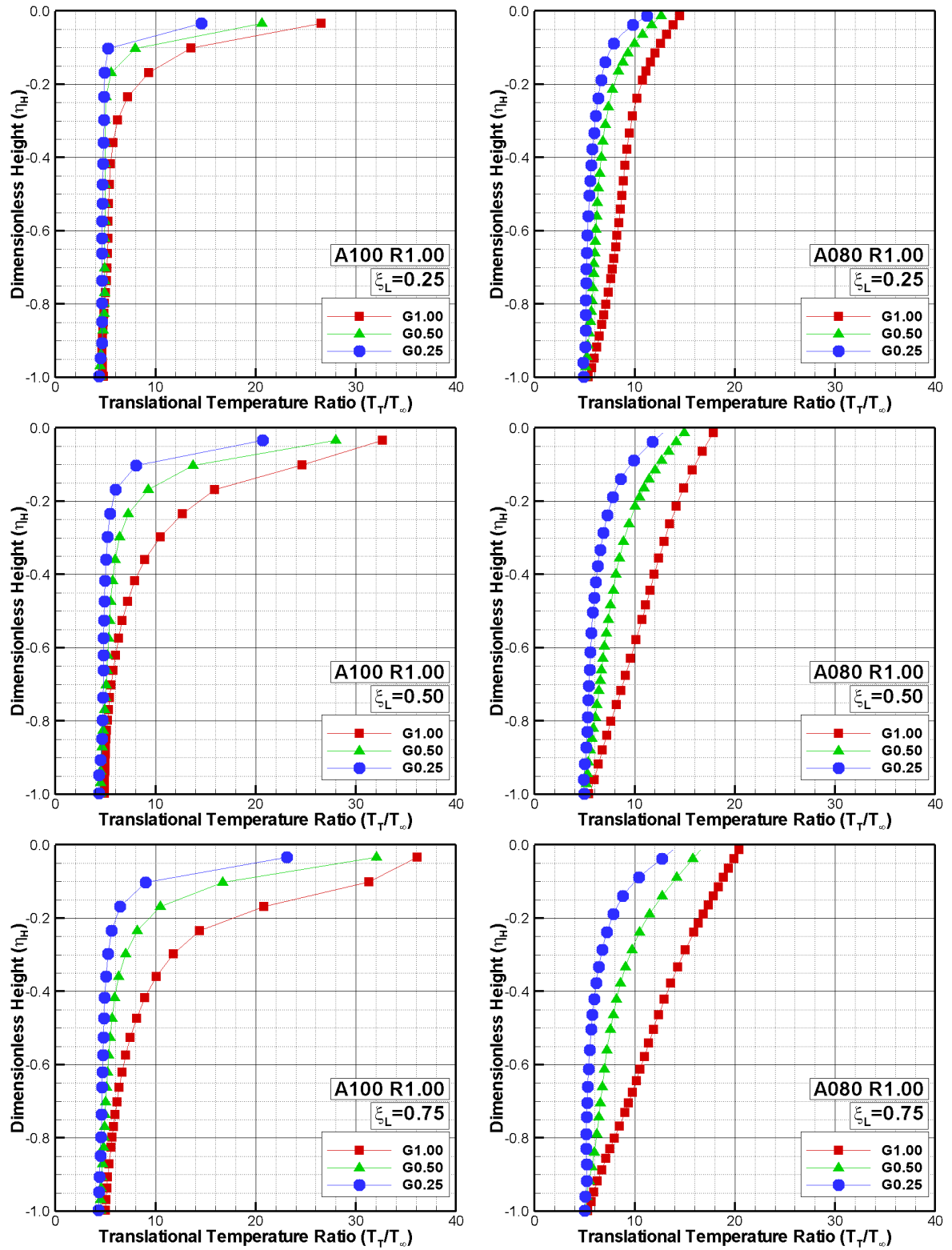


Figure 5.16 - Translational temperature ratio ( $T_T/T_\infty$ ) for three sections  $\xi_L$  inside the gap for altitude of 100 km (left) and 80 km (right) for radius ratio  $R = 1.00$  and gap ratio  $G = 1.00$ .

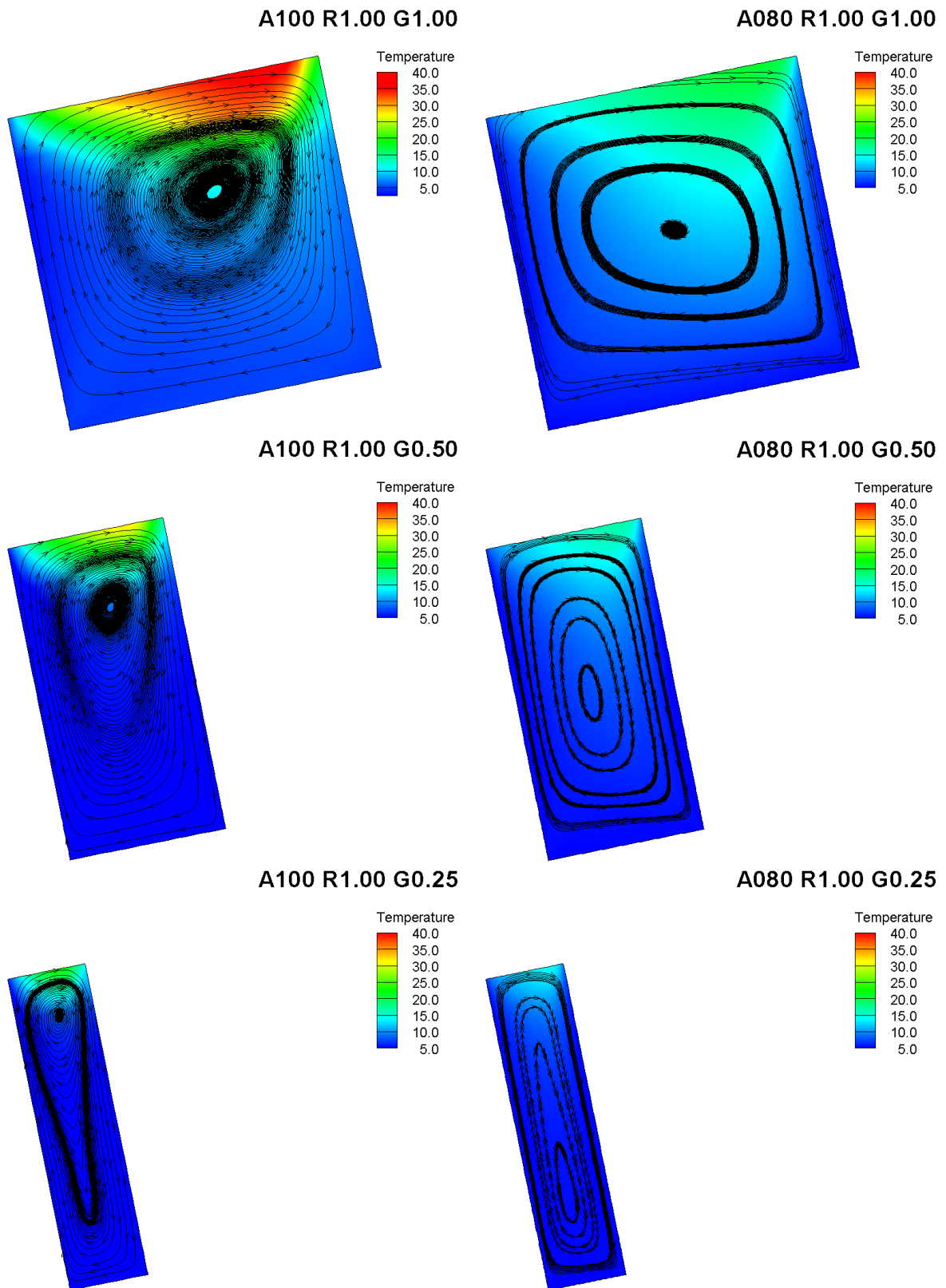


Figure 5.17 - Translational temperature ratio ( $T_T/T_\infty$ ) inside the gaps parameterized by the gap  $L/H$  ratio of 1, 1/2 and 1/4 and altitude of 100 km (left) and 80 km (right).

## 5.2 Aerodynamic Surface Properties

Proceeding in a manner analogous to the treatment in the previous section, this section provides a detail discussion on the aerodynamic surface properties. The aerodynamic surface properties of particular interest in this work are the number flux, heat transfer, pressure, skin friction and drag coefficients.

### 5.2.1 Number Flux

The number flux  $N$  is calculated by sampling the molecules impinging on the surface by unit time and area. For convenience, it proves helpful to separate the presentation of the results on the aerodynamic surface properties into five segments, surfaces  $S1$  and  $S5$ , correspondent to the surfaces outside the gap, and surfaces  $S2$ ,  $S3$  and  $S4$ , inside the gap, as defined earlier in Figure 3.3.

Effects of the altitude, the nose radius, and the gap  $L/H$  ratio on the number flux along surfaces  $S1$  and  $S5$  are illustrated in Figure 5.18. In this group of plots,  $N_f$  represents the number flux  $N$  normalized by  $n_\infty U_\infty$ , where  $n_\infty$  is the freestream number density and  $U_\infty$  is the freestream velocity. In addition,  $s$  is the arc length, measured from the stagnation point, normalized by the nose radius  $R$ . Filled and empty symbols stand for results on surface  $S1$  and  $S5$ , respectively. Furthermore, the left-column plots refer to the distribution of the number flux for an altitude of 100 km, while the right-column plots correspond to the distribution on the surfaces for an altitude of 80 km. Results for altitude of 90 km are intermediate, and they are not shown in this group of plots. Moreover, top-, middle-, and bottom-row plots correspond to results for nose radius of  $R$ ,  $R/2$  and  $R/4$ , respectively. As a base of comparison, the number flux distribution for a capsule without a gap (SANTOS, 2010) is also illustrated in this group of plots.

On examining first the left-column plots, for an altitude of 100 km, it is noticed that the number flux behavior to the surfaces outside the gap basically follows that for a capsule without a gap. Except very close to the gap position, no upstream disturb is caused by the presence of the gap. Along surface  $S5$ , no appreciable changes, as compared to that for a capsule without a gap, are observed in the number flux distribution, excepted at the vicinity of the gap shoulder, i.e., at the surface-S4/surface-S5 junction, as illustrated in the magnified view. On the other hand, this small effect at the vicinity of the gap shoulder increases with increasing the gap  $L/H$  ratio, i.e., by increasing the gap length  $L$  in this investigation. Due to the flow expansion on the gap shoulder the density is low in this region. As a result,

the number flux to the surface at the vicinity of the gap shoulder is smaller than that for a capsule without a gap at the corresponding section.

Turning next to right-column plots, for an altitude of 80 *km*, it is clearly noticed that the distribution of the number flux follows the same trend as that for an altitude of 100 *km*, for the nose radius and the gap  $L/H$  ratio investigated. Nevertheless, the number flux increases significantly on the stagnation point, surface  $S1$ . As the capsule enters a little deeper into the dense atmosphere, from 100 *km* to 80 *km*, the mean free path from incoming freestream molecules decreases and, therefore, density increases. At the vicinity of the spherical nose the molecules that are reflected upstream, which have a lower kinetic energy, interact with the oncoming freestream molecules, which have a higher kinetic energy. Thus, the surface-reflected molecules recollide with the surface, which produces an increase in the dimensionless number flux in the stagnation region.

An understanding of the number-flux behavior can be gained by considering the equations for free-molecular flow. As mentioned in Chapter 1, free-molecular flow or collisionless flow is the limiting case in which the Knudsen number tends to infinity. Knudsen number tends to infinity for high mean free paths, therefore, low densities, or with small characteristic dimensions. For high altitude, for instance 100 *km*, freestream density is low and, therefore, the Knudsen number may be a high value. On the other hand, as the characteristic length is small, for instance, as the nose radius decreases from  $R$  to  $R/4$ , the Knudsen number may be a high value.

The basic assumption is that intermolecular collisions can be neglected. The fluxes of mass, momentum and energy incident on and reflected from a surface element can be treated separately and do not interfere with each other. The incident flux is entirely unaffected by the presence of the surface. By considering free-molecular flow, the number flux is given by the following equation,

$$N_{mf} = \frac{N}{n_{\infty}U_{\infty}} = \frac{1}{2\sqrt{\pi}S_{\infty}}[\exp(-\chi^2) + \sqrt{\pi}\chi(1 + \operatorname{erf}\chi)] \quad (5.8)$$

where  $\chi = S_{\infty}\sin\theta$ ,  $S_{\infty} = \frac{U_{\infty}}{\sqrt{2RT_{\infty}}}$  and  $\theta$  is the body slope angle.

As a base of comparison, by considering free-molecular flow, for an altitude of 100 *km*, the number flux  $N_{mf}$  is 1.0 and 0.197 for body slope angles of 90 and 11.4 degrees, respectively. These slope angles correspond, respectively, to the stagnation point in the spherical nose and the conical afterbody. According to Fig. 5.18, for an

altitude of 100 *km* and nose radius of  $R/4$ , the number flux at the same stations is 1.47 and 0.23. Therefore, as the nose radius is reduced from  $R$  to  $R/4$ , the flow around the nose approaches the free-molecular flow.

The impact of the altitude, the nose radius, and the gap  $L/H$  ratio on the number flux to the surfaces inside the gap is demonstrated in Figures 5.19, 5.20 and 5.21, for surfaces  $S2$ ,  $S3$ , and  $S4$ , respectively. In this set of plots, the height  $\eta$  in the off-body direction ( $\eta$ -direction in Fig. 3.3) is normalized by the gap height  $H$ , and therefore,  $\eta/H$  of 0 and -1 correspond to the top and bottom of the gaps. In addition, the length  $\xi$  ( $\xi$ -direction in Fig. 3.3) is normalized by the gap length  $L$ . Therefore,  $\xi/L$  of 0 and 1 correspond, respectively, to surface-S2/surface-S3 junction and surface-S3/surface-S4 junction. Again, the left-column plots refer to the distribution of the number flux for an altitude of 100 *km*, while the right-column plots correspond to the distribution on the surfaces for an altitude of 80 *km*. Furthermore, top-, middle-, and bottom-row plots correspond to results for nose radius of  $R$ ,  $R/2$ , and  $R/4$ , respectively.

Looking first at left-column plots of Fig. 5.19, for the backward face, surface  $S2$ , the number flux is low at the gap shoulder, surface-S1/surface-S2 junction, it basically increases gradually along the surface up to the corner at the bottom surface, surface  $S3$ , where it reaches the maximum value. In addition, a similar behavior is observed as the nose radius is decreased from  $R$  to  $R/4$ . As the altitude decreases from 100 *km* to 80 *km*, right-column plots, a slightly different pattern is observed in the number flux as the gap  $L/H$  ratio change from 1 to 1/4. It is seen that the maximum values for the number flux take place not at the corner, surface-S2/surface-S3 junction, but close to the corner. It is also seen that the number flux to surface  $S2$  decreases with decreasing the nose radius, for an altitude of 80 *km*. This behavior is related to the recirculation region and the density distribution inside the gaps, as shown earlier.

Along the gap floor, surface  $S3$ , Figure 5.20, the number flux basically presents a similar behavior for the altitude, nose radius, and gap  $L/H$  ratio range investigated. It is clearly noted that the number flux is low at the surface-S2/surface-S3 junction and increases along the bottom surface up to the surface-S3/surface-S4 junction. It is also noted that the maximum value for the number flux at the surface-S3/surface-S4 junction decreases with decreasing not only the gap  $L/H$  ratio but also the nose radius. Conversely, the number flux increases with decreasing the altitude. This is an expected behavior in the sense that density increases inside the gap with decreasing the altitude. Moreover, the flow experiences a expansion at the vicinity of surface

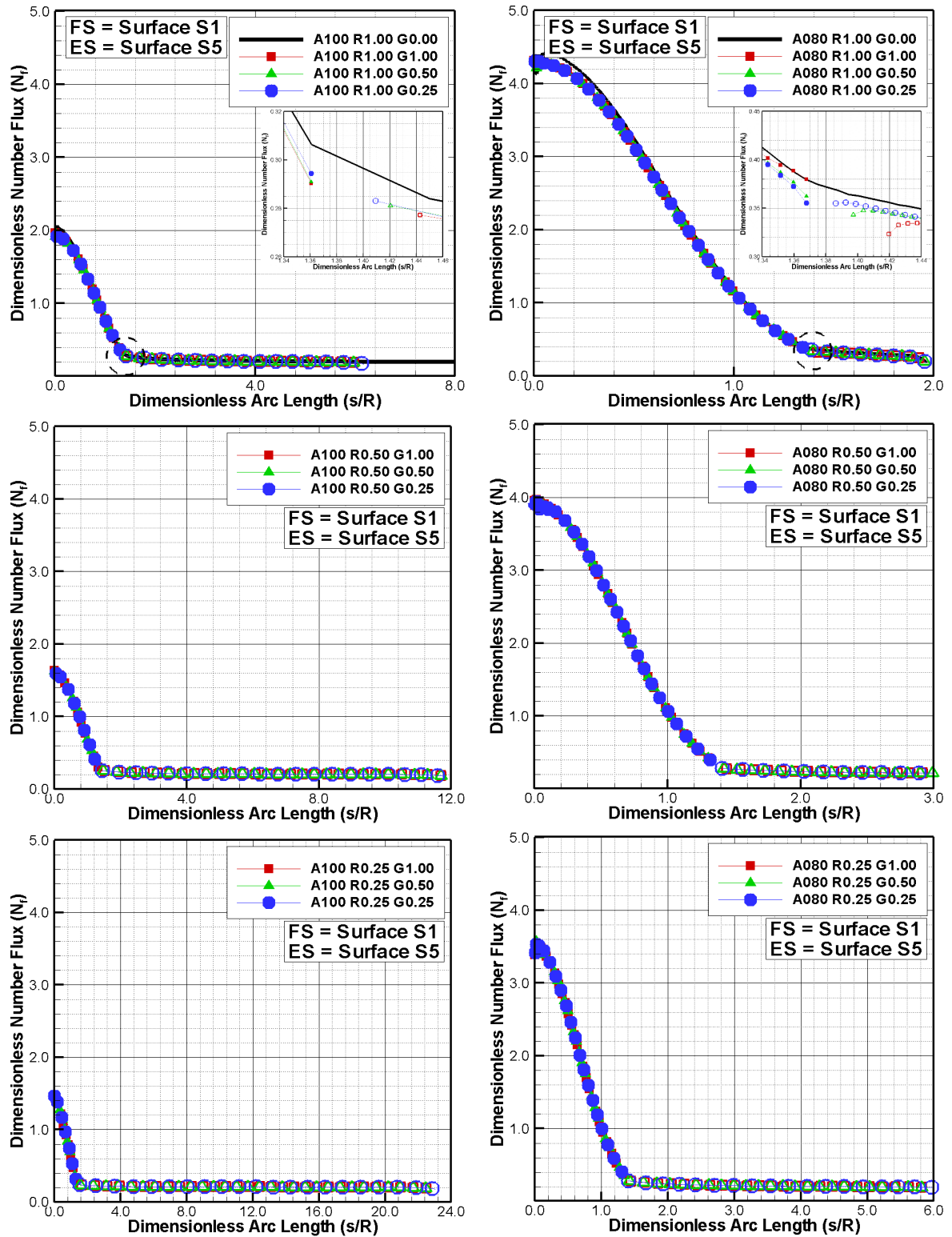


Figure 5.18 - Dimensionless number flux ( $N_f$ ) distribution along surfaces  $S1$  and  $S5$  as a function of the dimensionless arc length  $s/R$  parameterized by the altitude, nose radius, and the gap  $L/H$  ratio.

$S2$ , and a compression at the vicinity of surface  $S4$ .

In the following, along the forward face, surface  $S4$ , Figure 5.21,  $N_f$  basically increases from the corner, at the bottom surface, up to the top of the gap. This behavior is in contrast to that observed for the backward face. In fact, this is an expected behavior in the sense that it is directly related to the flow recirculation inside the gaps, as pointed out earlier. Due to the clockwise flow recirculation, at the vicinity of the surface  $S4$ , density is higher than that close to surfaces  $S2$  and  $S3$ . Therefore, a larger flux of molecules colliding to this surface is expected. In addition, as the altitude decreases from  $100\text{ km}$  to  $80\text{ km}$ , the number flux increases dramatically close to the gap corner, i.e., close to the surface- $S4$ /surface- $S5$  junction, for the conditions investigated. This is related to the flow compression on this side of the gaps.

Before proceeding with the analysis, it is desirable to present two effects associated to the collision process involving the freestream molecules and the surface-reflected molecules. The coupling of the surface-reflected molecules and freestream molecules disturbs the molecular flux to the body by either a shielding effect or an enhancing effect. In the shielding effect, molecules that are reflected upstream interact with the oncoming freestream molecules and recollide with the surface. In this situation, the freestream molecules do not reach the surface. In the enhancing effect, a portion of the oncoming freestream molecules is scattered to the surface after interaction with the surface-reflected molecules, thus resulting in an enhancement of the surface flux. The blunter the leading edge is the higher the density at the vicinity of the nose. In this way, this layer of high density acts as a shield for the molecules oncoming from the freestream. As a result, only part of the energy and momentum of the freestream molecules, diffusing into this layer, reaches the body surface. As the nose radius decreases from  $R$  to  $R/4$ , this density layer decreases and a larger fraction of the energy and momentum of the freestream molecules are transferred to the body surface. In this situation, the velocities of the molecules are those that are more characteristic of the freestream velocity. Consequently, the aerodynamic forces and the heat transfer may increase close to the stagnation point (next sections), although the number flux is decreasing with decreasing the nose radius, as the shape of the body is changing from blunt to sharp.

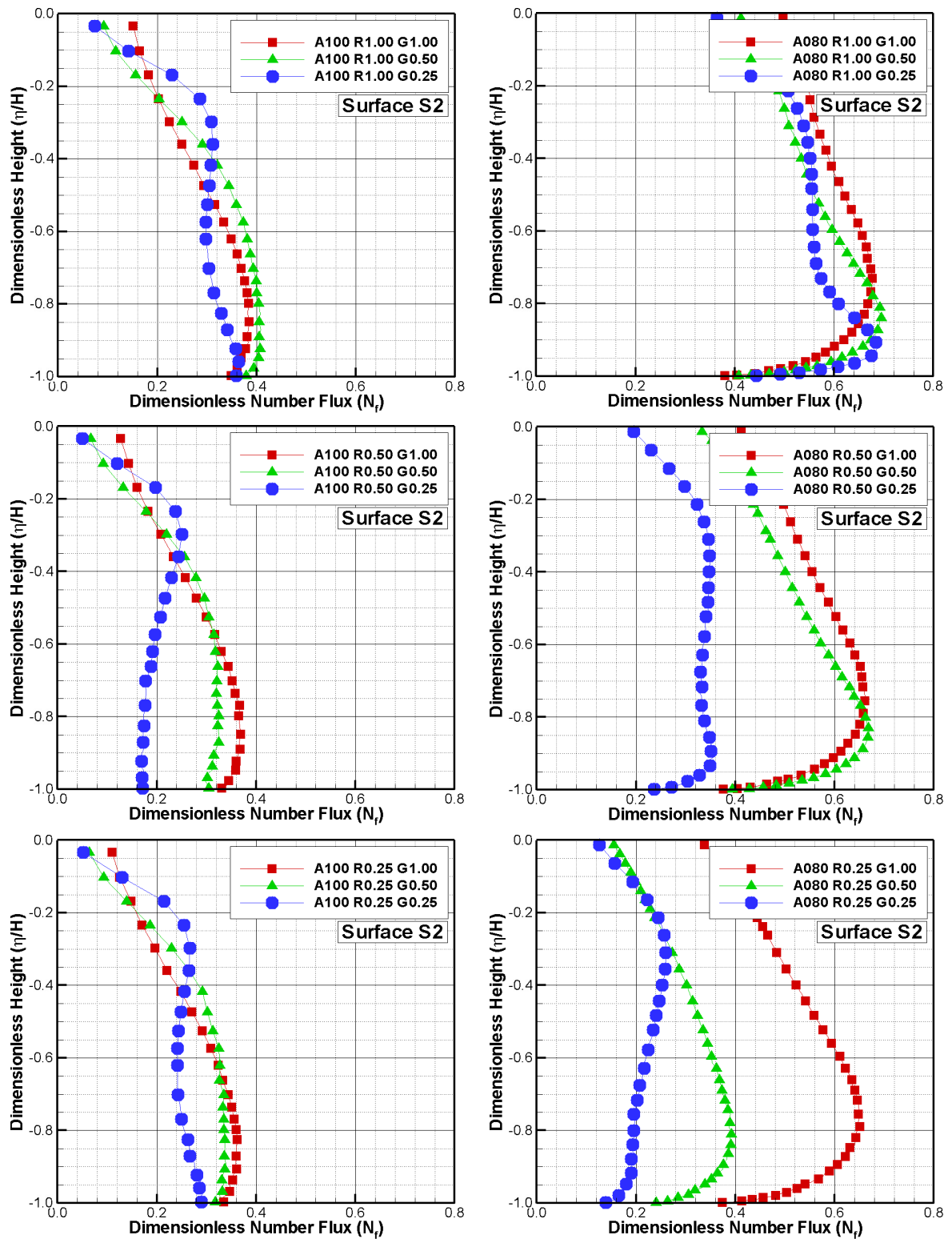


Figure 5.19 - Dimensionless number flux ( $N_f$ ) along surface  $S2$  as a function of the dimensionless height  $\eta/H$ , parameterized by the altitude, nose radius and the gap  $L/H$  ratio.

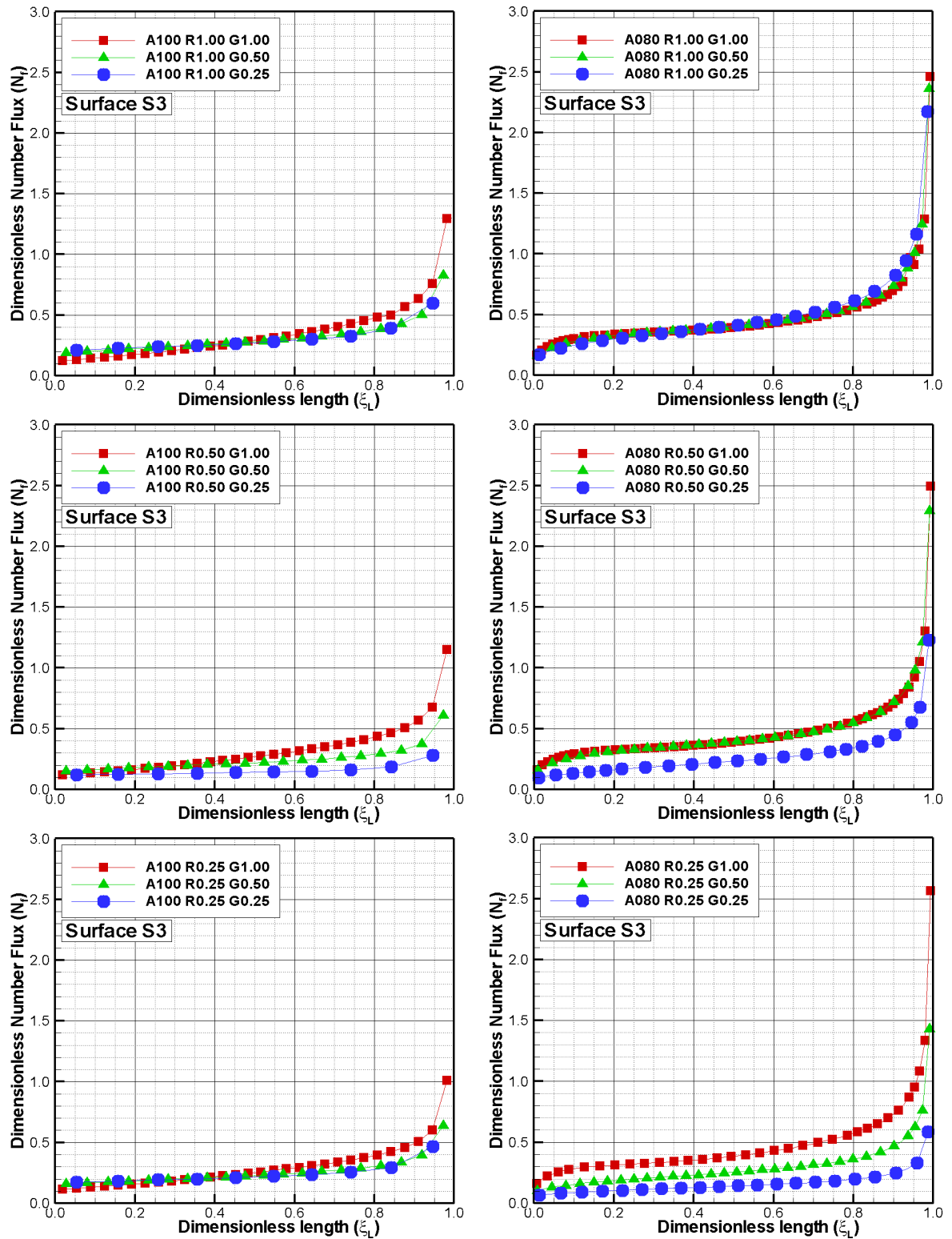


Figure 5.20 - Dimensionless number flux ( $N_f$ ) along surface  $S3$  as a function of the dimensionless length  $\xi_L$ , parameterized by the altitude, nose radius and the gap  $L/H$  ratio.

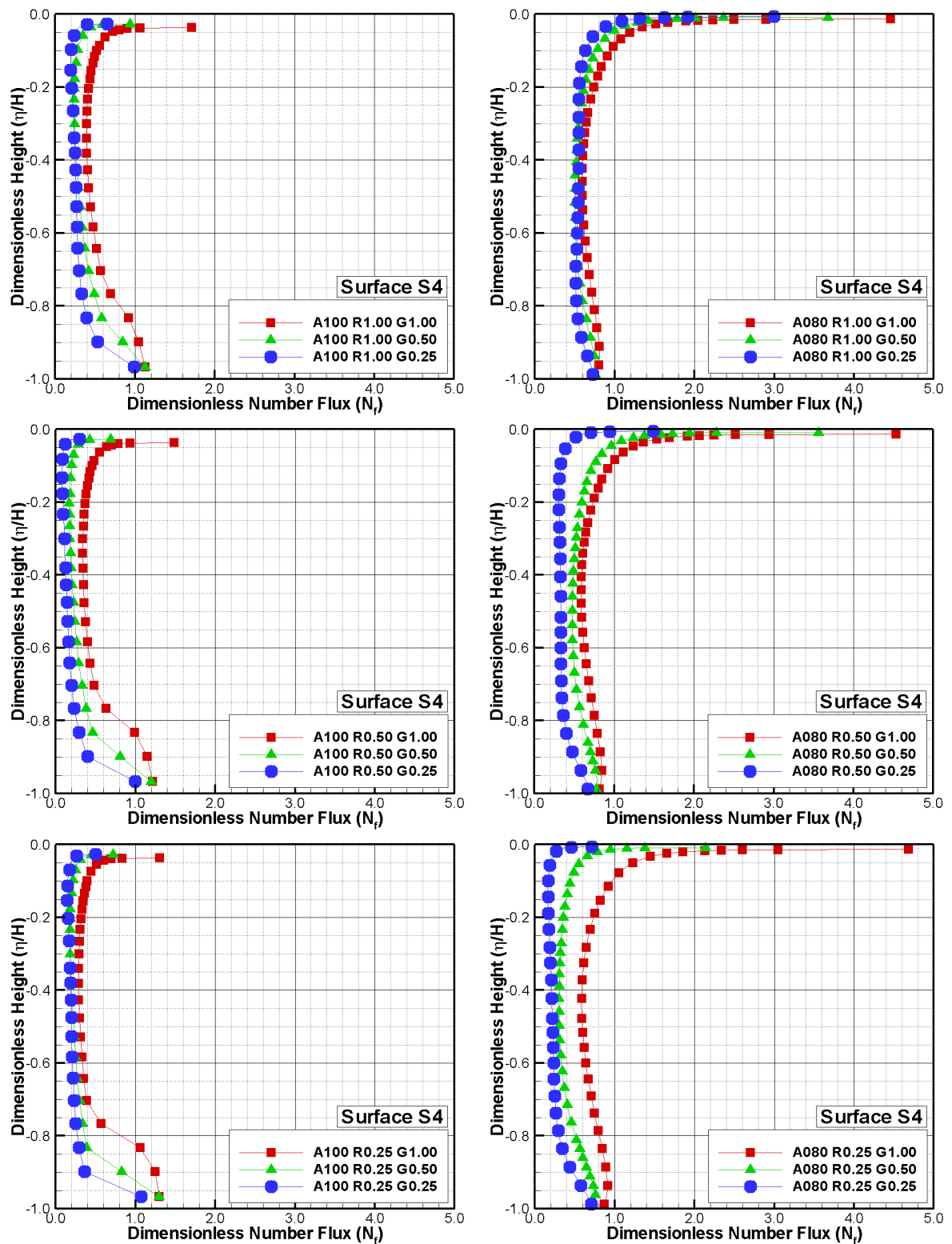


Figure 5.21 - Dimensionless number flux ( $N_f$ ) along surface  $S4$  as a function of the dimensionless height  $\eta/H$ , parameterized by the altitude, nose radius and the gap  $L/H$  ratio.

### 5.2.2 Heat Transfer Coefficient

The heat transfer coefficient is defined as follows,

$$C_h = \frac{q_w}{\frac{1}{2}\rho_\infty U_\infty^3} \quad (5.9)$$

where the heat flux  $q_w$  to the body surface is calculated by the net energy flux of the molecules impinging on the surface.

A flux is regarded as positive if it is directed toward the body surface. The net heat flux  $q_w$  is related to the sum of the translational, rotational and vibrational energies of both incident and reflected molecules as defined by,

$$q_w = q_i - q_r = \frac{F_N}{A\Delta t} \sum_{j=1}^N \left\{ \left[ \frac{1}{2}m_j c_j^2 + e_{Rj} + e_{Vj} \right]_i - \left[ \frac{1}{2}m_j c_j^2 + e_{Rj} + e_{Vj} \right]_r \right\} \quad (5.10)$$

where  $N$  is the number of molecules colliding with the gap surface by unit time and unit area,  $m$  is the mass of molecules,  $c$  is the velocity of the molecules,  $e_R$  and  $e_V$  stand for the rotational and vibrational energies, respectively. Subscripts  $i$  and  $r$  refer to incident and reflect molecules.

The influence of the altitude, the nose radius, and the gap  $L/H$  ratio on the heat transfer coefficient  $C_h$  along surfaces  $S1$  and  $S5$  are demonstrated in Fig. 5.22. Again, in this set of plots, filled and empty symbols stand for results on surface  $S1$  and  $S5$ , respectively. The left-column plots refer to the distribution of the heat transfer coefficient for an altitude of 100 km, while the right-column plots correspond to the distribution on the surfaces for an altitude of 80 km. in addition, top-, middle-, and bottom-row plots correspond to results for nose radius of  $R$ ,  $R/2$  and  $R/4$ , respectively. For comparison purpose, the heat transfer coefficient  $C_h$  for a capsule without a gap (SANTOS, 2010) is also illustrated in this set of plots for the case with nose radius of  $R$ .

Focusing on left-column plots of Fig. 5.22, it is observed that the heat transfer coefficient is not sensitive to the gap  $L/H$  ratio investigated, excepted at the vicinity of the gap position. The heat transfer coefficient behavior to the surfaces outside the gap basically follows that for a capsule without a gap. It presents the maximum value

in the stagnation point and drops off a short distance away along the capsule surface. No upstream disturb is caused by the presence of the gap, except very close to the gap position as shown in the magnified view. As the nose radius is reduced from  $R$  to  $R/4$ , it is seen that the heat transfer coefficient  $C_h$  increases in the stagnation point. This is an expected behavior, since the capsule is changing from a blunt body to a sharp body, i.e., the capsule is becoming aerodynamically sharp.

Turning to right-column plots of Fig. 5.22, for an altitude of 80  $km$ , it is seen that the heat transfer coefficient follows the same trend as that for 100  $km$  of altitude, in the sense that, its maximum value occurs at the stagnation point and decreases away along the capsule surface. However, the maximum value of  $C_h$  for 80  $km$  is smaller than that for 100  $km$  of altitude. As the altitude decreases, the freestream density increases, and the high density layer adjacent to the capsule surface acts as a shield for the molecules oncoming from the freestream. As a result, a small heat flux to the surface is observed.

In order to gain some insight into the heat transfer behavior, it becomes instructive to compare these results with those for free-molecular flow. For the free-molecular flow regime, the heat transfer coefficient is given by the following equation,

$$C_h = \frac{1}{2\sqrt{\pi}S_\infty^3}\Omega \quad (5.11)$$

$$\Omega = \left\{ \left[ S_\infty^2 + \frac{\gamma}{\gamma-1} - \frac{\gamma+1}{2(\gamma-1)} \frac{T_w}{T_\infty} \right] \left[ \exp(-\chi^2) + \sqrt{\pi}\chi(1 + \operatorname{erf}\chi) \right] - \frac{1}{2}\exp(-\chi^2) \right\}$$

According to this equation, for the Mach number correspondent to 100  $km$  of altitude, the heat transfer coefficient  $C_{hfm}$  is 0.984 and 0.194 for body slope angles of 90 and 11.4 degrees, respectively, i.e., at the stagnation point in the spherical nose and the conical afterbody. Based on Fig. 5.22, for an altitude of 100  $km$  and nose radius of  $R/4$ , the heat transfer coefficient  $C_h$  at the same stations is around 0.81 and 0.107. Therefore, as the nose radius is reduced from  $R$  to  $R/4$ , the flow around the nose approaches the free-molecular flow, as mentioned earlier.

According to Fig. 5.22, the heat transfer to the capsule is most severe at the stagnation point. Theoretical and numerical predictions of stagnation point heat transfer for continuum flow have been developed by Sibulkin (SIBULKIN, 1952), Lees (LEES,

1956), Roming (ROMIG, 1956) and Fay and Riddell (FAY; RIDDELL, 1958) to name a few. The work of Fay and Riddell (FAY; RIDDELL, 1958) is the typical reference point on aerodynamic heating. Due to their simplicity, the Fay-Riddell correlation formulas are still in use today for the thermal analysis of hypersonic vehicles. Theoretical formulations, experimental data, and semi-empirical formulas all agree in the fact that stagnation point heat transfer is inversely proportional to the square root of the nose radius of the leading edge, i.e.,  $q \propto \frac{1}{\sqrt{R}}$ . Certainly, this dependence of the heat flux with the nose curvature radius is quite apparent on the results shown in Fig. 5.22.

In the following, the sensitive of changes in the altitude, in the nose radius, and in the gap  $L/H$  ratio on the heat transfer coefficient to the surfaces inside the gap is displayed in Figs 5.23, 5.24 and 5.25 for surfaces  $S2$ ,  $S3$ , and  $S4$ , respectively. In this group of plots, again the height  $\eta$  in the off-body direction is normalized by the gap height  $H$ , and the length  $\xi$  is normalized by the gap length  $L$ . Also, left-column plots refer to the distribution of the heat transfer coefficient for an altitude of 100 km, while the right-column plots correspond to the distribution on the surfaces for an altitude of 80 km. Furthermore, top-, middle-, and bottom-row plots correspond to results for nose radius of  $R$ ,  $R/2$  and  $R/4$ , respectively.

On examining the left-column plots in Fig. 5.23, for the backward face, surface  $S2$ , it is noticed the heat transfer coefficient is basically constant over the entire surface for the range of the gap  $L/H$  ratio and nose radius investigated. In addition, the heat transfer coefficient  $C_h$  is two order of magnitude smaller than that observed along surface  $S1$ . As discussed earlier, this behavior is related to the recirculation region inside the gaps. As a result, the flow experiences a expansion at the vicinity of surface  $S2$  and a compression at the vicinity of surface  $S4$ .

As the altitude decreases from 100 km to 80 km, right-column plots, a different behavior is observed in the heat transfer coefficient as the gap  $L/H$  ratio change from 1 to 1/4. Basically, the heat transfer coefficient increases from the top to the bottom of the surface. It is also observed that the heat transfer coefficient decreases with decreasing the nose radius, for an altitude of 80 km. This is explained by the fact that the number flux to this surface decreases with decreasing the nose radius. This behavior, associated to molecules with low velocities inside the gap contributes to low heat transfer to the surface.

Along the gap floor, surface  $S3$ , Fig. 5.24, the heat transfer coefficient basically presents, for the same altitude, a similar behavior for the nose radius and gap  $L/H$

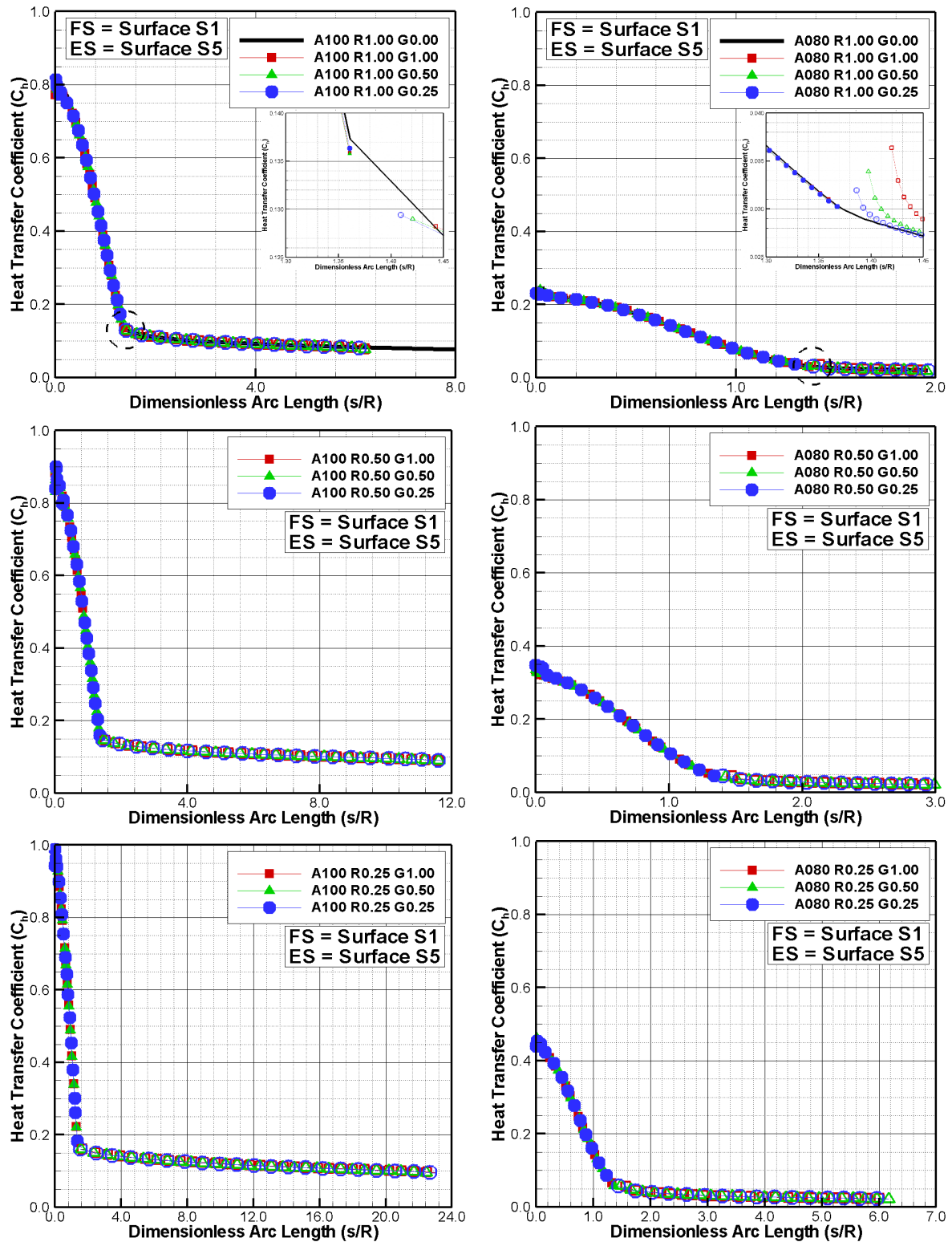


Figure 5.22 - Heat transfer coefficient ( $C_h$ ) distribution along surfaces  $S1$  and  $S5$  as a function of the dimensionless arc length  $s/R$  parameterized by the altitude, nose radius, and the gap  $L/H$  ratio.

ratio range investigated. In general, the heat transfer coefficient slightly increases from one corner to another along the bottom surface. This behavior is directly related to the flux of molecules to the bottom surface, as shown in Fig. 5.20.

Afterwards, along the forward face, surface  $S4$ , Fig. 5.25, the heat transfer coefficient basically increases from the corner, at the bottom surface, up to the top of the gap. This is an expected behavior in the sense that it is directly related to the flow recirculation inside the gaps, as pointed out earlier. Due to the clockwise flow recirculation, at the vicinity of the surface  $S4$ , density is higher than that close to surfaces  $S2$  and  $S3$ . Therefore, a larger flux of molecules colliding to this surface is expected.

In order to account for the gap effects, it is instructive to examine the differences in the heat transfer coefficient between a capsule without a gap and a capsule with a gap. At the section corresponding to the sphere/cone junction for a capsule without a gap, the heat transfer coefficient  $C_h$  is around 0.130 and 0.028 for 100  $km$  and 80  $km$  of altitude, respectively, and nose radius of  $R$ . On the other hand, the maximum values for the heat transfer coefficient inside the gap, on surface  $S4$ , are around 0.40 and 0.08 for 100  $km$  and 80  $km$  of altitude, respectively. Therefore, these values correspond approximately to 3.07 and 2.86 times, respectively, larger than those for a capsule without a gap. As a result, in a capsule project, where the presence of a gap is imperative, the heat transfer coefficient inside the gap can not be neglected.

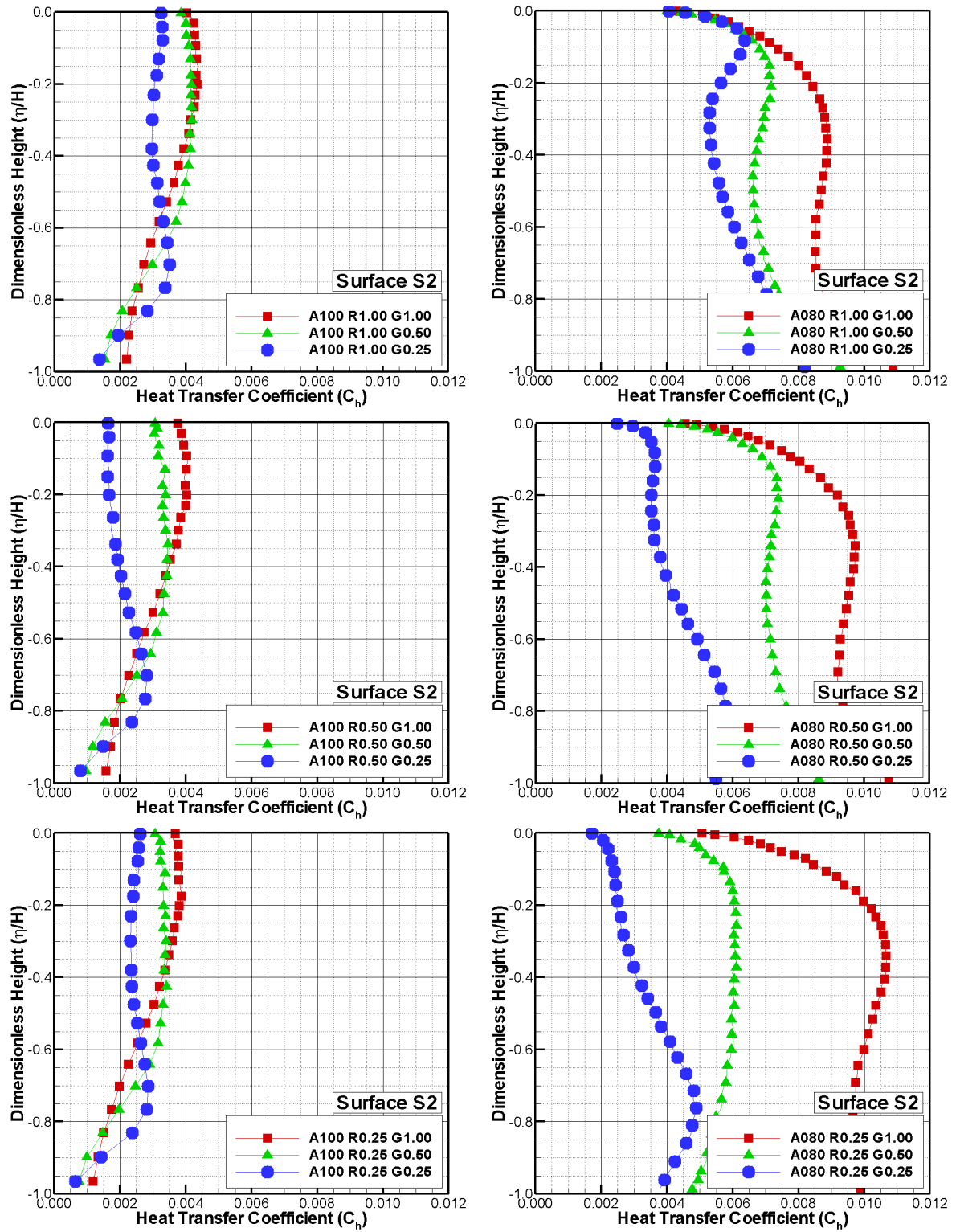


Figure 5.23 - Heat transfer coefficient ( $C_h$ ) distribution along surface  $S_2$  as a function of the dimensionless height  $\eta/H$  parameterized by the altitude, nose radius, and the gap  $L/H$  ratio.

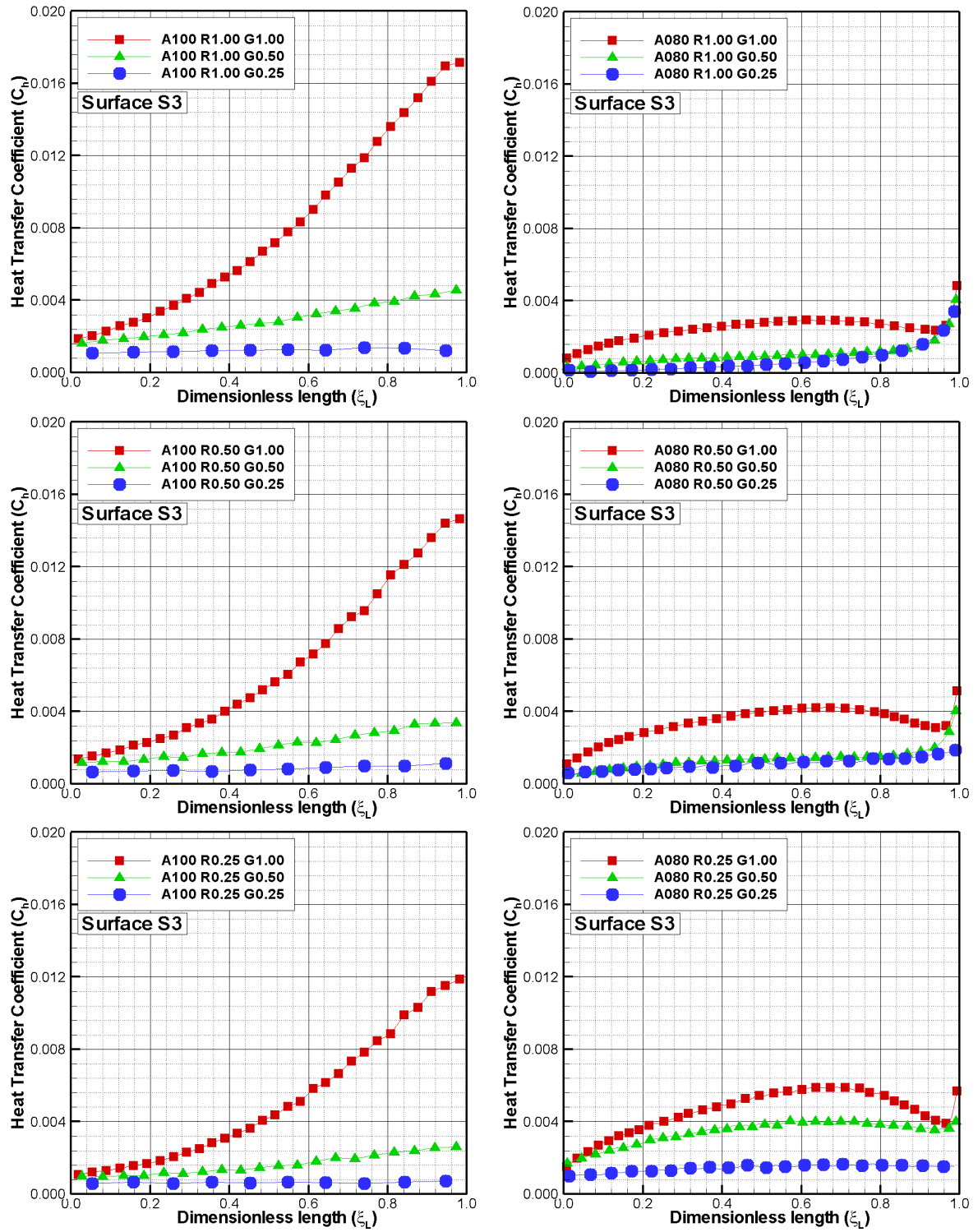


Figure 5.24 - Heat transfer coefficient ( $C_h$ ) distribution along surface  $S3$  as a function of the dimensionless length  $\xi_L$  parameterized by the altitude, nose radius, and the gap  $L/H$  ratio.

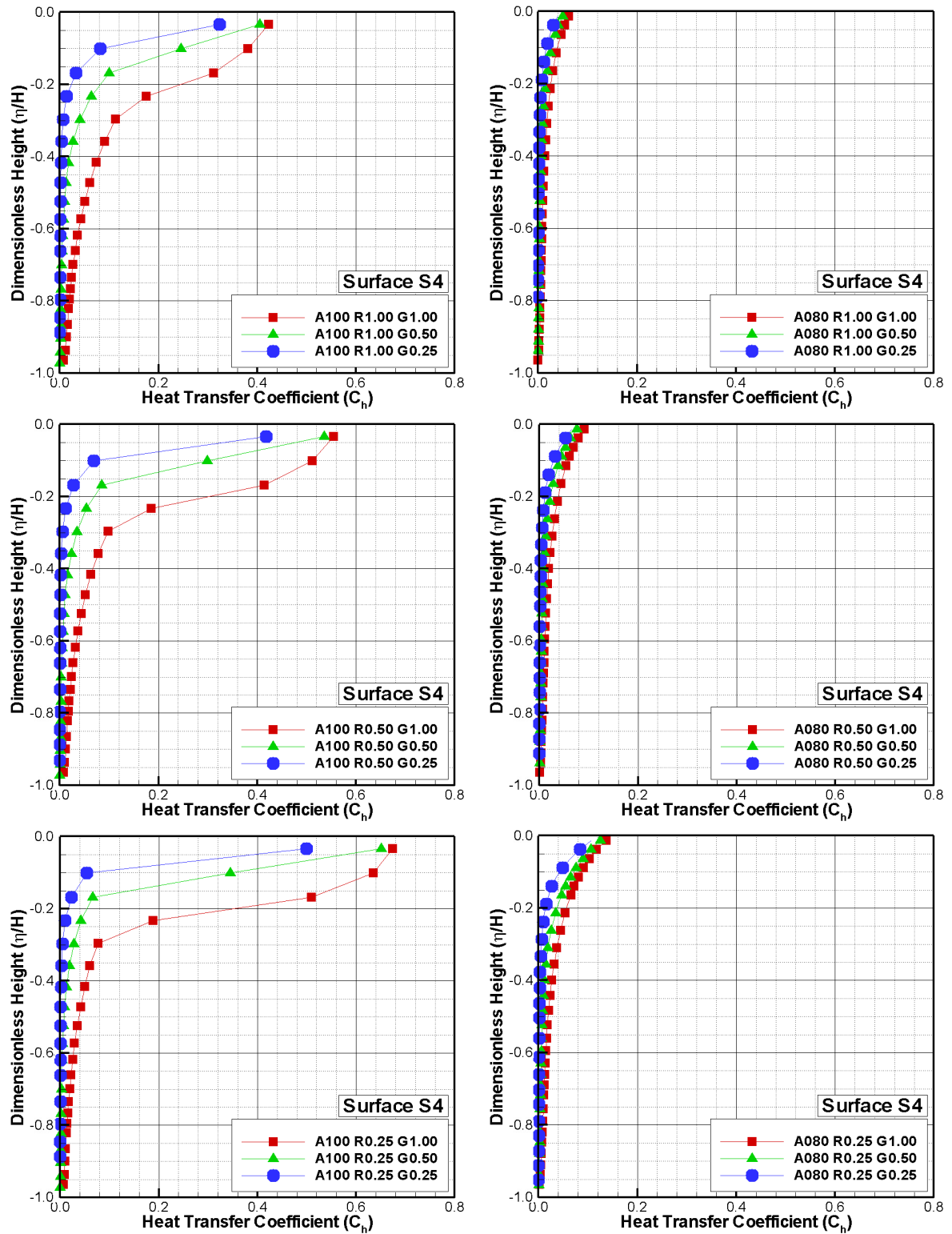


Figure 5.25 - Heat transfer coefficient ( $C_h$ ) distribution along surface  $S_4$  as a function of the dimensionless height  $\eta/H$  parameterized by the altitude, nose radius, and the gap  $L/H$  ratio.

### 5.2.3 Pressure Coefficient

The pressure coefficient  $C_p$  is defined as follows,

$$C_p = \frac{p_w - p_\infty}{\frac{1}{2}\rho_\infty U_\infty^2} \quad (5.12)$$

where the pressure  $P_w$  on the gap surface is calculated by the sum of the normal momentum fluxes of both incident and reflected molecules at each time step by the following expression,

$$p_w = p_i - p_r = \frac{F_N}{A\Delta t} \sum_{j=1}^N \{[(mv)_j]_i - [(mv)_j]_r\} \quad (5.13)$$

where  $v$  is the velocity component of the molecule  $j$  in the surface normal direction.

The effect of the altitude, the nose radius, and the gap  $L/H$  ratio on the pressure coefficient  $C_p$  along surfaces  $S1$  and  $S5$  are exhibited in Fig. 5.26. As defined earlier, in this group of plots, filled and empty symbols correspond to pressure coefficient on surface  $S1$  and  $S5$ , respectively. The left-column plots stand for the distribution of pressure coefficient for an altitude of 100 km, while the right-column plots stand for the distribution on the surfaces for an altitude of 80 km. In addition, top-, middle-, and bottom-row plots refer to results for nose radius of  $R$ ,  $R/2$  and  $R/4$ , respectively. As a matter of comparison, the pressure coefficient  $C_p$  for a capsule with nose radius of  $R$  without a gap (SANTOS, 2010) is also demonstrated in this group of plots.

According to Fig. 5.26, it is clearly observed that the pressure coefficient  $C_p$  acting on the capsule surface follows the same trend as that presented by the number flux, Fig. 5.18, in the sense that  $C_p$  is a maximum in the stagnation region. After that,  $C_p$  drastically decreases up to the sphere/cone junction. Along the cone surface, surface  $S5$ , the pressure coefficient  $C_p$  is basically constant, with values one order of magnitude lower than those attained in the stagnation point. Moreover, as the nose radius is reduced from  $R$  to  $R/4$ , it is also observed that the pressure coefficient  $C_p$  increases in the stagnation point, a similar behavior observed for the heat transfer coefficient. As mentioned earlier, the reason for that is because the capsule is changing from a blunt body to a sharp body, i.e., the capsule is becoming aerodynamically sharp with decreasing the nose radius  $R$ .

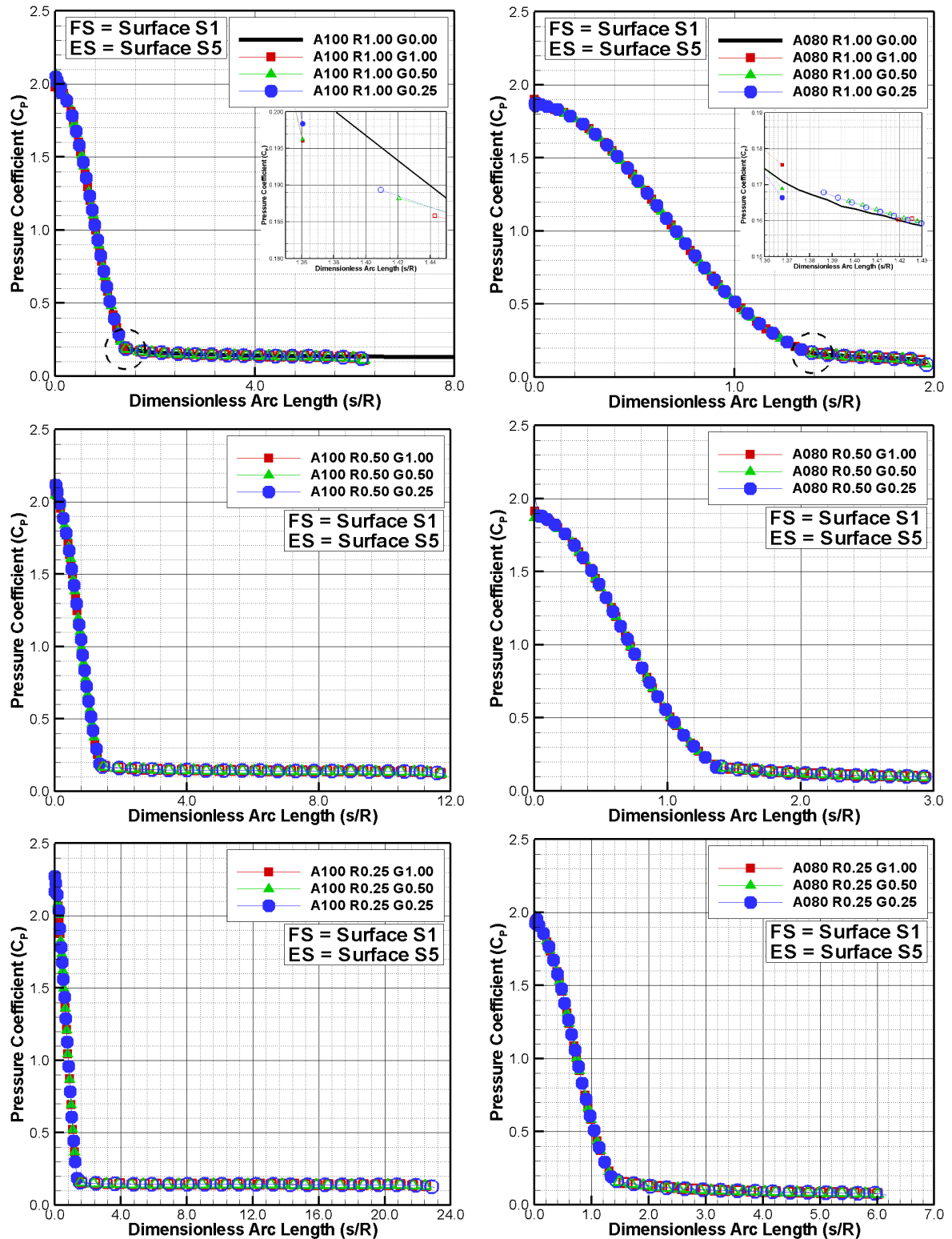


Figure 5.26 - Pressure coefficient ( $C_p$ ) distribution along surfaces  $S1$  and  $S5$  as a function of the dimensionless arc length  $s/R$  parameterized by the altitude, nose radius, and the gap  $L/H$  ratio.

Still referring to Fig. 5.26, it is noticed that the pressure coefficient preserve the same behavior as the altitude decreases from 100 *km* to 80 *km*, since the pressure coefficient for 80 *km* of altitude follows the same trend as that for 100 *km* of altitude, in the sense that, its maximum value occurs at the stagnation point and decreases away along the capsule surface. However, the maximum value of  $C_p$  for 80 *km* is smaller than that for 100 *km* of altitude for the corresponding nose radius. As the altitude decreases, the freestream density increases, and the high density layer adjacent to the capsule surface acts as a shield for the molecules oncoming from the freestream. As a result, a small pressure level to the surface is observed.

In order to bring out the essential features of the pressure coefficient  $C_p$ , it becomes instructive to compare DSMC results for  $C_p$  with those predicted by the Newtonian theory and by free-molecular flow. According to the Newtonian concept, the air flowing around a body is undisturbed by the presence of the body until it strikes the solid surface, at which time the air loses the component of momentum normal do the surface. The Newtonian theory takes into account only for the directed movement of the molecules not to the random movement of the molecules. It is important to recall that, in a hypersonic flow, the directed movement of the molecules is much larger than the random movement. The pressure coefficient predicted by the Newtonian theory is given by the following equation:

$$C_p = 2\sin^2\theta \quad (5.14)$$

where  $\theta$  is the slope angle along the body surface.

For comparison purpose, the pressure coefficient predicted by the Newtonian theory is 2.0 and 0.078 at surface slope angles of 90 and 11.4 degrees, which correspond to the stagnation point and the cone afterbody, respectively. For 100 *km* of altitude, Fig. 5.26, it is observed that DSMC results for pressure coefficient is very close to these values.

For the free-molecular flow regime, the pressure coefficient is given by the following equation,

$$C_{pfm} = \frac{1}{S_\infty^2} \left\{ \left[ \frac{\chi}{\sqrt{\pi}} + \frac{1}{2} \left( \frac{T_w}{T_\infty} \right)^{0.5} \right] \exp(-\chi^2) + \left[ \frac{1}{2} + \chi^2 + \frac{1}{2} \left( \frac{T_w}{T_\infty} \right)^{0.5} \sqrt{\pi} \chi \right] \left[ 1 + \operatorname{erf} \chi \right] - 1 \right\}$$

Based on this equation, for the Mach number correspondent to 100 km of altitude, the pressure coefficient  $C_{p_{fm}}$  is 2.15 and 0.108 for body slope angles of 90 and 11.4 degrees, respectively, i.e., at the stagnation point in the spherical nose and the conical afterbody. Based on Fig. 5.26, it is noticed that, as the nose radius is reduced from  $R$  to  $R/4$ , the flow around the nose approaches the free-molecular flow, as observed earlier.

In the results that follow, the implication of changes in the altitude, in the nose radius, and in the gap  $L/H$  ratio on the pressure coefficient to the surfaces inside the gap is illustrated in Figs. 5.27, 5.28, and 5.29, for surfaces  $S2$ ,  $S3$ , and  $S4$ , respectively. In this set of plots, again left-column plots correspond to the distribution of the pressure coefficient for an altitude of 100 km, while the right-column plots refer to the distribution on the surfaces for an altitude of 80 km. In addition, top-, middle-, and bottom-row plots correspond to results for nose radius of  $R$ ,  $R/2$  and  $R/4$ , respectively.

By looking at the left-column plots in Fig. 5.27 closely and carefully, surface  $S2$ , it is noted the pressure coefficient basically presents a low value at the top of the gap surface and increases along the surface up to the bottom with decreasing the gap  $L/H$  ratio, for the range of the gap  $L/H$  ratio and nose radius investigated. It is also noted that the pressure coefficient  $C_p$  is two orders of magnitude smaller than that observed at the stagnation point in the capsule nose. In addition, it is one order of magnitude smaller than that observed in a capsule without a gap at the same station. Certainly, this low values for the pressure coefficient is because the flow experiences a expansion at the vicinity of surface  $S2$  and a compression at the vicinity of surface  $S4$ .

As the altitude decreases from 100 km to 80 km, right-column plots, a similar behavior is observed in the pressure coefficient as the gap  $L/H$  ratio change from 1 to 1/4. Basically, the pressure coefficient increases from the top to the bottom of the surface. It is also observed that the pressure coefficient decreases with decreasing the nose radius, for an altitude of 80 km. The reason for that is related to the fact that the number flux to this surface decreases with decreasing the nose radius. This behavior, associated to molecules with low velocities inside the gap contributes to low wall pressure to the surface.

Along the gap floor, surface  $S3$ , Fig. 5.28, the pressure coefficient basically presents, for the same altitude, a similar behavior for the nose radius and gap  $L/H$  ratio range investigated. In general, the pressure coefficient increases from one corner to

another along the bottom surface. This behavior is directly related to the flux of molecules to the bottom surface, as shown in Fig. 5.20.

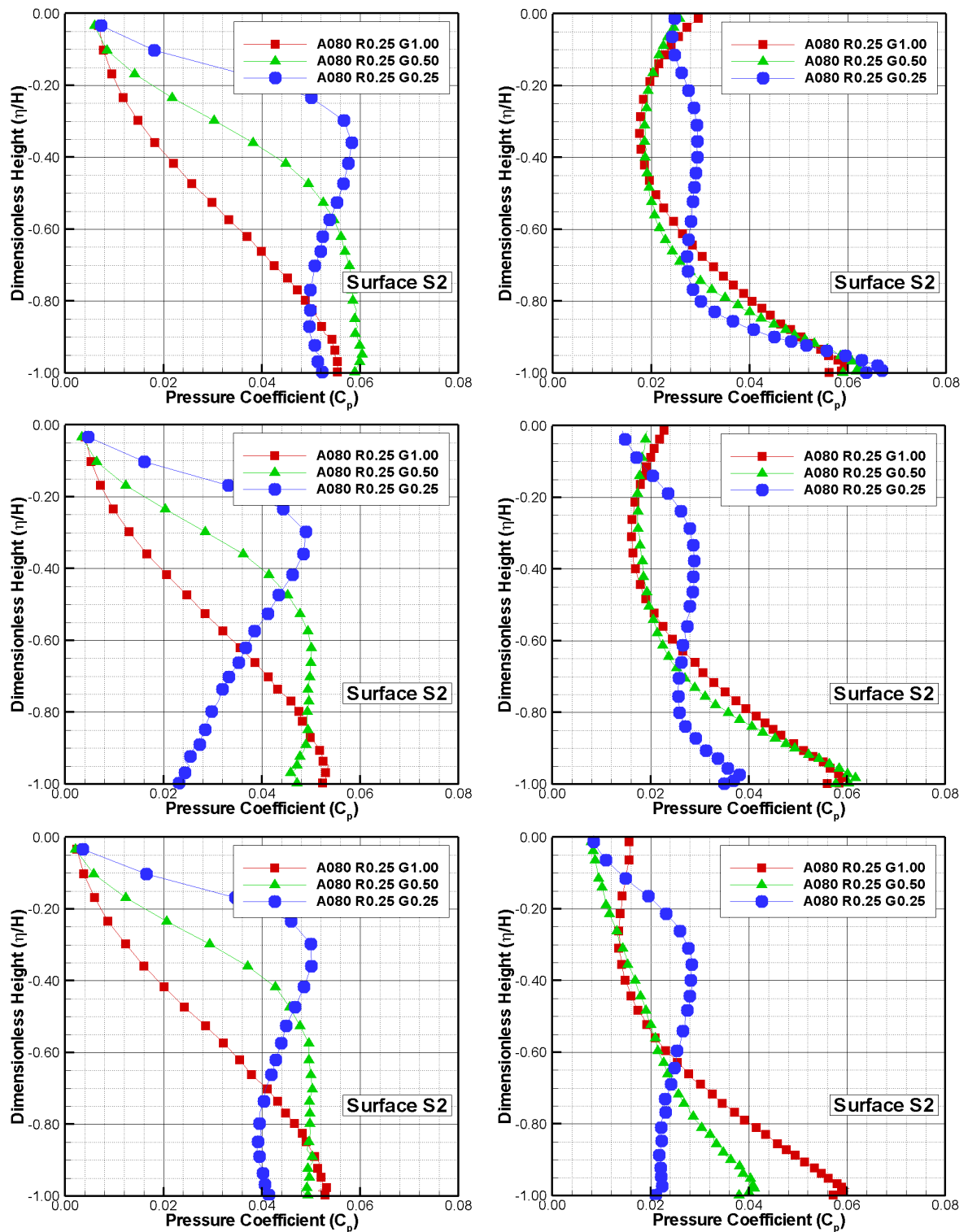


Figure 5.27 - Pressure coefficient ( $C_p$ ) distribution along surface  $S2$  as a function of the dimensionless height  $\eta/H$  parameterized by the altitude, nose radius, and the gap  $L/H$  ratio.

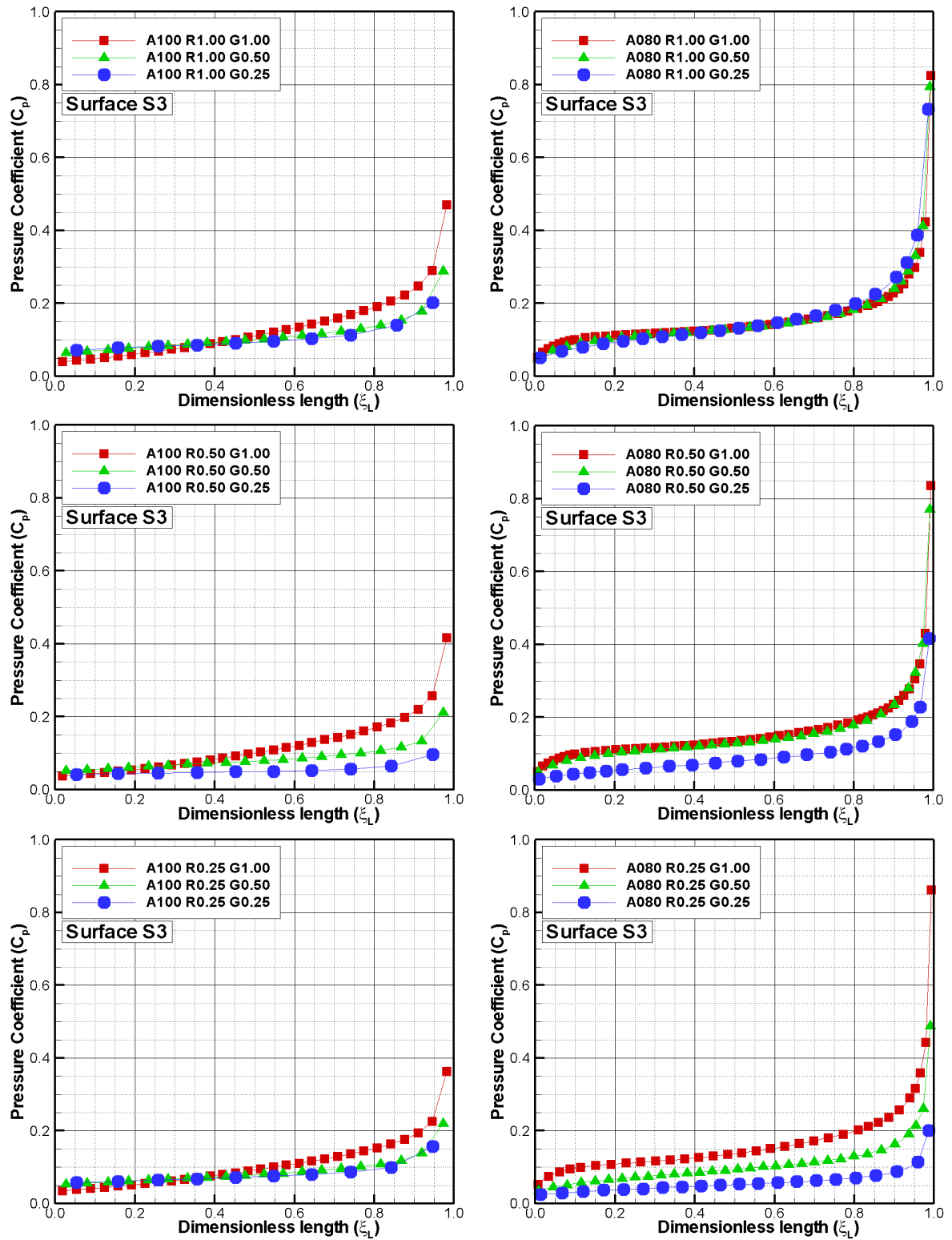


Figure 5.28 - Pressure coefficient ( $C_p$ ) distribution along surface  $S_3$  as a function of the dimensionless length  $\xi_L$  parameterized by the altitude, nose radius, and the gap  $L/H$  ratio.

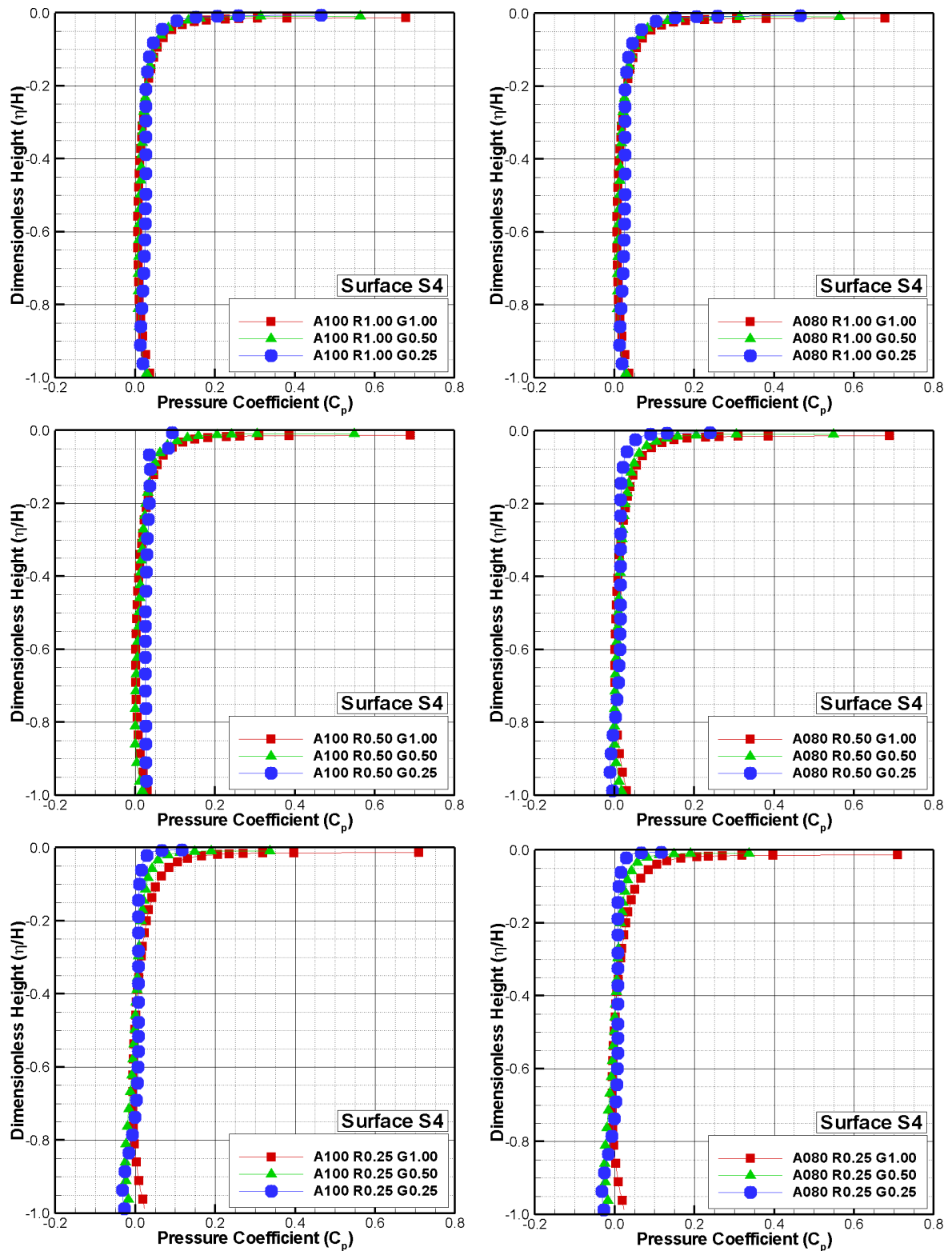


Figure 5.29 - Pressure coefficient ( $C_p$ ) distribution along surface  $S_4$  as a function of the dimensionless height  $\eta/H$  parameterized by the altitude, nose radius, and the gap  $L/H$  ratio.

### 5.2.4 Skin Friction Coefficient

The skin friction coefficient  $C_f$  is defined as follows,

$$C_f = \frac{\tau_w}{\frac{1}{2}\rho_\infty U_\infty^2} \quad (5.15)$$

where  $\tau_w$  is the shear stress on the body surface. The shear stress  $\tau_w$  is calculated by the sum of the tangential momentum fluxes of both incident and reflected molecules impinging on the surface at each time step by following expression,

$$\tau_w = \tau_i - \tau_r = \frac{F_N}{A\Delta t} \sum_{j=1}^N \{[(mu)_j]_i - [(mu)_j]_r\} \quad (5.16)$$

where  $u$  is the velocity component of the molecule  $j$  in the surface tangential direction.

It is important to note that for the special case of diffuse reflection, the gas-surface interaction model adopted in present work, the reflected molecules have a tangential moment equal to zero, since the molecules essentially lose, on average, their tangential velocity components. In this fashion, the net tangential momentum flux is defined as follows,

$$\tau_w = \tau_i = \frac{1}{A\Delta t} \sum_{j=1}^N \{[(mu)_j]_i\} \quad (5.17)$$

The dependence of the skin friction coefficient  $C_f$  along surfaces  $S1$  and  $S5$  due to changes in the altitude, nose radius, and in the gap  $L/H$  ratio is demonstrated in Fig. 5.30. As defined earlier, in this set of plots, the left-column plots stand for the distribution of the skin friction coefficient for an altitude of 100 km, while the right-column plots stand for the distribution on the surfaces for an altitude of 80 km. Furthermore, top-, middle-, and bottom-row plots refer to results for nose radius of  $R$ ,  $R/2$  and  $R/4$ , respectively. For comparison purpose, the skin friction coefficient  $C_f$  for a capsule with nose radius of  $R$  without a gap (SANTOS, 2010) is also demonstrated in this set of plots.

According to Fig. 5.30, the skin friction coefficient presents a similar behavior for the range of altitude, nose radius and gap  $L/H$  ratio investigated. Along the capsule

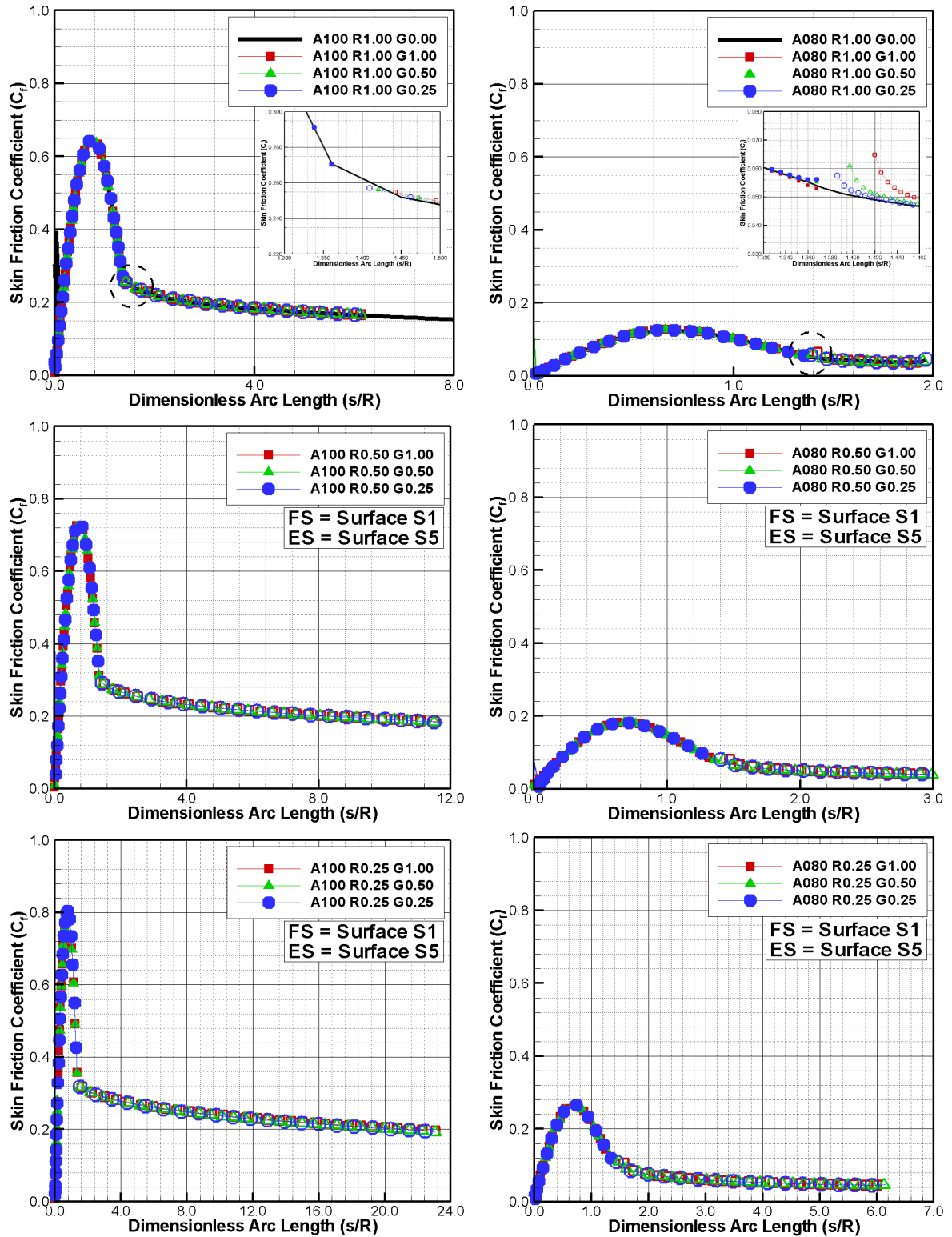


Figure 5.30 - Skin friction coefficient ( $C_f$ ) distribution along surfaces  $S1$  and  $S5$  as a function of the dimensionless arc length  $s/R$  parameterized by the altitude, nose radius, and the gap  $L/H$  ratio.

surface,  $C_f$  starts from zero at the stagnation point, increases to a maximum value located on the spherical surface, and decreases downstream along this surface up to the junction point, i.e., surface-S1/surface-S2 junction. It is seen that as the altitude is reduced from 100 km to 80 km, the peak value on the spherical surface decreases significantly. As pointed out earlier, the reason for that is related to either the shielding or enhanced effects. By reducing the altitude, the freestream mean free path decreases, the freestream density increases, and the high density layer adjacent to the capsule surface acts as a shield for the molecules oncoming from the freestream. As a result, a reduction in the net moment flux to the surface is observed.

Still referring to Fig. 5.30, it is also seen that the changes in the gap  $L/H$  ratio have a small effect on the skin friction coefficient. As shown in the magnified view, this effect is more pronounced as the altitude decreases from 100 km to 80 km, i.e., as the capsule enters deeper into the earth atmosphere. In contrast, as the nose radius decreases from  $R$  to  $R/4$ , the peak value on the spherical surface increases significantly. As explained earlier, the reason for that is related to changes in the body shape, i.e., the nose is becoming aerodynamically sharp one.

For the free-molecular flow regime, the the skin friction coefficient is given by the following equation,

$$C_{ffm} = \frac{\cos\chi}{\sqrt{\pi}S_\infty} [\exp(-\chi^2) + \sqrt{\pi}\chi(1 + \operatorname{erf}\chi)] \quad (5.18)$$

Based on this equation, for the Mach number correspondent to 100 km of altitude, the peak value for the skin friction coefficient,  $C_{ffm} = 1.0$ , is located on the spherical surface at a station corresponding to a body slope angle of 45 degrees. Based on Fig. 5.30, for the  $L/H=1$  case, the peak values for  $C_f$  are 0.65, 0.73, and 0.81, located at a station corresponding to 46.7, 46.4 and 44.6 degrees for nose radius of  $R$ ,  $R/2$  and  $R/4$ , respectively. Therefore, as the nose radius is reduced from  $R$  to  $R/4$ , the flow around the nose approaches the free-molecular flow, as observed earlier.

In the following, the consequence of changes in the altitude, in the nose radius, and in the gap  $L/H$  ratio on the skin friction coefficient to the surfaces inside the gap is illustrated in Figs. 5.31, 5.32, and 5.33, for surfaces  $S2$ ,  $S3$ , and  $S4$ , respectively.

Referring to the left-column plots in Fig. 5.32, for the backward face, surface  $S3$ , it is noticed the skin friction coefficient is negative along the entire surface for the range of

the gap  $L/H$  ratio and nose radius investigated. It means that the flow velocity is in the upward direction at the vicinity of this surface, a consequence of the recirculation region inside the gap. In addition, similar to the pressure coefficient, the skin friction coefficient is one order of magnitude smaller than that observed along surface  $S1$ .

As the altitude decreases from 100 km to 80 km, right-column plots, a different behavior is noticed in the skin friction coefficient as the gap  $L/H$  ratio change from 1 to 1/4. Basically, the skin friction coefficient increases from the top up to the middle of the surface and decreases from this position up to the bottom of the surface. It is also notice that the skin friction coefficient decreases with decreasing the nose radius, for an altitude of 80 km, similar to the heat transfer coefficient behavior. This is explained by the fact that the number flux to this surface decreases with decreasing the nose radius. This behavior, associated to molecules with low velocities inside the gap contributes to low tangential momentum flux to the surface.

Along the gap floor, surface  $S3$ , Figure 5.32, the skin friction coefficient basically presents a similar behavior for the range of the gap  $L/H$  ratio and nose radius investigated, i.e.,  $C_f$  is basically constant along the surface and significantly decreases close to the surface- $S3$ /surface- $S4$  junction. This behavior is directly related to the flux of molecules to the bottom surface, as shown in Fig. 5.20.

In the following, along the forward face, surface  $S4$ , Fig. 5.33, the skin friction coefficient basically increases from the corner, at the bottom surface, up to the top of the gap. Analogous to the heat transfer coefficient, this is an expected behavior in the sense that it is directly related to the flow recirculation inside the gaps, as pointed out earlier. Due to the clockwise flow recirculation, at the vicinity of the surface  $S4$ , density is higher than that close to surfaces  $S2$  and  $S3$ . Therefore, a larger flux of molecules colliding to this surface is expected. As a result, the momentum flux increases to this surface.

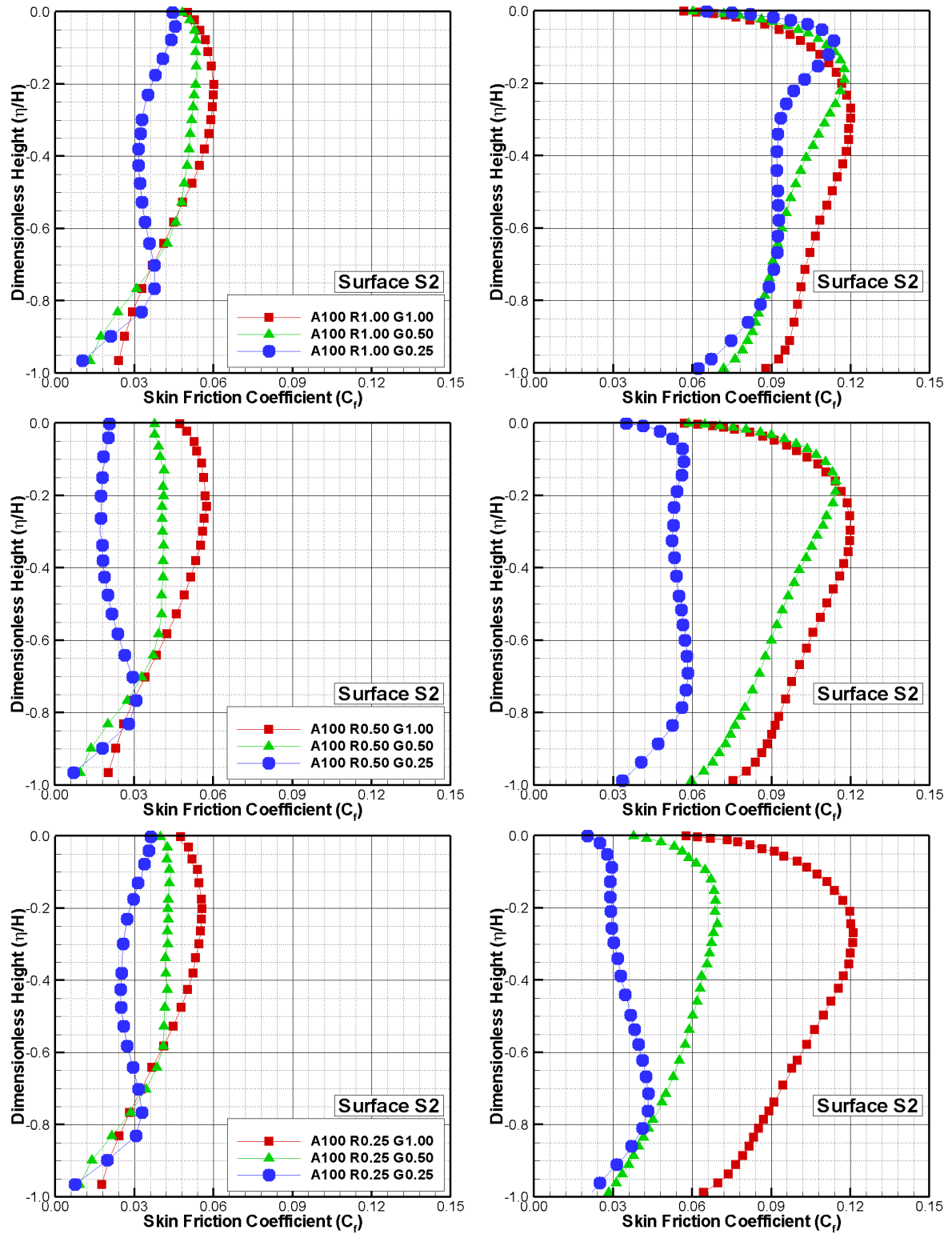


Figure 5.31 - Skin friction coefficient ( $C_f$ ) distribution along surface  $S2$  as a function of the dimensionless height  $\eta/H$  parameterized by the altitude, nose radius, and the gap  $L/H$  ratio.

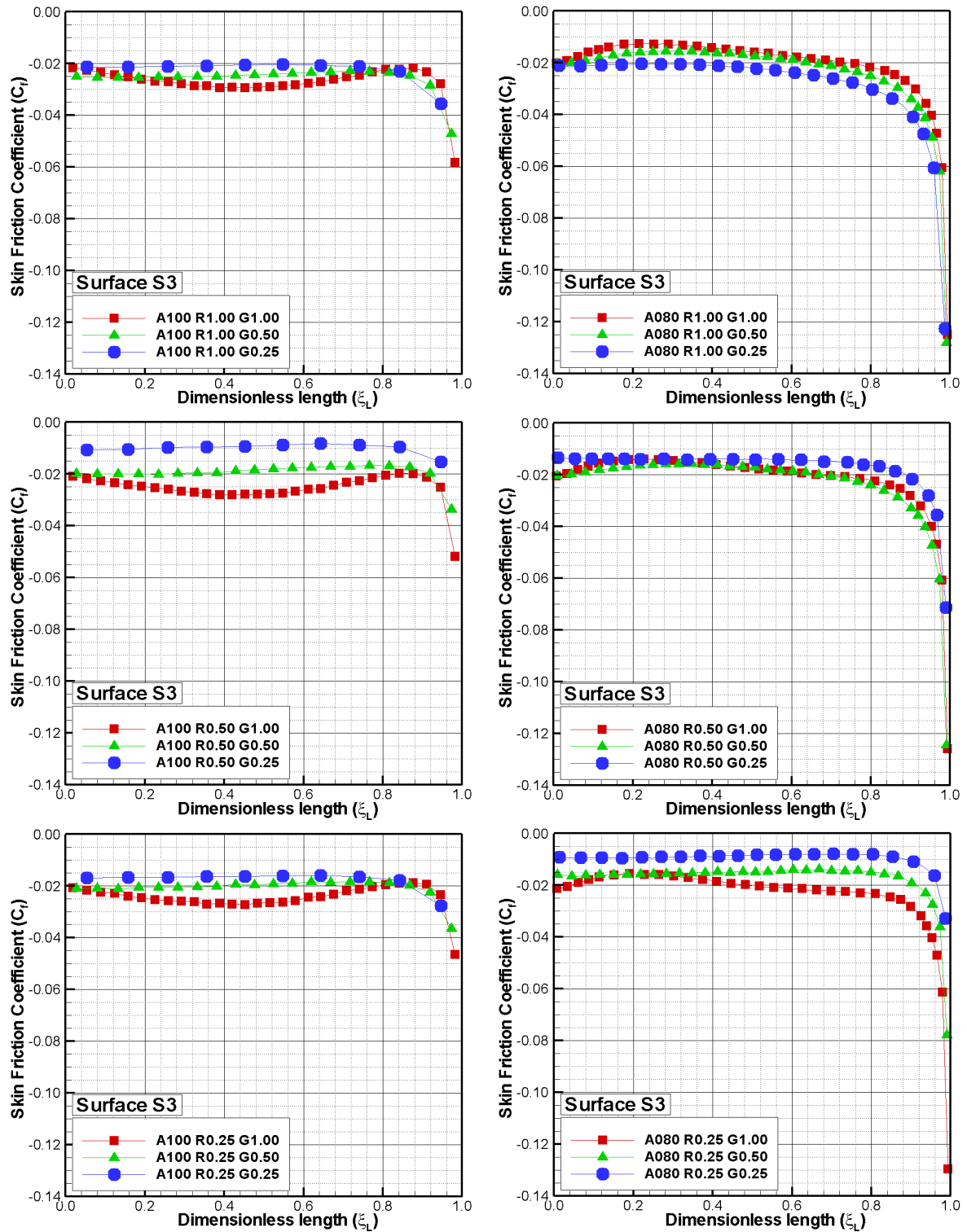


Figure 5.32 - Skin friction coefficient ( $C_f$ ) distribution along surface  $S3$  as a function of the dimensionless length  $\xi_L$  parameterized by the altitude, nose radius, and the gap  $L/H$  ratio.

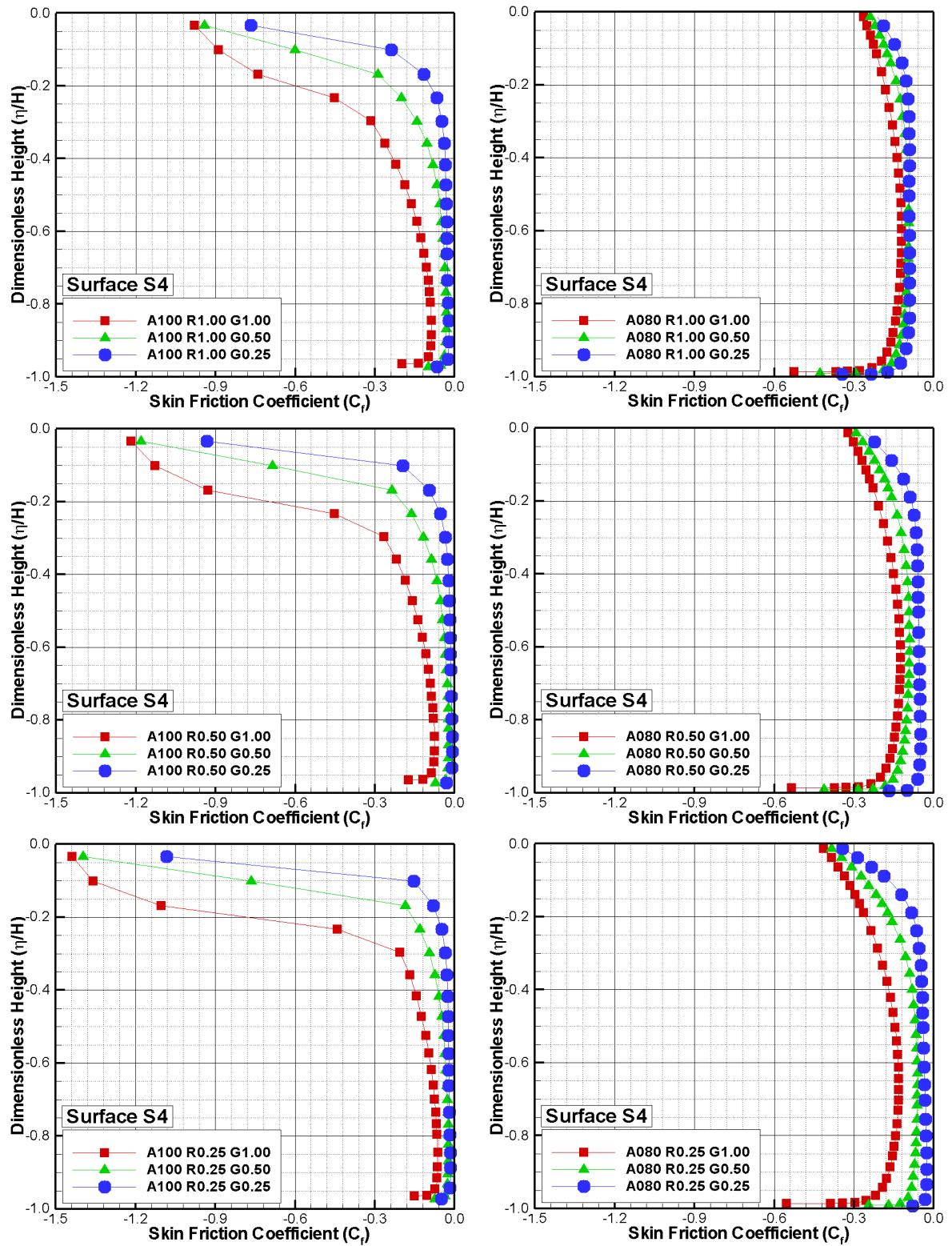


Figure 5.33 - Skin friction coefficient ( $C_f$ ) distribution along surface  $S_4$  as a function of the dimensionless height  $\eta/H$  parameterized by the altitude, nose radius, and the gap  $L/H$  ratio.

### 5.2.5 Drag Coefficient

The total drag coefficient  $C_d$  is defined as being,

$$C_d = \frac{F_d}{\frac{1}{2}\rho_\infty U_\infty^2 A} \quad (5.19)$$

where  $F_d$  is the resultant force acting on the capsule surface and  $A$  is a reference area.

The drag force  $F_d$  is obtained by the integration of the wall pressure  $p_w$  and shear stress  $\tau_w$  distributions along the capsule surface. In the present account, the integration was considered from the stagnation point to the section that corresponds to the total length  $l$ , as shown in Fig. 3.1(a). As a result, the reference area  $A$  was considered as the frontal area at this section, which is different for each nose radius  $R$  investigated. In addition, no base pressure effects were taken into account on the calculations.

Changes in the total drag coefficient is demonstrated in Tab. 5.1. Analyzing the results of the Tab. 5.1 it is possible to verify that the drag coefficient is directly related to the altitude, presenting higher coefficients as the it decreases. In addition, it is noted that the wall pressure  $p_w$  have more relevance than the shear stress  $\tau_w$  on the drag coefficient, however, as the nose radius  $R$  becomes smaller, i.e., the vehicle becomes more aerodynamic, smaller are those differences.

Finally, it was noted that the gap  $L/H$  ratio for the cases investigated has little influence on the total drag coefficient.

Table 5.1 - Total Drag Coefficient ( $C_d$ ) for all vehicles cases investigated.

Alt. ( $A$ )	Nose Ratio ( $R$ )	Gap Ratio ( $G$ )	$(C_d)_p$	$(C_d)_f$	$C_d$
100	1.00	1.00	0.033	0.019	0.052
100	1.00	0.50	0.033	0.019	0.052
100	1.00	0.25	0.033	0.019	0.052
100	0.50	1.00	0.010	0.007	0.017
100	0.50	0.50	0.010	0.007	0.017
100	0.50	0.25	0.010	0.007	0.017
100	0.25	1.00	0.011	0.004	0.015
100	0.25	0.50	0.012	0.004	0.016
100	0.25	0.25	0.012	0.004	0.016
090	1.00	1.00	0.032	0.010	0.042
090	1.00	0.50	0.032	0.010	0.042
090	1.00	0.25	0.034	0.010	0.044
090	0.50	1.00	0.011	0.009	0.020
090	0.50	0.50	0.011	0.010	0.021
090	0.50	0.25	0.011	0.010	0.021
090	0.25	1.00	0.013	0.005	0.018
090	0.25	0.50	0.013	0.005	0.018
090	0.25	0.25	0.013	0.005	0.018
080	1.00	1.00	0.149	0.022	0.171
080	1.00	0.50	0.149	0.022	0.171
080	1.00	0.25	0.149	0.023	0.172
080	0.50	1.00	0.059	0.021	0.080
080	0.50	0.50	0.059	0.022	0.081
080	0.50	0.25	0.059	0.022	0.081
080	0.25	1.00	0.022	0.017	0.039
080	0.25	0.50	0.022	0.018	0.040
080	0.25	0.25	0.022	0.018	0.040

### 5.2.6 Computational and Experimental Comparison

Having completed the discussion on the aerodynamic surface properties along the capsule surface, the attention now is turned to the comparison of the results. Because of the small amount of data on SARA capsule in the literature, the present simulation data will be compared to those obtained experimentally (GRIFFITH; LEWIS, 1964), (WILKINSON; HARRINGTON, 1962), (MACHELL, 1956) with a similar geometry, i.e., a body defined by a spherical nose with a conical afterbody.

Griffith and Lewis (GRIFFITH; LEWIS, 1964) conducted experiments in the hypervelocity tunnel of the Arnold Engineering Development Center-von Karman Facility (AEDC-VKF) for a 9-degree half-angle spherically blunted cone. In addition,  $N_2$  was used as the working fluid, freestream Mach number near 19 and freestream Reynolds number between 8000 and 15000/*in*. Wilkinson and Harrington (WILKINSON; HARRINGTON, 1962) obtained experimental data from Cornell Aeronautical Laboratory (CAL) shock tunnel for a 9-degree half-angle spherically blunted cone, with air as a working fluid, freestream Mach number near 14.5 and freestream Reynolds number between 5700 and 12000/*in*. Finally, Machell (MACHELL, 1956) employed a spherical nosed cone with semi-vertex angle of 10 degrees tested in a hypersonic wind tunnel at a Mach number of 5.8, and freestream Reynolds number in the range of 0.97-2.38x10<sup>5</sup>/*in*. Main characteristics of the models for these experimental studies are tabulated in Table 5.2.

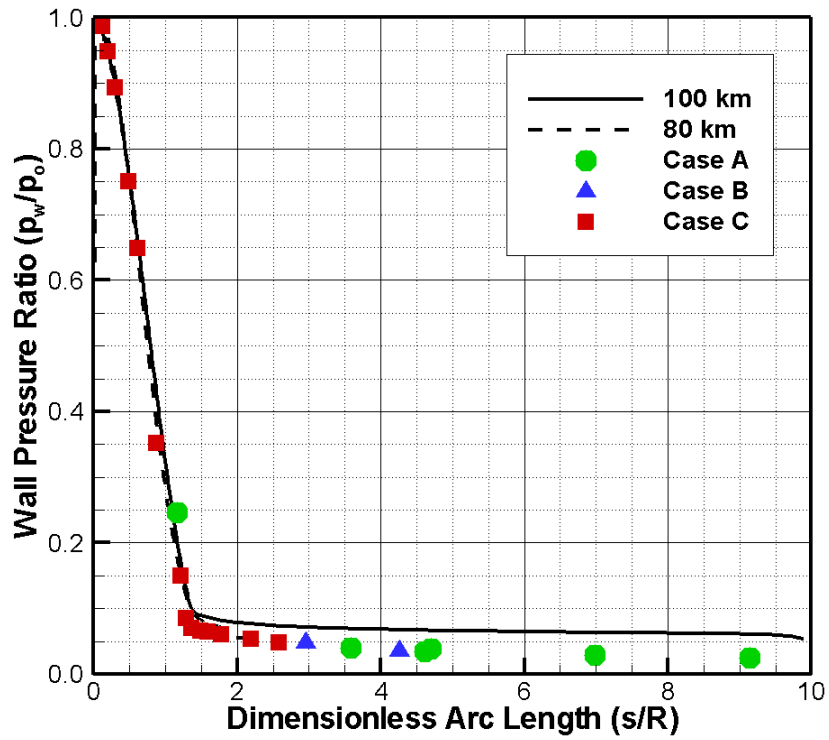
Table 5.2 - Flow and geometric conditions for the spherically blunted cone models.

Case	A	B	C
$M_\infty$	19	14.5	5.8
$Re_\infty/in$	9-15x10 <sup>3</sup>	5.7-12x10 <sup>3</sup>	1.910x10 <sup>5</sup>
$R/R_B$	0.3	0.3	0.8
$\Theta$	9	9	10

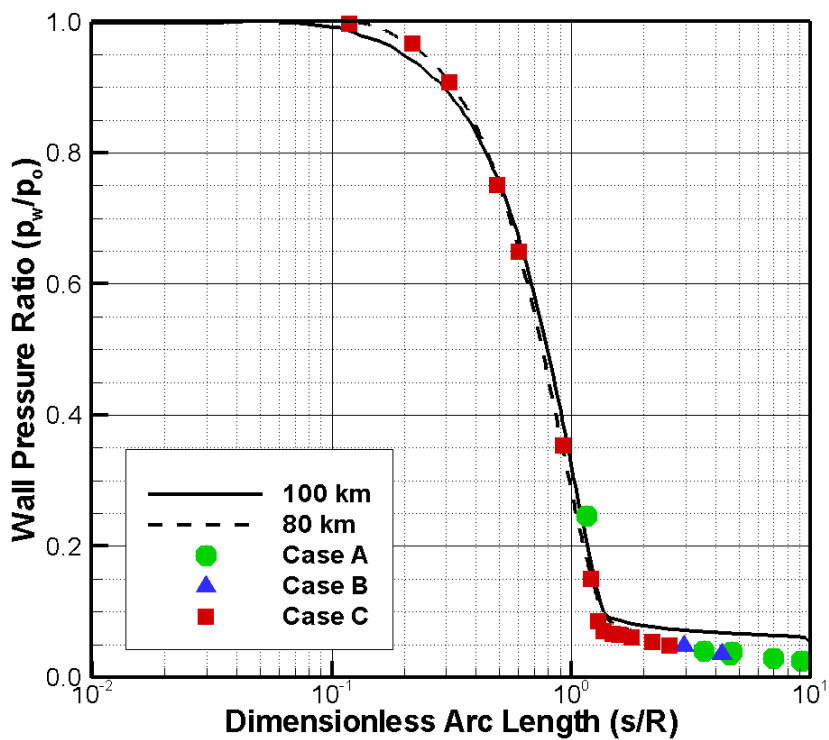
As a basis of comparison, Fig. 5.34 displays the pressure acting on the body surface from these experimental studies and from DSMC simulations. In this set of plots, the wall pressure  $p_w$  is normalized by the pressure at the stagnation point  $p_o$ , and the arc length  $s$  along the body surface is normalized by the nose radius  $R$ . In addition, the plot on the top illustrates the pressure ratio  $p_w/p_o$  distribution with a linear scale in the abscissa, while that in the bottom exhibits the same pressure ratio distribution in a logarithm scale in order to emphasize the pressure ratio behavior at the vicinity

of the stagnation point.

According to Fig. 5.34, it is clearly seen that the wall pressure ratio for the present work agreed reasonably well with that obtained experimentally. It is important to remark that the shape of the pressure distributions as described in nondimensional coordinates is independent of the spherical nose radius and of the Reynolds number over the range investigated.



(a)



(b)

Figure 5.34 - Comparison of wall pressure ratio ( $p_w/p_o$ ) distribution along the body surface in a (a) linear scale and in a (b) logarithm scale.

## 6 CONCLUSIONS

### 6.1 Concluding Remarks

Computations of a rarefied hypersonic flow over a reentry capsule, like SARA capsule, have been performed by using the Direct Simulation Monte Carlo method. The calculations provided information concerning the nature of the flowfield structure around the capsule and the aerodynamic surface properties acting on the capsule by considering a discontinuity on the surface defined by a gap. The capsule overall performance resulting from variations in the gap length-to-depth ( $L/H$ ) ratio, in the altitude, and in the nose radius were compared to that of a capsule without a gap on its surface for the idealized situation of an axisymmetric rarefied hypersonic flow. A very detailed description of the flowfield properties, such as velocity, density, pressure, and temperature, and aerodynamic surface quantities, such as number flux, heat transfer, pressure, skin friction, were presented separately outside and inside the gaps by a numerical method that properly accounts for non-equilibrium effects. The surface discontinuity impact on the capsule performance was investigated for a wide range of parameters. The gap  $L/H$  ratio was set to 1,  $1/2$ , and  $1/4$ . The altitude covered the capsule reentry trajectory for 100, 90, and 80 *km*, and finally, changes on the capsule shape considered a capsule with a nose radius of  $R$ ,  $R/2$ , and  $R/4$ . These cases covered a hypersonic flow from the free molecular flow regime to the transitional flow regime.

#### Gap $L/H$ ratio Effect

It was observed that the presence of the gap had a small effect on the primary properties, velocity, density, pressure and temperature, upstream and downstream of the gap location as compared to that for a capsule without a gap. In addition, the domain of influence along the upstream and downstream surfaces did not change with decreasing the gap  $L/H$  ratio. It was also observed that the flow structure inside the gap was characterized by a primary vortex system, with the recirculation region filling the entire gap for the range of  $L/H$  ratio investigated. The analysis showed that the gap flow topology observed here in a rarefied environment differed from that usually observed in the continuum flow regime, where the number of vortices is approximately given by the  $H/L$  ratio. Another issue that stimulated this study is related to the heat and pressure loads on the capsule surface. Peak values for the heat loads took place on the gap corner in the forward-facing surface. It was found that the heat load is three times larger than that corresponding to the same position for a capsule without a gap. A similar behavior was found for the pressure load. It

was found that the pressure load in the gap corner on the forward-facing surface is larger than that corresponding to the same position for a capsule without a gap. In this scenario, in the design of a capsule, where the presence of a gap is imperative, heat and pressure loads inside the gap can not be neglected.

#### Altitude Effect

Rarefaction effect caused considerable changes in the aerodynamic characteristics of the capsule. The stagnation point heating decreased significantly when the altitude was decreased from 100 *km* to 80 *km*. For 100 *km* of altitude, the stagnation point heating approached that predicted by the free molecular flow. In contrast, inside the gap, the heat load increased by decreasing the altitude.

#### Nose Radius Effect

It was found that changes on the nose of the capsule disturbed the flowfield around the capsule. The extent of the flowfield disturbance decreased with decreasing the nose radius since the capsule shape changed from a blunt body to an aerodynamically sharp body. For the same altitude, it was also found that the heat and pressure loads increased inside the gap by decreasing the nose radius.

## 6.2 Future Work

The present document has described an initial investigation of a high-altitude and low density flow over the capsule like the SARA capsule. Although this investigation has taken into account for a representative range of altitude, gap  $L/H$  ratio, and nose radius, a number of improvements to a realistic capsule design is still desirable. Since no database exists for such a design and since no appropriate flight data are available at such high entry velocities and conditions, the use of computational methods is essential. Since many of these issues occur in the rarefied portion of the trajectory, accurate DSMC analysis is especially important.

First on the list is to incorporate a chemical reaction model in order to examine the effects of such modeling on the predicted surface heating over the capsule surface. The shock layer around typical hypersonic reentry vehicles is characterized by a high degree of thermal and chemical non-equilibrium. Moreover, many of these flowfields results in significant surface heating as a result of chemical non-equilibrium in the shock layer. Therefore, the ability to predict these types of flowfield will be helpful in predicting thermal loads and necessary to adequate the thermal protection system.

The diffuse reflection model employed in this research assumes that the molecules are reflected equally in all directions, quite independently of their incident speed and direction. Nevertheless, as a space flight vehicle is exposed to a rarefied environment over a considerable time, a departure from the fully diffuse model is observed, resulting from the colliding molecules that clean the surface of the vehicle, which becomes gradually decontaminated. Molecules reflected from clean surfaces show lobular distribution in direction. In this scenario, incomplete surface accommodation effects might provide more insight into the sensitivity of the aerothermodynamic surface quantities to gas-surface model.

The DSMC method has been used to assess the flowfield structure and the aerodynamic surface properties by considering constant wall temperature. In a realistic design, temperature changes along the body surface. In this context, a more detailed analysis that includes the conjugate heat transfer problem seems to be challenge.



## REFERENCES

- ABE, T. Rarefied gas flow analysis by Direct Simulation Monte Carlo method in body-fitted coordinate system. **Journal of Computational Physics**, v. 83, p. 424–432, 1989. 22, 47
- \_\_\_\_\_. Generalized scheme of the no-time-counter scheme for the DSMC in rarefied gas flow analysis. **Computer Fluids**, v. 22, n. 2-3, p. 253–257, 1993. 25
- ACOSTA, L. M. C.; MORAES JR., P. Características aerodinâmicas de um veículo de reentrada atmosférica. In: INTERNATIONAL SYMPOSIUM ON SHOCK WAVES, 15th. **Proceedings...** Águas de Lindóia, São Paulo, Brasil: Rio da Janeiro: ABCMI, 1999. 1
- AKIRA, S. Introduction to practice of molecular simulation. 2011. Elsevier Inc. 18
- ALDER, B. J.; WAINWRIGHT, T. E. Studies in molecular dynamics. **Journal of Chemical and Physics**, v. 27, p. 1208–1209, 1957. 18
- \_\_\_\_\_. Molecular dynamics by electronic computers. **Transport Processes in Statistical Mechanics**, v. 27, p. 97–131, 1958. Ed. I. Prigogine, New York, Interscience. 18
- ALEXANDER, F. J.; GARCIA, A. J.; ALDER, B. J. A consistent Boltzmann algorithm. **Physical Review Letter**, v. 74, n. 26, p. 5212–5215, 1995. 18, 19
- \_\_\_\_\_. Erratum: Cell size dependence of transport coefficients in stochastic particle algorithms. **Physics of Fluids**, v. 12, n. 3, p. 731, 2000. 48
- AVERY, D. E. **Experimental aerodynamic heating to simulated space shuttle tiles in laminar and turbulent boundary layers with variable flow angles at a nominal mach number of 7**. Whashington, USA: NASA, 1985. PAPER-2307. 7, 8
- AVERY, D. E.; KERR, P. A.; WIETING, A. R. **Experimental aerodynamic heating to simulated shuttle tiles**. Whashington, USA: NASA, 1983. Paper TM-84654. 7, 8
- BAGANOFF, D.; FALLAVOLLITA, M.; MCDONALD, J. Reduction of simulation cost and error for particle simulations of rarefied flow. **Journal of Computational Physics**, v. 109, n. 1, p. 30–36, 1993. 27
- BERGEMANN, F.; BOYD, I. D. New discrete vibrational energy model for the Direct Simulation Monte Carlo method. **Rarefied gas Dynamics**, p. 174–183, 1994. 33

- BERTIN, J. J.; CUMMINGS, R. M. Critical hypersonic aerothermodynamic phenomena. **Annual Review of Fluid Mechanics**, v. 38, p. 129–157, 2006. 2, 3
- BERTIN, J. J.; GOODRICH, W. D. Aerodynamic heating for gaps in laminar and transitional boundary layers. In: AIAA AEROSPACE SCIENCES MEETING AND EXHIBIT, 18th. **Proceedings...** Pasadena, CA., USA: AIAA, 1980. 7, 8, 39
- BERTIN, J. J.; KEISNER, A. **Effect of step and/or gap tile misalignment on Shuttle transition**. Austin, TX.: NASA, 19778. NASA-CR-151833, REPT-78003. 7, 8
- BERTRAM, M. H.; WIGGS, M. M. Effect of surface distortions on the heat transfer to a wing at hypersonic speeds. **AIAA Journal**, v. 1, n. 6, p. 1313–1319, 1963. 2
- BIRD, G. A. Molecular gas dynamics. **Annual Review of Fluid Mechanics**, 1976. 18, 21, 22, 25, 26, 27
- \_\_\_\_\_. Monte Carlo simulation of gas flows. **Annual Review of Fluid Mechanics**, v. 10, p. 11–31, 1978. 19
- \_\_\_\_\_. Monte-Carlo simulation in an engineering context. **International Symposium on Rarefied Gas Dynamics**, p. 239–255, 1981. AIAA. 24
- \_\_\_\_\_. Definition of mean free path for real gases. **Physics of Fluids**, v. 26, n. 11, p. 3222–3223, 1983. 43
- \_\_\_\_\_. Low-density aerothermodynamics. **Progress in Astronautics and Aeronautics**, v. 103, 1986. ix, 15, 16
- \_\_\_\_\_. Rarefied gas dynamics: Theoretical and computational techniques: Perception of numerical method in rarefied gas dynamics. **Journal of Computational Physics**, p. 374–395, 1989. Washington D.C: Eds. E.P Muntz, D.P Weaver and D.H Campbel. 22, 25
- \_\_\_\_\_. Molecular gas dynamics and the direct simulation of gas flows. 1994. [S.l.]: Clarendon Press, Oxford. ix, 18, 21, 26, 31, 33, 34, 45, 48, 49, 50, 52, 81
- \_\_\_\_\_. Recent advances and current challenges for DSMC. **Computers and Mathematics with Applications**, v. 35, n. 1-2, p. 1–14, 1998. 22, 33
- \_\_\_\_\_. Forty years of DSMC, and now. **Rarefied Gas Dynamics**, p. 372–380, 2001. 22nd International Symposium. 34, 35

\_\_\_\_\_. Sophisticated DSMC. **Notes prepared for a short course at the DSMC07 meeting**, 2007. 27

\_\_\_\_\_. A comparison of collision energy-based and temperature-based procedures in dsmc. In: INTERNATIONAL SYMPOSIUM ON RAREFIED GAS DYNAMICS, 26th. **Proceedings...** Kyoto, Japan, 2008. p. 245–250. 33, 35, 43

\_\_\_\_\_. The DSMC method, version 1.1. 2013. ix, 18, 23

BOHON, H. L.; W., S. J.; HUNT, L. R.; WEINSTEIN, I. Performance of thermal protection systems in a mach 7 environment. **Journal of Spacecraft**, v. 12, n. 12, p. 744–749, 1975. 7, 8

BORGNAKKE, C.; LARSEN, P. Statistical collision model for Monte Carlo simulation of polyatomic gas mixture. **Journal of Computational Physics**, v. 18, p. 405–420, 1975. 32, 33, 34, 43

BOYD, I. D. Analysis of rotational nonequilibrium in standing shock waves of nitrogen. **AIAA Journal**, v. 28, n. 11, p. 1997–1999, 1990. 33

\_\_\_\_\_. Monte carlo study of vibrational relaxation process. In: INTERNATIONAL SYMPOSIUM ON RAREFIED GAS DYNAMICS, 17th. **Proceedings...** Aachen, Germany, 1990. p. 792–799. 33

\_\_\_\_\_. Rotational and vibrational nonequilibrium effects in rarefied hypersonic flow. **Journal of Thermophysics and Heat Transfer**, v. 4, n. 4, p. 478–484, 1990. 33, 34, 43

\_\_\_\_\_. Rotational-translational energy transfer in rarefied nonequilibrium flows. **Physics of Fluids**, v. 2, n. 3, p. 447–452, 1998. 33

BOYD, I. D.; CHEN, G.; CANDLER, G. V. Prediction failure of the continuum fluid equations in the transition hypersonic flows. **Physics of Fluids**, v. 7, n. 1, p. 210–219, 1995. 16

BREWER, R. A.; SAYDAH, A. R.; NESTLER, D. E.; FLORENCE, D. E. Thermal performance evaluation of rsi panel gaps for space shuttle orbiter. **Journal of Spacecraft**, v. 10, n. 1, p. 23–28, 1973. 7, 8

BURNETT, D. The distribution of molecular velocities and the mean motion in a non-uniform gas. **Proceedings of the London Mathematical Society**, v. 40, n. 2, p. 382–435, 1936. 17

- CERCIGNANI, C. The Boltzmann equation and its applications. **Springer-Verlag**, 1988. 17
- CERCIGNANI, C.; LAMPIS, M. Kinetic models for gas-surface interactions. **Transport Theory and Statistical Physics**, v. 1, n. 2, p. 101–114, 1971. 37
- CHAPMAN, S.; COWLING, T. G. **The Mathematical Theory of Non-Uniform Gases**. [S.l.: s.n.], 1970. 16, 35
- CHARBONNIER, J.; BOERRIGTER, H. Contribution to the study of gap induced boundary layer transition in hypersonic flow. In: AIAA INTERNATIONAL AEROSPACE PLANES AND HYPERSONICS TECHNOLOGIES CONFERENCE, 5th. **Proceedings...** Munich, Germany: AIAA, 1993. p. 5111. 7, 8
- CHENG, H. K.; EMMANUEL, G. Perspective on hypersonic nonequilibrium flows. **AIAA Journal**, v. 33, n. 3, p. 385–400, 1995. 17
- COMEAX, K. A.; MACCORMACK, R. W.; CHAPMAN, D. R. An analysis of the burnett equations based on the second law of thermodynamics. In: AIAA AEROSPACE SCIENCE MEETING AND EXHIBIT, 33rd. **Proceedings...** Reno, NV., USA: AIAA, 1995. p. 0415. 17
- CORRÊA JR., F. A.; MORAES JR., P. Experimentos científicos e tecnológicos em ambiente de baixa gravidade. In: **Proceedings...** Águas de Lindóia, São Paulo, Brasil: COBEM, 1999. 1
- COX, R. N.; CRABTREE, P. L. **Elements of Hypersonic Aerodynamics**. [S.l.: s.n.], 1965. 15
- CYBYK, B. Z.; ORAN, E. S.; BORIS, J. P.; ANDERSON JR., J. D. Combining the monotonic lagrangian grid with Direct Simulation Monte Carlo model. **Journal of Computational Physics**, v. 122, p. 323–334, 1995. 21
- DIETRICH, S. Efficient computation of particle movement in 3-d DSMC calculations on structured body-fitted grids. **Rarefied Gas Dynamics**, p. 745–752, 1990. 17th International Symposium on Rarefied Gas Dynamics. 21
- DOMINIK, M.; JÜRIG, H. Ab initio molecular dynamics: Basic theory and advanced methods. 2009. Cambridge University Press. 18

DUNAVANT, J. C.; THROCKMORTON, D. A. Aerodynamic heat transfer to rsi tile surfaces and gap intersections. **Journal of Spacecraft and Rockets**, v. 11, p. 437–440, 1974. 7, 8

ENGBLOM, W. A.; GOLDSTEIN, D. B. Nose-tip surface heat reduction mechanism. **Journal of Thermophysics and Heat Transfer**, v. 10, n. 4, p. 598–605, 1996. 39

EVERHART, J. L.; ALTER, S. J.; MERSKI, N. R.; WOOD, W. A. Pressure gradient effects on hypersonic flow heating. In: AIAA AEROSPACE SCIENCES MEETING AND EXHIBIT, 44th. **Proceedings...** Orlando, FL., USA: AIAA, 2006. p. 0185. 7, 9, 39

FALLAVOLLITA, M. A.; BAGANOFF, D.; MCDONALD, J. D. Reduction of simulation cost and error for particle simulations of rarefied flows. **Journal of Computational Physics**, v. 109, p. 30–36, 1993. 48

FAY, J. A.; RIDDELL, F. R. Theory of stagnation point heat transfer in dissociated air. **Journal of Aeronautical Sciences**, v. 25, n. 2, p. 73–85, 1958. 99

FISCKO, K. A.; CHAPMAN, D. R. Hypersonic shock structure with burnett terms in the viscous stress and heat transfer. In: AIAA THERMOPHYSICS, PLASMADYNAMICS AND LASERS CONFERENCE, 23rd. **Proceedings...** San Antonio, CA., USA: AIAA, 1988. p. 2733. 17

\_\_\_\_\_. Comparison of burnett, super-burnett and monte carlo solutions for hypersonic shock structure, rarefied gas dynamics: Theoretical and computational techniques. **AIAA Progress in Astronautics and Aeronautics**, v. 118, p. 374–395, 1989. AIAA Paper 88-2733. 17

FRENKEL, D.; SMIT, B. Understanding molecular simulation from algorithms to applications. v. 1, 2009. Computational Science Series. 18

GAI, S.; MILTHORPE, J. F. Hypersonic high-enthalpy flow over a blunt-stepped cone. In: INTERNATIONAL SYMPOSIUM ON SHOCK WAVES, 20th. **Proceedings...** California, EUA: Edited by Sturtevant, B. and Shepherd, J.E and Hornung, H.G, v.1, 1995. p. 234–244. 7, 39

GALLIS, M. A.; TORCZYNSKI, J. R.; PLIMPTON, S. J.; RADERA, D. J. Direct simulation monte carlo the quest for speed. In: INTERNATIONAL SYMPOSIUM

ON RAREFIED GAS DYNAMICS, 29th. **Proceedings...** [S.l.]: AIAA, 2014. p. 27–36. 19

GRIFFITH, B. J.; LEWIS, C. H. Laminar heat transfer to spherically blunted cones at hypersonic conditions. **AIAA Journal**, v. 2, n. 3, p. 438–444, 1964. 122

GROTOWSKY, I. M. G.; BALLMANN, J. Numerical investigation of hypersonic step-flows. **Shock Waves**, v. 10, p. 57–72, 2000. 39

GUO, K.; LIAW, G. S. A review - boundary conditions for the dsmc method. In: AIAA THERMOPHYSICS CONFERENCE, 35th. **Proceedings...** Anaheim, CA., USA: AIAA, 2001. p. 175–191. 52

GUPTA, R. N.; SCOTT, C. D.; MOSS, J. N. Surface-slip equations for low Reynolds number multicomponent air flow. **Rarefied Gas Dynamics: Thermal Design of Aeroassisted Orbital Transfer Vehicles, Progress in Astronautics and Aeronautics**, v. 96, n. 465-490, 1985. 82

HAHN, M. Experimental investigation of separated flow over a cavity at hypersonic speed. **AIAA Journal**, v. 7, n. 6, p. 1092–1098, 1969. 2

HARVEY, J.; GALLIS, M. Review of code validation studies in high-speed low-density flows. **Journal of Spacecraft and Rockets**, v. 37, n. 1, p. 8–20, 2000. 19

HASH, D.; HASSAN, H. A. A generalized hard-sphere model for Monte Carlo simulation. **Physcis of Fluids**, v. 5, n. 3, p. 738–744, 1993. 25, 33

HASH, D. B.; HASSAN, H. A. Direct Simulation with vibration-dissociation coupling. **Journal of Thermophysics and Heat Transfer**, v. 7, n. 4, p. 680–686, 1993. 25

HASH, D. B.; MOSS, J. N.; HASSAN, H. A. Direct Simulation of diatomic gases using the generalized hard sphere model. **Journal of Thermophysics and Heat Transfer**, v. 8, n. 4, p. 758–764, 1994. 25

HAVILAND, J. K. The solution of two molecular flow problems by the monte carlo method. **Methods in Computational Physics**, v. 4, p. 109–209, 1965. 18

HAVILAND, J. K.; LAVIN, M. L. Application of monte carlo method to heat transfer in rarefied gases. **Physics of Fluids**, v. 5, p. 1399–1405, 1962. 18

HIGDON, J. J. L. Stokes flow in arbitrary two-dimensional domains: Shear flow over ridges and cavities. **Journal of Fluid Mechanics**, v. 159, p. 195–226, 1985. 7, 8

HINDERKS, M.; RADESPIEL, R.; GULHAN, A. Simulation of hypersonic gap flow with consideration of fluid structure interaction. In: AIAA FLUID DYNAMICS CONFERENCE AND EXHIBIT, 34th. **Proceedings...** Portland, Oregon: AIAA, 2004. p. 2238. 7, 8, 9

HINDERSKS, M.; RADESPIEL, R. Investigation of hypersonic gap flow of a reentry nose cap with consideration of fluid structure interaction. **AIAA Paper**, v. 6, p. 1111, 2006. 7, 8, 39

JACKSON, A. P.; HILLIER, R.; SOLTANI, S. Experimental and computational study of laminar cavity flows at hypersonic speeds. **Journal of Fluid Mechanics**, v. 427, p. 329–358, 2001. 39

JENKIS, D. R. **Space Shuttle: The History of the National Space Transportation System**. [S.l.]: Voyageur Press, 2007. 524 p. 2

KANNENBERG, K. C.; BOYD, I. Strategies for efficient particle resolution in the Direct Simulation Monte Carlo method. **Journal of Computational Physics**, v. 157, p. 727–745, 2000. 48

KEON-YOUNG, Y.; AGARWAL, R. K.; BALAKRISHNAN, R. Beyond navier-stokes: Burnett equations for flows in the continuum-transition regime. **Physics of Fluids**, v. 13, n. 10, p. 3061–3086, 2001. 17

KOURA, K. Null-collision technique in the Direct Simulation Monte Carlo method. **Physics of Fluids**, v. 29, n. 11, p. 3509–3511, 1986. 22, 25

KOURA, K.; MATSUMOTO, H. Variable soft sphere molecular model for inverse-power-law of lennard-jones potential. **Physics of Fluids**, A3, n. 10, p. 2459–2465, 1991. 25

\_\_\_\_\_. Variable soft sphere molecular model for air species. **Physics of Fluids**, A4, n. 5, p. 1083–1085, 1992. 25

KUNC, J. A.; HASSAN, H. A.; HASH, D. B. The GHS interaction model for strong attractive potentials. **Physics of Fluids**, v. 7, n. 3, p. 1173–1175, 1995. 25

LAUX, M. Optimization and parallelization of the DSMC method on unstructured grids. **American Institute of Aeronautics and Astronautics**, 1997. AIAA paper 97-2512. 21

LEE, C. J. Unique determination of solutions to the burnett equations. **AIAA Journal**, v. 32, n. 4, p. 985–990, 1994. 17

LEES, L. Laminar heat transfer over blunt-nosed bodies at hypersonic flight speeds. **Jet Propulsion**, v. 26, n. 4, p. 259–269, 1956. 99

LEITE, P. H. M. Simulação direta molecular da influência de degraus na superfície de veículos na reentrada. **INPE: Dissertation**, 2009. ix, 37

LORD, R. Application of the cercignani-lampis scattering kernel to direct simulation monte carlo method. In: INTERNATIONAL SYMPOSIUM ON RAREFIED GAS DYNAMICS, 17th. **Proceedings...** Aachen, Germany, 1991. p. 1427–1433. 37

\_\_\_\_\_. Direct Simulation of rarefied hypersonic flow over a flat-plate with incomplete surface accommodation. **Rarefied Gas Dynamics**, v. 160, p. 221–228, 1994. 37

LUMPKIN III, F. E.; CHAPMAN, D. R. Accuracy of the burnett equations for hypersonic real gas flows. **Journal of Thermophysics and Heat Transfer**, v. 6, n. 3, p. 419–425, 1992. 17

MACHELL, M. R. An experimental investigation of the flow over blunt-nosed cones at a mach number of 5.8. **Aeronautical Engineer Thesis**, 1956. CalTech-CA. 122

MOHRI, K.; HILLIER, R. **Computational and Experimental Study of Supersonic Flow Over Axisymmetric Cavities**. [S.l.]: SPRINGER, 2011. 39

MORGENSTERN JR., A.; CHOKANI, N. Hypersonic flow past open cavities. **AIAA Journal**, v. 32, n. 12, p. 2387–2393, 1994. 2

MOSS, J. N.; PRICE, J. M.; DOGRA, V. K.; HASH, D. B. Comparison of DSMC and experimental results for hypersonic external flows. **30th Thermophysics Conference**, 1995. American Institute of Aeronautics and Astronautics. 19

MOSS, J. N.; SCOTT, C. D. Thermophysical aspect of re-entry flows. **Progress in Astronautics and Aeronautics**, 1986. American Institute of Aeronautics and Astronautics. 19

NANBU, K. Rarefied gas dynamics: Theoretical basis of the direct simulation Monte Carlo method. **Journal of Computational Physics**, v. 1, p. 369–383, 1986. Eds. V. Boffi and C. Cercignani. 22, 25

NANCE, R. P.; WILMOTH, R. G.; HASSAN, H. A. Comparison of grid-definition schemes for Monte Carlo simulations. **Journal of Thermophysics and Heat Transfer**, v. 11, n. 2, p. 296–303, 1997. 21, 47

NESTLER, D. E. An experimental study of hypersonic cavity flow. **AIAA Journal**, v. 19, n. 3, p. 195–196, 1982. 2

NESTLER, D. E.; SAYDAH, A. R.; AUXER, W. L. Heat transfer to steps and cavities in hypersonic turbulent flow. **AIAA Journal**, v. 7, n. 7, p. 1368–1370, 1969. 2

OLYNICK, D. P.; MOSS, J. N.; HASSAN, H. A. Grid generation and adaptation for the Direct Simulation Monte Carlo method. **Journal of Thermophysics and Heat Transfer**, v. 3, n. 4, p. 368–373, 1989. 47

PALMER, G. E.; PULSONETTI, M.; WOOD, W. A.; ALTER, S.; GNOFFO, P.; TANG, C. Computational assessment of thermal protection system damage experienced during sts-118. **Journal of Spacecraft and Rockets**, v. 46, n. 6, p. 1110–1116, 2009. 4

PATIL, D. V.; LAKSHMISHA, K. N.; ROGG, B. Lattice boltzmann simulation of lid-driven flow in deep cavities. **Computers and Fluids**, v. 35, p. 1116–1125, 2006. 7, 8, 10

PETLEY, D. H.; SMITH, D. M.; EDWARDS, C. L. W.; CARLSON, A. B.; HAMILTON II, H. H. Surface step induced gap heating in the shuttle thermal protection system. **Journal of Spacecraft and Rockets**, v. 11, n. 2, p. 156–161, 1984. 7, 8

PITTS, W. C.; MURBACH, M. S. Flight measurements of tile gap heating on the space shuttle. **Fluids Plasma and Heat Transfer Conference**, 1982. AIAA Paper 82-0840. 7, 8

PRASANTH, P.; KAKKASSERY, J. K. Direct Simulation Monte Carlo (DSMC): A numerical method for transition-regime flows - a review. **Journal of Indian Institute of Science**, v. 86, p. 169–192, 2006. 19, 23

- \_\_\_\_\_. Molecular models for simulation of rarefield gas flows using Direct Simulation Monte Carlo method. **Fluid Dynamics Research**, v. 40, n. 4, p. 233–252, 2008. 32
- PROBSTEIN, R. F. Shock wave and flow field development in hypersonic re-entry. **Journal of American Rocket Society**, v. 31, p. 185–194, 1961. 15
- PULLIN, D. I.; DAVIS, J.; HARVEY, J. K. Monte Carlo calculations of the rarefied transition flow past a bluff faced cylinder. **AIAA - Progress in Astronautics and Aeronautics**, p. 379–391, 1977. 50, 52, 58, 59
- RAULT, D. F. G. Aerodynamic of the shuttle orbiter at high altitude. **Journal of Spacecraft and Rockets**, v. 31, n. 6, p. 944–952, 1994. 47
- REGAN, F. J.; ANANDAKRISHNAN, S. M. **Dynamics of Atmospheric Re-Entry**. USA: AIAA Education Series, 1992. 588 p. 6, 15
- RIEFFEL, M. A. A method for estimating the computational requirements of DSMC simulations. **Journal of Computational Physics**, v. 149, p. 95–113, 1999. 49
- ROMIG, M. Stagnation point heat transfer for hypersonic flow. **Jet Propulsion**, v. 26, n. 12, p. 1098–1101, 1956. 99
- SANTOS, W. F. N. Computational analysis of the aerodynamic heating and drag of a reentry brazilian satellite. In: NATIONAL CONGRESS OF MECHANICAL ENGINEERING, 4th. **Proceedings...** Campina Grande, PB, Brazil: AIAA, 2010. 89, 97, 105, 113
- \_\_\_\_\_. Aerothermodynamic analysis of a reentry brazilian satellite. **Brazilian Journal of Physics**, v. 42, n. 373-390, 2012. 41, 61
- SCHLINGLOFF, H. **Astronautical Engineering: An Introduction to the Technology of Spaceflight**. Germany: Ingenieurbuero Dr. Schlingloff, 2005. 505 p. 5
- SCOTT, C. D.; MARAIA, R. J. Gap heating with pressure gradients. In: AIAA THERMOPHYSICS CONFERENCE, 14th. **Proceedings...** Orlando, FL., USA: AIAA, 1979. 2, 7, 8, 39
- SHU, C.; MAO, X. H.; CHEW, Y. T. Particle number per cell and scaling factor effect on accuracy of DSMC simulation of micro flows. **International Journal of**

**Numerical Methods for Heat and Fluid Flow**, v. 15, n. 8, p. 827–841, 2005. 19, 21

SIBULKIN, M. Heat transfer near the forward stagnation point of a body of revolution. **Journal of Aeronautical Sciences**, v. 19, n. 8, p. 570–571, 1952. 98

SMITH, D. M.; PETLEY, D. N.; EDWARDS, C. L. W.; PATTEN, A. B. An investigation of gap heating due to stepped tiles in zero pressure gradient regions of the shuttle orbiter thermal protection system. In: AIAA AEROSPACE SCIENCES MEETING AND EXHIBIT, 21st. **Proceedings...** Reno, NV., USA: AIAA, 1983. p. 0120. 7, 8

TANNEHILL, J. C.; EISLER, G. R. Numerical computation of the hypersonic leading edge problem using the burnett equations. **Physics of Fluids**, v. 19, n. 1, p. 09–15, 1976. 17

THROCKMORTON, D. A. Effect of a surface-to-gap temperature discontinuity on the heat transfer to reusable surface insulation tile gaps. **NASA TECHNICAL NOTE**, 1976. NASA TN D-8233. 7, 8

TRAINEAU, J. C.; THIVET, F.; GULHAN, A.; COSSON, E.; SMITH, A.; MARRAFFA, L. Synthesis of the gap heating analysis of the hyflex flight. In: EUROPEAN SYMPOSIUM ON AEROTHERMODYNAMICS FOR SPACE VEHICLES, 5th. **Proceedings...** Cologne, Germany, 1983. 7, 8, 9

VENKATRAMAN, A.; ALEXEENKO, A. A. Molecular models for DSMC simulations of metal vapor deposition. **Rarified Gas Dynamics 2010**, 2010. 22

WEINSTEIN, I.; AVERY, D. E.; CHAPMAN, A. J. Aerodynamic heating to the gaps and surfaces of simulated reusable-surface-insulation tile arrays in turbulent flow at mach 6.6. **NASA TECHNICAL MEMORANDUM**, 1975. NASA TM X-3225. 7, 8

WIETING, A. R. **Experimental Investigation of Heat-Transfer Distributions in Deep Cavities in Hypersonic Separated Flow**. WASHINGTON - USA: NASA TECHNICAL NOTE, 1970. 8, 39

WILKINSON, D. B.; HARRINGTON, S. A. Hypersonic force, pressure and heat transfer investigations of sharp and blunt slender cones. **Rept. AF-1560-A-5**, 1962. Cornell Aeronaut. Lab. 122

WILMOTH, R. G.; LEBEAU, G. J.; CARLSON, A. B. DSMC grid methodologies for computing low-density, hypersonic flows about reusable launch vehicles.

**NASA Langley Technical Report Server**, 1996. 21, 47

XU, J.; HUANG, H.; HUANG, G.; MO, S. **Numerical Simulation of Supersonic Gap Flow**. [S.l.]: PLOS ONE, 2015. 7, 8, 11

YEN, S. M. Monte carlo solutions of nonlinear boltzmann equation for problems of heat transfer in rarefied gases. **International Journal of Heat and Mass Transfer**, v. 14, p. 1865–1865, 1971. 18

\_\_\_\_\_. Numerical solution of the nonlinear Boltzmann equation for nonequilibrium gas flow problems. **Annual Review of Fluid Mechanics**, v. 16, p. 67–97, 1984. 18

YOSHIO, S. Molecular gas dynamics: Theory, technique, and applications. **Birkhäuser**, v. 1, 2007. Modeling and Simulation in Science, Engineering and Technology. 18

ZHONG, X.; MCCORMACK, R. W.; CHAPMAN, D. R. Stabilization of the burnett equations and application to hypersonic flows. **AIAA Journal**, v. 31, n. 6, p. 1036–1043, 1993. 17

## PUBLICAÇÕES TÉCNICO-CIENTÍFICAS EDITADAS PELO INPE

### **Teses e Dissertações (TDI)**

Teses e Dissertações apresentadas nos Cursos de Pós-Graduação do INPE.

### **Manuais Técnicos (MAN)**

São publicações de caráter técnico que incluem normas, procedimentos, instruções e orientações.

### **Notas Técnico-Científicas (NTC)**

Incluem resultados preliminares de pesquisa, descrição de equipamentos, descrição e ou documentação de programas de computador, descrição de sistemas e experimentos, apresentação de testes, dados, atlas, e documentação de projetos de engenharia.

### **Relatórios de Pesquisa (RPQ)**

Reportam resultados ou progressos de pesquisas tanto de natureza técnica quanto científica, cujo nível seja compatível com o de uma publicação em periódico nacional ou internacional.

### **Propostas e Relatórios de Projetos (PRP)**

São propostas de projetos técnico-científicos e relatórios de acompanhamento de projetos, atividades e convênios.

### **Publicações Didáticas (PUD)**

Incluem apostilas, notas de aula e manuais didáticos.

### **Publicações Seriadas**

São os seriados técnico-científicos: boletins, periódicos, anuários e anais de eventos (simpósios e congressos). Constam destas publicações o International Standard Serial Number (ISSN), que é um código único e definitivo para identificação de títulos de seriados.

### **Programas de Computador (PDC)**

São a seqüência de instruções ou códigos, expressos em uma linguagem de programação compilada ou interpretada, a ser executada por um computador para alcançar um determinado objetivo. Aceitam-se tanto programas fonte quanto os executáveis.

### **Pré-publicações (PRE)**

Todos os artigos publicados em periódicos, anais e como capítulos de livros.